Foundations and Trends® in
Robotics
Vol. 2, No. 3 (2011) 143–259

DOI: 10.1561/2300000023

now
the essence of knowledge

Micro-Scale Mobile Robotics

By Eric Diller and Metin Sitti

Contents

Foundations and Trends® in
Robotics
Vol. 2, No. 3 (2011) 143–259

DOI: 10.1561/2300000023

now
the essence of knowledge

Micro-Scale Mobile Robotics

Eric Diller[1] and Metin Sitti[2]

[1] *Carnegie Mellon University, NanoRobotics Lab, Department of Mechanical Engineering, Pittsburgh, PA 15213, USA, ediller@cmu.edu*
[2] *Carnegie Mellon University, NanoRobotics Lab, Department of Mechanical Engineering, Pittsburgh, PA 15213, USA, sitti@cmu.edu*

Abstract

The field of microrobotics has seen tremendous advances in recent years. The principles governing the design of such submillimeter scale robots rely on an understanding of microscale physics, fabrication, and novel control strategies. This monograph provides a tutorial on the relevant physical phenomena governing the operation and design of microrobots, as well as a survey of existing approaches to microrobot design and control. It also provides a detailed practical overview of actuation and control methods that are commonly used to remotely power these designs, as well as a discussion of possible future research directions. Potential high-impact applications of untethered microrobots such as minimally invasive diagnosis and treatment inside the human body, biological studies or bioengineering, microfluidics, desktop micromanufacturing, and mobile sensor networks for environmental and health monitoring are reported.

1

Introduction

Due to recent advances in micro- and nanoscale science and technology and increasing demand for new microsystems for applications in medicine, biotechnology, manufacturing, and mobile sensor networks, creating tiny mobile robots that could access enclosed small spaces down to the micron scale such as inside the human body and microfluidic devices and could manipulate and interact with micro/nanoscale entities has become a critical issue. Since human or macroscale robot sensing, precision, and size are not sufficient to interact with such tiny objects and access such tiny spaces directly, microrobotics has emerged as a new robotics field to extend our interaction and exploration capabilities to submillimeter scales. Moreover, mobile microrobots could be manufactured cost-effectively in large numbers where a large number of microrobots could enable new massively parallel, self-organizing, reconfigurable, swarm, or distributed systems. For these purposes, many groups have been proposing various untethered mobile microrobotic systems in the past decade. Such untethered microrobots could enable many new applications such as minimally invasive diagnosis and treatment inside the human body, biological studies or bioengineering applications inside microfluidic channels, desktop micromanufacturing, and mobile sensor networks for environmental and health monitoring.

There is no standardized definition of the term *microrobot*. In fact, reported microrobots range in size from single μms to the cm scale. However, one common approach defines a microrobot as existing in the size range of hundreds of nm to 1 mm. In some cases, *component size scale* being micron scale is taken as the crucial aspect, which could then include millimeter or centimeter-scale mobile robots as microrobots. In other cases, *overall size scale* being micron scale is emphasized where mobile robots able to fit in spaces smaller than a millimeter are considered as microrobots. In this monograph, the latter is used to define microrobots since the overall size dictates the environment in which the robots are capable of accessing, and also tells us something about their capabilities. On the other hand, a more relevant definition when studying novel wireless locomotion schemes might involve the types of *physical interactions* which dominate the motion and interaction of the robot. Large or centi/milli-scale robots are dominated by inertial and other bulk forces, while the motion of microrobots is dominated by surface area-related forces, including friction, adhesion, drag, and viscous forces at the micro-scale. The lower-bound of microrobots could likewise be when assumptions of the continuity of matter are no longer valid. At sizes below tens of μm, effects such as Brownian motion and chemical interactions could lead to stochastic descriptions of motion behavior. This is the realm of *nanorobots*, and will not be addressed in this survey. Thus, we define microrobots as being roughly in the size range single to hundreds of μm, and being dominated by micro-scale physical forces and effects.

This size range presents significant new challenges in fabrication, actuation, and power supply not seen in larger traditional robotics. This size scale is particularly interesting because new physical principles begin to dominate the behavior. As we go smaller, the balance of different forces changes dramatically, and we see increases in friction and adhesion while the influence of weight and inertia is markedly reduced. Other changes in fluid mechanics, stochastic motions, and shorter time scales also challenge natural engineering notions as to how robotic elements move and interact. These physical effects must be taken into account when designing and operating robots at the small scale.

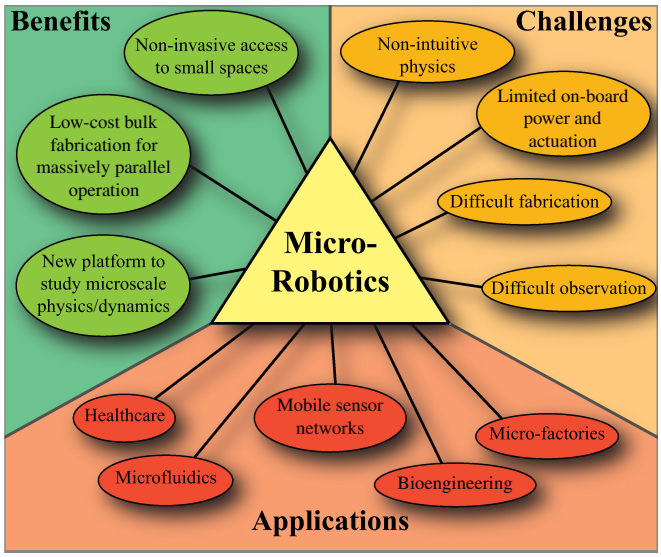

Fig. 1.1 Diagram showing the benefits, challenges, and potential applications of micro-scale mobile robots.

The benefits, challenges, and potential applications of micro-scale mobile robots are overviewed in Figure 1.1. Here we see that micro-robots promise to access small spaces in a non-invasive manner as a new platform for microscale physics/dynamics. Compared with other robotic systems, they can be fabricated inexpensively in bulk for potential massively parallel applications. However, several challenges arise in the design and control of micro-scale robots such as nonintuitive physical forces, limited options for power and actuation, significant fabrication constraints, and difficulty in localizing such tiny robots. The field of microrobotics is particularly exciting due to the potential applications in healthcare, bioengineering, microfluidics, mobile sensor networks, and in micro-factories.

1.1 Brief History of Microrobotics

Advances in and increased use of microelectromechanical systems (MEMS) since the 1990s have driven the development of untethered microrobots. MEMS fabrication methods allow for precise features to

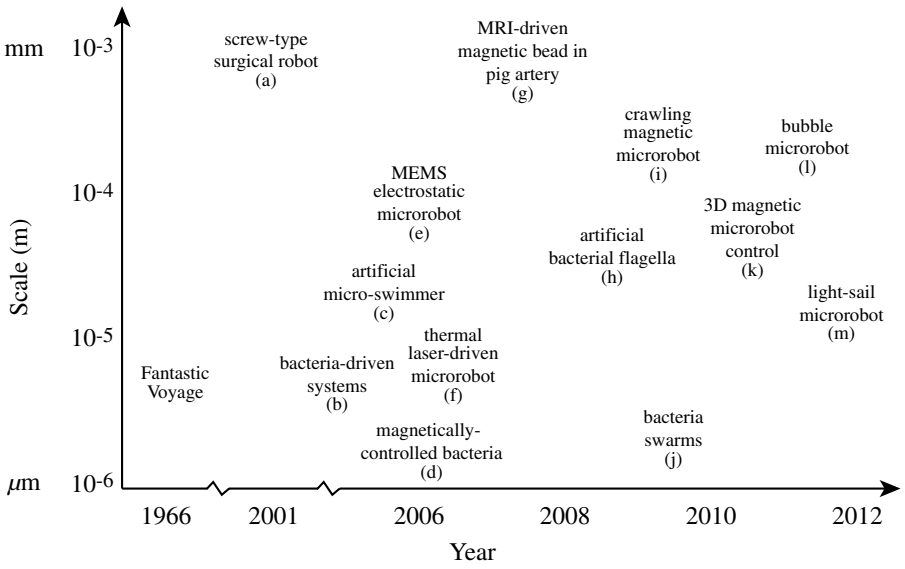

Fig. 1.2 Approximate timeline showing the emerging new microrobot systems as significant milestones. (a) Screw-type surgical robot [100]. (b) Bacteria-driven systems [40]. (c) Artificial micro-swimmer [53]. (d) Magnetically controlled bacteria [133]. (e) MEMS electrostatic microrobot [50]. (f) Thermal laser-driven microrobot [201]. (g) MRI-driven magnetic bead in pig artery [132]. (h) Artificial bacterial flagella [236]. (i) Crawling magnetic microrobot [155]. (j) Bacteria swarms [134]. (k) 3D magnetic microrobot control [115]. (l) Bubble microrobot [96]. (m) Light-sail microrobot [27].

be made from a wide range of materials which can be useful for functionalized microrobots. There has been a surge in microrobotics work in the past few years, and the field is relatively new and is growing fast [186]. Figure 1.2 overviews a few of the new microrobotic technologies which have been published, along with their approximate size scale.

In popular culture, the field of microrobotics is familiar to many due to the 1966 sci-fi movie *Fantastic Voyage*, and later the 1987 movie *Innerspace*. In these films, miniaturized submarine crews are injected inside the human body and perform noninvasive surgery. The first studies in untethered robots using principles which would develop into microrobot actuation principles were only made recently, such as a magnetically driven screw which moved through tissue [100]. Other significant milestone studies in untethered microrobotics include a study on bacteria-inspired swimming propulsion [55], bacteria-propelled

beads [14, 40], steerable electrostatic crawling microrobots [50], laser-powered micro-walkers [201], magnetic resonance imaging (MRI) device-driven magnetic beads [132], and magnetically driven mm-scale nickel robots [231]. These first studies have been followed by other novel actuation methods such as helical propulsion [75, 236], stick-slip crawling microrobots [155], magnetotactic bacteria swarms as microrobots [135], optically driven "bubble" microrobots [96], and microrobots driven directly by the transfer of momentum from a directed laser spot [27], among others. Figures 1.3 and 1.4 show a number of the existing approaches to microrobot mobility in the literature for motion in 2D/3D. These methods will be discussed in detail in Section 3. It is immediately clear that actual microrobots do not resemble the devices shrunk down in popular microrobotics depictions.

As an additional driving force for the development of mobile microrobots, the Mobile Microrobotics Competition sponsored and run by the National Institute of Standards and Technology (NIST) began in

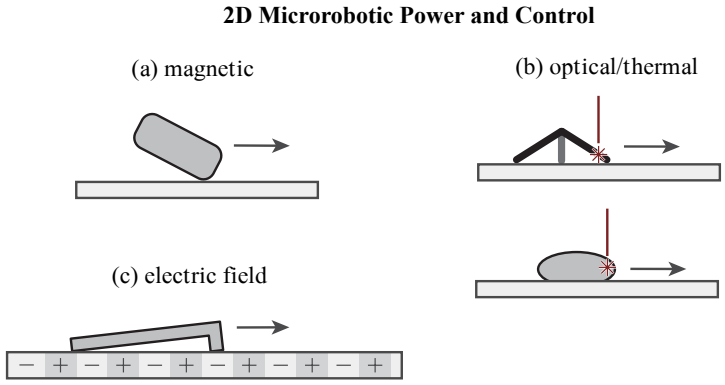

Fig. 1.3 Some existing approaches to mobile microrobot power and control in 2D. (a) Magnetically-driven crawling robots include the Mag-μBot [155], the Mag-Mite magnetic crawling microrobot [71], the magnetic microtransporter [173], rolling magnetic microrobot [105], the diamagnetically-levitating mm-scale robot [157], the self-assembled surface swimmer [192], and the magnetic thin-film microrobot [106]. (b) Thermally-driven microrobots include the laser-activated crawling microrobot [201], micro light sailboat [27], and the optically controlled bubble microrobot [96]. (c) Electrically-driven microrobots include the electrostatic scratch-drive microrobot [52] and the electrostatic microbiorobot [174]. Other microrobots which operate in 2D include the piezoelectric-magnetic microrobot MagPieR [28] and the electrowetting droplet microrobot [176].

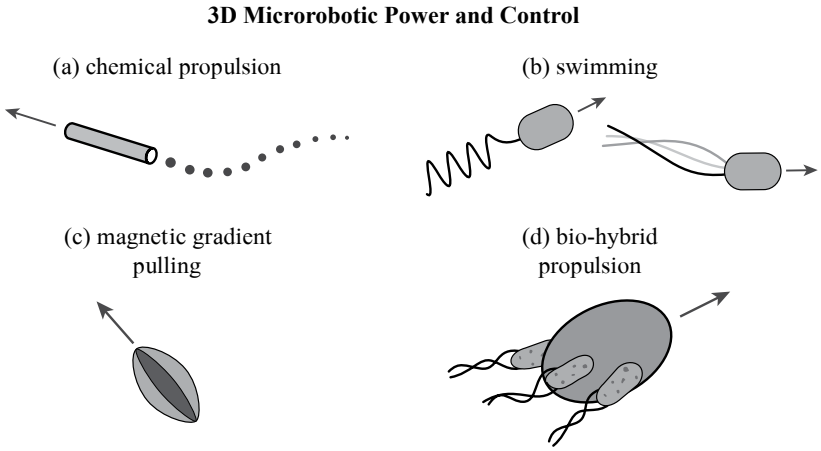

Fig. 1.4 Some existing approaches to mobile microrobot power and control in 3D. (a) Chemically-propelled designs include the microtubular jet microrobot [193] and the electro-osmotic swimmer [98]. (b) Swimming microrobots include the colloidal magnetic swimmer [53], the magnetic thin-film helical swimmer [226], the micron-scale magnetic helix fabricated by glancing angle deposition [75], the micro-helix microrobot with cargo carrying cage, fabricated by direct laser writing [208] and the micro-helix microrobot with magnetic head, fabricated as thin-film and rolled using residual stress [237]. (c) Microrobots pulled in 3D using magnetic field gradients include the nickel microrobot capable of 5 DOF motion in 3D using the OctoMag system [115] and the MRI-powered and imaged magnetic bead [131]. (d) Bio-hybrid approaches include the artificially-magnetotactic bacteria [99], the chemotactic steering of bacteria-propelled microbeads [110] and the bacteria swarm manipulating micron-scale bricks [134].

2007 as the "nanogram" league of the popular Robocup robot soccer competition [82]. This yearly event has moved to the International Conference on Robotics and Automation (ICRA), and challenges teams to accomplish mobility and manipulation tasks with an untethered microrobot smaller than 500 μm on a side. The competition has spurred several research groups to begin research in microrobotics, and has helped define the challenges most pressing to the microrobotics research field.

This monograph introduces the reader to micro-scale robotics in the context of the relevant micro-scale physical effects which govern their operation. It begins with an overview of the most commonly encountered physical effects in Section 2, followed by a review of some of

the microrobot actuation methods used in Section 3. The monograph concludes with a discussion of potential application areas in Section 4 and a summary of the current status of the field, along with a list of important open challenges in Section 5. A list of nomenclature used throughout the monograph is also given at the end.

2

Microscale Challenges

Here we introduce some of the challenges encountered when designing and operating micro-scale robots. To overview the technology available today, and those that may be practical in the future, we discuss the dominant physics and dynamics experienced by micro-scale robots and entities and discuss methods of microrobot localization, power delivery, and fabrication.

2.1 Microscale Physics and Dynamics

2.1.1 Scaling Effects

All entities, regardless of size, experience the same physical forces and are governed by the same laws. However, as the magnitude of such forces is usually size-dependent, the relative strength of physical effects can change dramatically with scale. Scaling down an object's size with a length scale factor of L isometrically, its surface area and volume would scale with L^2 and L^3, respectively. This means that the surface area-to-volume ratio would increase at very small length scales such as micro- or nano-scale dimensions, and surface area-related forces and dynamics would dominate at the micro/nano-scale.

Table 2.1. Scaling of different forces dependent on length (perimeter), surface area, and volume.

Length dependent ($\propto L$)	Surface tension
Area dependent ($\propto L^2$)	Surface forces, fluid drag, friction, Reynolds number (Re), evaporation, fluid drag transient time τ (low Re), heat conduction, electrostatic forces
Volume dependent ($\propto L^3$)	Mass, inertia, heat capacity, buoyancy

The dependence of a force on the characteristic scale L approximately determines its relative influence at different size scales. The length dependence of some common forces in microrobotics is listed in Table 2.1. One major factor for many force balance comparisons is the surface area-to-volume ratio S/V, which is proportional to L^{-1}. As an example from the natural world, a meter-scale whale may have an S/V ratio of about 1 m^{-1}, while a micron-scale bacteria may have an S/V ratio of about 10^7 m^{-1}.

The scaling laws lead to some interesting trends in the abilities and limitations of small animals in nature. Small insects often have capabilities which are not possible at the larger scale. For example, the water strider insect can use surface tension rather than buoyancy to support its weight on a water surface [94]. Other insects can jump very high in proportion to their size [203]. On the other hand, the life span of smaller animals is reduced because the time scale is quickened such that vibrations and heart rate are increased [179]. Smaller objects also lose heat at a faster rate, thus only larger animals support a warm-blooded system. Similar accommodations must be made with small mechanical systems to operate effectively.

2.1.1.1 Scaling of mechanical systems

If it is assumed that the bulk values of material strength, modulus, density, friction coefficient, etc. are invariant with size, we can analyze how the behavior of mechanical mechanisms scales. The bending stiffness of a beam varies roughly with thickness^4/length$^3 \propto L^1$. However, deformation is proportional to force/stiffness (L^1), so the shape of

a deformed structure is scale invariant. The resonant frequency of a vibrating system equals $\sqrt{\text{stiffness/mass}} \propto L^{-1}$, so increases as the size is reduced. An example resonant microscale robot which vibrates at a high frequency is the MagMite [71]. This two-mass system vibrates at several kHz frequency due to its small size of less than 200 μm.

In addition to the increase in resonant speeds, microorganism and microrobot locomotion speeds are typically normalized by body size. Thus, some small organisms can have relative speed much higher than large animals or robots. Bacteria swim with speeds of 20–40 body-lengths per second (blps), while a whale only swims at speeds of about 0.4 blps. In a similar way, microrobots can travel at speeds up to hundreds of blps, while large-scale robots typically travel up to several blps.

Electrostatic and magnetic forces are particularly relevant microrobotic actuation principles. In electrostatic attraction between charged plates, the force scales by the square of the area of the plates and the inverse square of the plate gap. A magnetic force between two permanent magnets scales as the square of the magnet volume and the inverse fourth power of the gap, while a magnetic torque between two permanent magnets scales as the square of the magnet volume and the inverse third power of the gap. However, isometric scaling may not be the best scaling method to compare these methods of actuation because for a given actuation scheme, the gap or element size may be held constant. For example, in the case of a magnetic microrobot driven by external magnets, workspace limitations may mean that the actuation magnet may not come closer to the microrobot as the size scale decreases. Indeed, the scaling of magnetic systems driven by magnetic coils is even more complex as issues of electrical current density must be taken into consideration [34]. Thus, it is difficult to fairly compare scaling laws between these different actuation methods. In general, however, it can be seen that electrostatic actuation forces scale down more favorably than magnetic ones, especially when operating at scales approaching 1 μm [4].

A summary of the scaling laws for other relevant mechanical phenomena is listed in Table 2.2, for an isometric scaling law except where

Table 2.2. Approximate scaling of different mechanical systems and properties.

Characteristic	Scales with	Scaling factor
Bending stiffness	$\text{Thickness}^4/\text{length}^3$	L^1
Beam resonant frequency	$\sqrt{\text{Stiffness}/\text{mass}}$	L^{-1}
Deformation	Force/stiffness	L^1
Mechanical power density	Power/volume	L^1
Friction force	Force	L^2
Impact force	Mass $\times$ acceleration	L^4
Electrostatic breakdown	Gap size	L^1
Electrostatic force	$\text{Area}^2/\text{gap}^2$	L^0
Magnetic force	$\text{Volume}^2/\text{gap}^4$	L^2
Magnetic torque	$\text{Volume}^2/\text{gap}^3$	L^3

indicated. For a more comprehensive scaling analysis of physical forces, the reader is referred to Wautelet et al. [217].

Microrobot motion is also strongly influenced by temperature, humidity, vibrations, and fluid flow which may not be critical factors for large-scale robots. Strong nonlinearities in surface forces make motion difficult to predict, and stochastic variations further complicate study. We now review some of the mechanics of motion at the small-scale.

2.1.2 Micron-Scale Mechanics

Here, we discuss the surface area and perimeter-related forces that dominate the motion of objects such as microrobots. Most notably, the motion of such objects becomes dominated by adhesive and friction forces rather than inertial forces, and operate in a unique fluid dynamics regime dominated by viscous forces. While some of the physical trends present challenges to design and control microrobots correctly, in some cases they open up new methods of locomotion and manipulation which are not feasible at larger scales. Developing an understanding of such forces is paramount in the design and operation of mobile microrobots.

2.1.2.1 Adhesion

Intermolecular forces act to hold objects close together when their spacing is small, where adhesion is defined as the pull-off force required to separate two surfaces in contact in a given environment, e.g., air, liquid,

or vacuum. In ambient condition, these forces can be due to van der Waals interactions, capillary effects, hydrogen bonding, covalent bonding, electrostatic charging, or Casimir forces [60]. Capillary forces can be very significant when there are air–fluid–solid boundaries. Electrostatic effects are often small compared to van der Waals forces [9].

To determine the adhesive force between materials 1 and 2, the work of adhesion, W_{12}, must be determined for the pair utilizing their intrinsic surface energies γ_1 and γ_2 as [73, 101]

$$W_{12} = \gamma_1 + \gamma_2 - \gamma_{12} \approx 2\sqrt{\gamma_1 \gamma_2}. \tag{2.1}$$

Adhesion modeling for micro- and nano-particle manipulation is discussed in [73, 139, 189], where the Johnson–Kendall–Roberts (JKR), Derjaguin–Muller–Toporov (DMT), and Dugdale (D) models are the three main contact mechanics models at the micro-nanoscale for any specific case. To determine which of the three models is most appropriate to use, a dimensionless parameter λ, often called the elasticity, or Tabor parameter, is introduced as

$$\lambda = \left(\frac{8 R_e W_{12}^2}{\pi h^3 K^2} \right)^{\frac{1}{3}}, \quad \text{where} \tag{2.2}$$

$$K = \frac{4}{3} \left(\frac{1 - \nu_1^2}{E_1} + \frac{1 - \nu_2^2}{E_2} \right)^{-1}, \quad \text{and} \tag{2.3}$$

$$R_e = (R_1^{-1} + R_2^{-1})^{-1}. \tag{2.4}$$

Here, R_e is the effective radius of contact of the two spherical objects of radii R_1 and R_2, $h = 0.165$ nm is a typical separation distance between the points of contact for the two materials' atoms, and K is the equivalent elastic modulus of contact, based upon each material's Young's modulus (E_1 and E_2) and Poisson's ratio (ν_1 and ν_2) [101]. Values of several of these properties for different materials commonly seen in microrobotics are given in Table 2.4. The elasticity parameter λ is then used to determine the appropriate model to use as is outlined in Table 2.3 as $\lambda < 0.6$ for DMT, $\lambda > 5$ for JKR, and the D model for intermediate values. An alternative intermediate adhesion model is the Pietrement model [151, 162], but the Dugdale model is given here as it is easier to apply. The adhesive (pull-off) force for the Dugdale model

Table 2.3. Micro/nano-scale Contact model details. The Dugdale model force P_{D} is given in Equation (2.5).

Model	Valid for	Pull-off force	Description
DMT	$\lambda < 0.6$	$P = -2\pi RW_{12}$	Long-range surface forces act outside contact area
JKR	$\lambda > 5$	$P = -\frac{3}{2}\pi RW_{12}$	Long-range surface forces act inside contact area
D	$0.6 < \lambda < 5$	$P = P_{\mathrm{D}}$	Interface modeled as a crack

Table 2.4. Properties of materials commonly encountered in microrobotics studies.

Material	Surface energy γ (mJ m^{-2})	Elastic modulus E (GPa)	Poisson ratio ν
Glass	83–280 [150, 167, 175, 36]	70	0.25
Polystyrene	33–40 [235, 73]	3.2	0.35
Silicon	46–72 [97]	160 [87]	0.17 [87]
Silicon dioxide	17.8 [97]	70 [112]	0.17
Gold	1080 [211]	79	0.42
Nickel	2450 [191]	200	0.31
SU-8	28–70 [215]	2.0	0.37
Polymers	∼15–45 [107]	∼0.3–3.4	∼0.3–0.4
Water	72.3	—	—
Silicone oil	19.8–21 [2, 86]	—	—

is given as [73, 139].

$$P_{\mathrm{D}} = -\left(\frac{7}{4} - \frac{1}{4}\frac{4.04\lambda^{1/4} - 1}{4.04\lambda^{1/4} + 1}\right)\pi RW_{12}. \tag{2.5}$$

Due to the wide range of possible surface energies for glass given in Table 2.4, there is a large range of pull-off forces that can potentially exist with this surface. This wide range can be reduced when operating immersed in liquid.

When immersed completely in a fluid, the capillary and electrostatic contributions to the pull-off force can be reduced due to the lack of air-fluid interfaces and dispersion of electrical charges. The van der Waals, double layer, steric, hydrophobic, and other intermolecular forces in liquid will thus dominate and now will include fluid interaction forces [101]:

$$W_{132} = W_{12} + W_{33} - W_{13} - W_{23}. \tag{2.6}$$

Positive or negative total work of adhesion values W_{132} can result from different material and liquid layer combinations. Negative values

imply the two surfaces repel each other, whereby the surfaces minimize their energy by contacting the fluid, not each other. As an example of this case, a glass surface is used with polystyrene beads for manipulation in [67]. The range of immersed work of adhesion from the values given in Table 2.4 when immersed in water is $-45\ \text{mJ}\cdot\text{m}^{-2} < W_{132} < -3.1\ \text{mJ}\cdot\text{m}^{-2}$. As this range is necessarily negative, the adhesion is negative between these two surfaces, implying repulsion. This repulsion can aid in object motion, as the motion will be governed primarily by fluid interactions. For irregularly shaped particles, the pull-off force will also be greatly reduced from its perfectly smooth value.

Van der Waals forces

Van der Waals forces are due to instantaneous fluctuating dipole moments which act on nearby atoms within a material to generate an induced dipole moment. Dispersion (London) forces act on all molecules, and are quantum mechanical in origin. Orientation (Keesom) forces result from attraction between permanent dipoles, such as the case with water, and are negligible for nonpolar molecules. Induction (Debye) forces are between permanent and induced dipoles.

Van der Waals forces always exist, and are considered long-range adhesive forces, acting at ranges of 0.2–20 nm. The forces between two identical materials are always attractive, but can be repulsive for certain cases involving different materials. Thus, the van der Waals force is an important consideration for micro-scale robotics involving objects in contact. For the case of an atomically smooth sphere–plane contact geometry, van der Waals forces can be modeled as

$$F_{vdW}(h) \approx -\frac{AR}{6h^2}, \tag{2.7}$$

where R is the sphere radius, h is the sphere–plane separation distance, and A is the Hamaker constant. The Hamaker constant is found as

$$A = \pi^2 C \rho_1 \rho_2, \tag{2.8}$$

where C is the coefficient in the particle–particle pair interaction, and ρ_1 and ρ_2 are the number of atoms in the two interacting bodies per

Table 2.5. Hamaker constant for several common materials, from [101] unless otherwise noted.

Material	Hamaker constant (zJ)
Air, vacuum	0
Water	37–40
Hydrocarbons	∼50
Ethanol	42
Acetone	50
Polystyrene	65–79
PTFE	38
Iron	212 [214]
Iron oxide	210
Metals	300–500
Quartz	42–413 [214]
Silicon	221–256 [214]
Silicon dioxide	85–500 [214]
Gold	400
Copper	284 [214]
PMMA	63 [214]
Polymers	52–88 [214]

unit volume. Hamaker constants do not vary widely between different materials, and mostly lie in the range of $(0.4\text{–}4)\times10^{-19}$ J. Values for some materials are given in Table 2.5. Force relations for other contact geometries and additional details of van der Waals interactions are given in [101]. The Hamaker constant for disparate materials with constants A_1 and A_2 in contact can be found as

$$A_{12} \approx \sqrt{A_1 A_2}. \tag{2.9}$$

For two solids with constants A_1 and A_1 separated by a liquid with constant A_3, the Hamaker constant can be found as

$$A_{132} \approx \left(\sqrt{A_{11}} - \sqrt{A_{33}}\right)\left(\sqrt{A_{22}} - \sqrt{A_{33}}\right). \tag{2.10}$$

The relation of van der Waals force for very small separations can be investigated approximately using the Lennard–Jones potential, which is a simple model that predicts the change from attraction to repulsion at very small interatom spacings due to Pauli repulsion. The relation for two atoms separated by distance r_s is of the form

$$w(r_s) = -A_L/r_s^6 + B_L/r_s^{12}, \tag{2.11}$$

where w is the interaction potential and $A_L = 10^{-77}$ J m^6 and $B_L = 10^{-134}$ J m^{12} [101]. The interaction force using this potential can be computed as

$$F(r_s) = -\frac{dw(r_s)}{dr_s}, \tag{2.12}$$

The van der Waals force is reduced by the surface roughness because the two rigid surfaces are locally further separated. Taking b_r as the root-mean square roughness of two surfaces separated by distance h, the force is attenuated as [188]

$$F_{vdW,\text{rough}}(h) \simeq \left(\frac{h}{h + b_r/2}\right)^2 F_{vdW}(h), \tag{2.13}$$

where h is measured to the top of the surface roughness. Typical roughness values are approximately 2 nm for a polished silicon wafer, and 1 μm for a polished metal surface.

Capillary forces

Capillary forces act at fluid–air–solid interfaces to minimize the surface energy of the interface. As an example of the potential of these forces, they are used by trees to transport water from the roots to the leaves through capillaries several microns in diameter [89]. Thus, these forces can be relatively large in certain circumstances. The height h_c of liquid in a tube due to the capillary force is found using the Jurin equation

$$h_c = \frac{2\gamma_l \cos\theta}{\rho g r_t}, \tag{2.14}$$

where γ_l is the liquid surface tension, θ is the liquid–solid contact angle, ρ is the fluid density, g is the acceleration due to gravity, and r_t is the radius of the tube. As an example for a water-filled glass tube of radius $r_t = 1$ μm, with $\gamma = 0.072$ N/m, $\theta = 20°$, $\rho = 1000$ kg/m^3, the meniscus height will be 15 m.

The adhesive properties of surfaces in an ambient air environment can be sensitive to vapor in the environment due to capillary condensation which forms in the cracks and pores of a surface [101]. The forces which occur when two objects contact in the presence of this thin liquid layer is dependent on the curvature of the spherical concave meniscus

which forms between. This curvature r_k can be found for the case of sphere–plane contact using the Kelvin equation [6]

$$r_k = \frac{\gamma_l V}{R_g T \log(p/p_s)}, \tag{2.15}$$

where V is the liquid molar volume, R_g is the gas constant, T is the temperature, and p/p_s is the relative humidity. For water at 20°C, $\gamma_l V/(R_g T) = 0.54$ nm, resulting in $r_k = 10$ nm at 90% humidity, $r_k = 1.6$ nm at 50% humidity and $r_k = 0.5$ nm at 10% humidity. The resulting force can be derived approximately from the Laplace equation [6, 101] as

$$F = \frac{4\pi R_s \gamma_l \cos\theta}{1 + (h/d_w)}. \tag{2.16}$$

Here, R_s is the sphere radius and θ is the liquid contact angle, h is the sphere–wall separation, and d_w is the immersion depth of the sphere. This force is at its maximum when the sphere is in contact with the surface and reduces as it is pulled away.

Thus, control of environmental humidity can have a large effect on the capillary force between two objects in an air environment, depending on their surface properties. Indeed, for hydrophobic surfaces ($\theta > 90°$), this capillary force can even be repulsive. Capillary forces can immobilize microrobots such as the electrostatically driven scratch drive microrobot in [50]. This microrobot operates in a dry nitrogen environment with less than 15% relative humidity to prevent such effects. As another example, water strider insects with sub-millimeter diameter superhydrophobic legs repel water dominated by such repulsive capillary forces while buoyancy of their thin legs is negligible. In this way they support their body weight with repulsive surface tension forces [195, 200].

Electrostatic forces

Electrostatic forces can develop between nonconductive objects resulting from charge buildup, electrical dipoles, or applied voltage [73]. Forces can also be induced between conductive surfaces when a voltage potential is applied to them. The force on a sphere of radius R_s at voltage potential U with a gap of distance h from a grounded plane is

given by [72]

$$F_e = 2\pi\epsilon\epsilon_0 R_s^2 U^2 \left[\frac{1}{2(h+R_s)^2} - \frac{8R_s(R_s+h)}{[4(h+R_s)^2 - R_s^2]^2}\right], \tag{2.17}$$

where ϵ is the relative dielectric constant of the medium and $\epsilon_0 = 8.85 \times 10^{-12}$ F/m is the dielectric constant of vacuum (vacuum permittivity). The relative permeability of air is approximately 1, while that of water is 80.4. Electrostatic forces can be significantly smaller in water than in air because charge is able to dissipate through water. These electrostatic forces can be complex in practice and are often time-variant and difficult to measure. Therefore, it is often best in a microrobotics application to reduce them. Electrostatic forces can be reduced by using conductive or grounded objects or by operating in conductive liquid environments. One common method when operating in an air or other nonconductive environment is to sputter a thin layer of conductive material onto the object surfaces and ground such a conductive layer to disperse the charges, and reduce the electrostatic forces.

A comparison of weight and adhesive forces is given in Figure 2.1. Here, typical values are chosen for a gold microsphere of radius R_s in

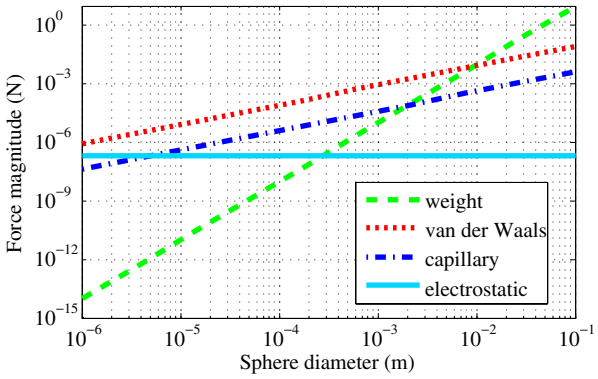

Fig. 2.1 Comparison of weight and adhesive forces for a gold sphere in close 0.2 nm contact with a gold surface. The surfaces are assumed to be atomically smooth gold, with a Hamaker constant of 400 zJ for gold. The medium is assumed as air, with a relative permittivity of 1. The sphere was assumed to be made from gold ($\rho = 19300$ kg/m^3) for the weight calculation, and to have a voltage of 100 V for the electrostatic calculation in an air environment. For the capillary force, $\gamma = 0.0728$ N/m is chosen for water, with a contact angle of $\theta = 85°$.

close 0.2 nm contact with an infinite gold plane for comparison. Here it can be seen that the sphere weight dominates at larger scales, but that van der Waals and capillary forces begin to come into play for objects smaller than several mm in size. Electrostatic forces only become dominant at much smaller sizes of several microns. These scaling relations can change if different materials are used, or if the surfaces are not atomically smooth, which would decrease the surface force magnitudes.

2.1.2.2 Friction and Wear

Unlike friction modeled at the macro-scale, friction at the micro-scale can be adhesion controlled or load controlled. The friction can thus be both load and contact area dependent as

$$f = \tau_f A_f + \mu_f N \tag{2.18}$$

where τ_f is the interfacial shear strength, A_f is the real contact area, μ_f is the coefficient of friction, and N is the normal load. The interfacial shear stress can be approximated as one-third of the effective interface shear modulus [202]. The real contact area is complex to calculate, and depends strongly on the surface roughness. For relatively hard surfaces with low adhesion, i.e., $\lambda < 0.6$, the contact area A_f can be found using the DMT model as [101]

$$A_f = \pi \left[\frac{R_s}{K} \left(L_w + 2\pi R_s W_{12} \right) \right]^{2/3}, \tag{2.19}$$

where K is the interface stiffness and L_w is the vertical load on the sphere. The value is K is found from Equation (2.3). For relatively soft surfaces with high adhesion, i.e., $\lambda > 5$, the contact area is found as [101]

$$A_f = \pi \left[\frac{R_s}{K} \left(L_w + 3\pi R_s W_{12} + \sqrt{6\pi R_s W_{12} L_w + (3\pi R_s W_{12})^2} \right) \right]^{2/3}. \tag{2.20}$$

The shear stress in the friction analysis is thus

$$S = f/A_f = \tau_f + \mu_f P_i, \tag{2.21}$$

where P_i is the real local shear pressure. When two rough rigid objects contact, the real contact area would be less than the apparent contact

area due to asperity contact. For cases when the normal contact force is dominated by adhesion, a common method to reduce friction is to reduce the contact area by adding small bumps or ridges on surfaces in contact to serve as contact points with reduced contact area [84].

Wear is a critical problem for sliding interfaces in micromechanisms, necessitating the use of special material pairings to achieve useful lifetimes in fast-moving interfaces [223]. Problems of wear, friction, and adhesion can be avoided through the use of flexure joints as opposed to rotary joints [8, 196].

2.1.2.3 Fluid Mechanics

Many applications of micro-scale robots involve operation in fluids. The motion of microrobots by any method thus is subject to fluid forces. In this section we cover the governing equations of fluid mechanics, focusing on simplifications for motion at the micro-scale. Of particular interest for microrobot motion, we introduce fluid drag relations for translating and rotating bodies.

Using the principles of conservation of momentum, a fluid flow is governed by pressure, viscous, and body (gravitational) forces. This balance of forces is assembled in the Navier–Stokes equation

$$-\nabla P_f + \mu \nabla^2 u + \rho g = \rho \frac{Du}{Dt}, \tag{2.22}$$

where P_f is the fluid pressure, μ is the fluid viscosity, u is the fluid velocity, ρ is the fluid density, and g is the acceleration due to gravity. Here, $\frac{Du}{Dt}$ refers to the material derivative of the fluid velocity. This governing equation assumes the liquid as a continuous, incompressible, Newtonian medium, and neglects effects such as Brownian motion. The continuum model of fluid mechanics is valid at all scales in the realm of microrobotics. Solutions to this equation, using appropriate fluid boundary conditions, given the fluid velocity vector field. In many applications the gravitational (body) force term can be neglected, and we use a change of variables to analyze the relative magnitude of the remaining terms. Here we use the nondimensional variables $x^* = x/L_c$, $u^* = u/u_\infty$, and $P_f^* = P_f L_c/\mu u_\infty$, and divide by $\mu u_\infty/L_c$ to isolate terms on the left-hand side of the equation. Here, u_∞ is a characteristic velocity of the

fluid (such as the free stream velocity) and L_c is a characteristic length, such as an object dimension. Thus we arrive at the nondimensional form

$$-\nabla P_f^* + \nabla^2 u^* = \left(\frac{\rho u_\infty L_c}{\mu}\right)\frac{Du}{Dt}. \tag{2.23}$$

The term in parenthesis on the right-hand side of this equation is known as the Reynolds number $Re = \rho u_\infty L_c/\mu$, and is often interpreted as the ratio of fluid inertial to viscous forces. Thus, when Re becomes small, viscous forces dominate over inertial forces, resulting in creeping flow (Stokes flow), and can be thus described by the simpler equation

$$\nabla^2 u^* = \nabla P_f^*. \tag{2.24}$$

Fluid flow at the micro-scale, with small characteristic length L_c, is dominated by viscous forces as opposed to inertial forces. This flow would correspond to that seen at larger scales for low density, slow, or high viscosity flows.

Stokes flow has no dependence on time, and thus the solution for steady boundary conditions over all time only requires knowledge of the fluid state at a single time. In addition, the flow is time-reversible. Thus reciprocal motions, where a motion and its opposite are repeated over time, will result in no net forces exerted on the fluid. This is known as the *Scallop theorem* [165], and is a notable difference when comparing micro-scale versus larger-scale swimming methods.

The Stokes flow equation can be solved exactly by finding Green's function (here called a stokeslet), numerically by a boundary element method, or by experimental characterization. The solutions to several interesting cases are now given. These fluid flow solutions are used in modeling microrobot motion through fluids as well as in studies of the fluid flow generated by moving microrobots.

Viscous drag on a sphere

The fluid drag on any object at the micro-scale can be approximated by the drag on a sphere. As opposed to macro-scale high-Re drag analysis which includes multiple competing drag contributors such as viscous drag and form drag, Stokes flow drag is relatively simple, as it results only from viscous forces. The drag force across a wide range of laminar flow can be found using the empirically derived Kahn–Richardson

formulation for a sphere, F_{KR}, which is valid for a large range of small to moderate Reynolds numbers ($0 < Re < 10^5$) [168]:

$$Re = \frac{2\rho U R}{\mu} \tag{2.25}$$

$$F_{KR} = \pi R^2 \rho U^2 \left(1.84 Re^{-0.31} + 0.293 Re^{0.06}\right)^{3.45}, \tag{2.26}$$

where Re is a function of the sphere's radius R, the fluid velocity U, the fluid density ρ, and the dynamic viscosity of the fluid μ.

For small Re, this force can be simplified by using the viscous drag equation for a sphere at low Reynolds number [145], which provides results within 2.5% of the Kahn–Richardson model:

$$F_{drag} \approx 6\pi\mu R U. \tag{2.27}$$

Thus, the fluid drag force on a sphere in the low Re regime is proportional to the fluid viscosity, the sphere radius, and the fluid velocity. This simple model can also be applied to nonspherical shapes using a sphere of equivalent radius. Analytical solutions for such equivalent sphere radii for cases of ellipsoids, in addition to approximate correction factors for other geometries, are given in [32, 85].

Drag torque

Rotating bodies often appear in microrobotics. In a low Re environment, the drag torque on a rotating body can be solved exactly for an ellipsoid, and other shapes can be approximated by ellipsoids. The drag torque, assuming Stokes flow and an elliptical microrobot shape with major axis a and minor axis b, is given as [212]

$$\vec{T}_d = -\kappa_d V \mu \vec{\omega}, \tag{2.28}$$

where κ_d is the *particle shape factor*, given as

$$\kappa_d = \frac{1.6\left[3(a/b)^2 + 2\right]}{1 + \zeta - 0.5\zeta(b/a)^2}, \tag{2.29}$$

where

$$\zeta = \frac{1}{\epsilon^3}\left[\ln\left(\frac{1+\epsilon}{1-\epsilon}\right) - 2\epsilon\right] \tag{2.30}$$

and

$$\epsilon = \sqrt{1 - (b/a)^2} \quad (a \geq b). \tag{2.31}$$

Here, $V = \frac{\pi a b^2}{6}$ is the volume of the microrobot and μ is the viscosity. Thus, the drag torque is proportional to the fluid viscosity and the rotation rate.

Wall effects

When operating in fluid near a solid boundary, the torque required to rotate or translate a microobject increases. Liu and Prosperetti [125] studied a sphere of diameter D rotating about an axis perpendicular to a planar boundary in low Reynolds number environment, giving a far-field approximation for the increase in torque from the unbounded fluid torque T_d to the torque in the presence of the wall T_w at a distance d from the wall. This ratio is given as

$$T_w/T_d = [1 - \frac{1}{64}\left(\frac{D}{d}\right)^3 - \frac{3}{2048}\left(\frac{D}{d}\right)^8]^{-1}, \tag{2.32}$$

with a value of 1.202 being the exact maximum torque ratio when in contact with the wall. For a sphere rotating about an axis parallel to the boundary, the far-field approximation gives

$$T_w/T_d \approx 1 + \frac{5}{128}\left(\frac{D}{d}\right)^3. \tag{2.33}$$

These far-field equations are accurate for values of $\frac{D}{d}$ greater than approximately 1.2.

For translation without rotation parallel to a nearby wall, the increase in drag force as a function of the wall proximity is approximated by [59, 79]

$$F_w/F_d = \left[1 - \frac{9}{16}\left(\frac{D}{d}\right) + \frac{1}{8}\left(\frac{D}{d}\right)^3 - \frac{45}{256}\left(\frac{D}{d}\right)^4 - \frac{1}{16}\left(\frac{D}{d}\right)^5\right]^{-1}, \tag{2.34}$$

which is valid for values of $\frac{D}{d} < 10$ (i.e., large distances from the wall). Approximations for near-contact can be found in [79].

2.1.2.4 Thermal Properties

Actuation in micro-scale mechanisms is often accomplished through thermal expansion of materials. The thermal strain ϵ_t induced from a change in temperature ΔT is

$$\epsilon_t = \alpha \Delta T, \tag{2.35}$$

where α is the coefficient of thermal expansion. The value of α varies widely for different materials, meaning that dissimilar materials paired together will result in a bending along with expansion.

The heat lost through a surface due to conduction is proportional to the square of the surface area while the thermal energy it contains is proportional to the volume. Thus, a small object will conduct its heat quickly, requiring constant energy generation to maintain a high temperature. This can have a benefit that micro-mechanisms which are actuated by heating and cooling can be cycled quickly for high-speed operation. While thermal time scales with meso-scale objects can be on the order of minutes, at the microscale these scales can be seconds or less.

2.2 Energy Requirements

With the exception of biohybrid and chemically powered designs, all current microrobots have been powered by off-board power. On-board power sources such as chemical batteries will typically scale with the volume of the power source, and so not be easily used at small scales. Here we overview some of the challenges of powering microrobots using on-board or remotely delivered power. We will see that supplying on-board power for microrobot motion will be very challenging. However, on-board power for sensors or triggers could be more viable.

2.2.1 Required Power

The mechanical power required to move microrobots is dependent on the size scale and the operation environment. For constant motion, the mechanical power P is equal to the force required for motion F times the velocity v as

$$P = Fv. \tag{2.36}$$

The estimated mechanical power required for stated values of several microrobots in the literature can be compared, using estimated force and forward translational velocity values from the literature. The Mag-Mite resonant magnetic microrobot [71], which is about 300 μm in size, operates at forces of approximately 10 μN with 12.5 mm/s stated speeds, corresponding to an approximate power requirement of 125 nW. The Mag-μBot magnetic microrobot [155], which is about 200 μm in size, operates at forces of approximately 1 μN with 22 mm/s stated speeds, corresponding to an approximate power requirement of 22 nW. The OctoMag magnetic microrobot [115], which is about 2,000 μm in size, operates at forces of approximately 83 μN with 1.9 mm/s stated speeds, corresponding to an approximate power requirement of 340 nW. Here it is observed that micron-scale robots require *nanowatt*-level power. This level of power is quite low compared with macro-scale robotic systems, but is still too high to supply via on-board power supplies.

Sensors and microtools can potentially operate with much lower power than microrobot actuation, and therefore could be viable candidates to receive power from stored or scavenged power. We now overview some potential on-board power sources which can operate untethered at the microscale.

2.2.2 On-board Energy Storage

Voltaic cells transfer ions between anode and cathode materials across a conductive electrolyte. Microscale thin-film batteries have been made, although as battery storage capacity scales with volume, such storage techniques do not miniaturize well. The smallest electrochemical battery storage available in research stages are hundreds of nanometers thick thin-film construction, with energy densities of around 50 μAhcm^{-2} μm^{-1} and current densities of around 10 μAcm^{-2}, creating voltages of around 1.5 V. These cells have been fabricated in sizes of several mm. However, the integration and use of these sources smaller than 1 mm in size for untethered operation have yet to be done [33].

Another potential on-board power supply could be the harnessing of microstructured radioisotope power sources. Thin-film radioisotopes

have been shown to exhibit extremely long half lifetimes of up to hundreds of years with constant or pulsed power output and very large energy density. Such systems have been proposed for remote sensors [119], with typical energy density of 1–100 MJ/cm^3 but constant power output of only hundreds of picowatts. The low power available could limit their application for microrobot actuation unless intermittent motion from charged storage could be utilized. In fact, direct mechanical motion through a bending MEMS cantilever has been used as a storage mechanism for intermittent signal transmission in such systems [123], which could be explored for actuation purposes.

2.2.3 Wireless Power Delivery

To overcome the limitations with electrical energy storage, electrical power can be remotely supplied by wireless delivery. This has been performed inductively, optically, or with microwave radiation.

2.2.3.1 Wireless power transfer by radio frequency (RF) fields

Inductive power receivers can be made smaller than 1 mm using small pickup coils. These systems are driven by a transmitting coil with matched resonant frequency to the pickup coil. Using RF power transfer, the power P_r received is equal to

$$P_r = \frac{P_0 \lambda_w^2}{4\pi R_{tr}^2}, \tag{2.37}$$

where λ_w is the signal wavelength and R_{tr} is the distance between transmitter and receiver. Thus in ideal conditions the power delivered is proportional to $\frac{1}{R_{tr}^2}$, but in reality may decay even faster. Therefore, the distance between transmitter and receiver is a critical factor in such a design.

Such inductive power transfer has been used to deliver power up to tens of watts at distances up to several meters using large inductively coupled coils [116]. This work is significant in that it achieved very high transmission efficiency of about 40%. However, these technologies are only beginning to be used in actual wireless power applications at short

distances [180]. Indeed, as the power sent is proportional to the square of the receiving coil size, this technology will be very difficult to scale down for use in sub-mm robots.

Using a pickup coil on the order of several mm, Takeuchi and Shimoyama [204] delivered several mW of power using a high-Q receiving circuit. The electricity delivered in this example powered an electrostatic actuator. However, such a design has not been minimized to the size required for sub-mm robots.

A related method is power transfer through microwave energy [185]. Using a rectifying antenna, power has been wirelessly transmitted since the 1960s with high enough efficiency to power free-flying helicopters [26]. This technology has more recently been under investigation to power ground vehicles and portable electronic devices. Its use in miniature actuators for robotic use has been investigated [122]. In a typical application, a cm-scale in-pipe robot was able to move at 10 mm/s using a supplied microwave power of 200 mW [184]. However, the scaling of microwave rectifying antennas could pose a problem for future miniaturization of the technology.

2.2.3.2 Wireless optical power

Solar cells can be used to gather light radiation and convert it to electrical potential. The intensity of light from the sun outdoors is about 1.3 kW/m^2, although indoors the ambient light power density is only about 1 W/m^2. Most marketed solar cells are made from silicon, although gallium arsenide, amorphous silicon, and cadmium telluride designs are also made. A single solar cell creates a voltage potential of about 1 V, so arrays of such cells would be necessary to create the high voltages required for microrobotic piezoelectric or electrostatic actuators. Solar cells have advantages as a well-understood power source, although limited power density, low voltage output, and low availability of light in application areas could be major challenges. MEMS solar cells have been fabricated, with arrays generating tens of volts with μA-level current. An 8-mm walking robot has been made which uses MEMS solar cells to power an electrostatic leg system for propulsion [90]. These cells provide approximately 100 μW of power in a 3.6 $\times$ 1.8 $\times$ 200 μm^3

package with a mass of 2.3 mg. However, it could be difficult to miniaturize both the solar cell and associated electronics for sub-mm microrobotics use.

2.2.3.3 Energy scavenging

Energy scavenging takes advantage of natural mechanical vibration in the environment to generate electricity. This could be particularly well suited for high vibration areas such as on machinery or objects with which humans interact regularly. Many such vibration sources provide dominant frequencies between 60 and 200 Hz, with amplitudes from 0.1 to 10 m/s^2 [170]. Devices scavenge these vibrations using a free proof mass. This power can be harvested by piezoelectric [93, 117], magnetostrictive [216], electrostatic [143], or magnetic [222] elements. The electrical power available from a resonant system from oscillations of amplitude A_o is [12]

$$P_e = \frac{m\zeta_e A_o^2}{4\omega_o \left(\zeta_e + \zeta_m\right)^2}, \tag{2.38}$$

where ζ_e is the electrical damping ratio, ζ_m is the mechanical damping ratio of the oscillator, and ω_o is the oscillation frequency. Thus it is seen that the power is proportional to the oscillator mass, the square of the oscillation amplitude, and inversely proportional to the frequency.

Energy scavenging could also harvest energy from thermal gradients [198], fluid flow [91], or ambient radio waves [229]. However, these technologies may suffer from low conversion efficiency and difficulty in miniaturization.

2.3 Microrobot Fabrication

Traditional robot fabrication relies on the use of bulk materials machined using mills, drills, etc., and accommodates the incorporation of power, computation, and actuation on-board. These traditional techniques cannot be easily extended to the microscale, and so alternative microfabrication methods are used. Borrowing from the microchip and MEMS fabrication communities, microrobots are predominantly made using the methods of micromachining including

photolithography, material deposition, electroplating, and micromolding. Additional processes have also been explored. Laser micromachining using commercially available or custom setups can cut feature sizes directly down to tens of microns, but suffer from speed as a serial process. It is typically used for 2D part geometries, but can be used for some simple 3D cuts with low precision. Electro-discharge machining (EDM) can likewise machine metallic parts down to tens of microns in size, as another serial process. EDM is typically limited to 2D part geometries. As a promising additive manufacturing process at the micro-scale, 3D micro-stereolithography has been used to create high-resolution 3D shapes with features sizes of several microns out of plastic materials [20, 120], and can even be used for multimaterial construction [31]. This has been used to create 3D microrobot shapes which are functionalized using magnetic coatings [208] or included magnetic particles [227]. Micromachining using small traditional cutters such as end mills operating at high speed can also be used to create microscale features. These typically custom setups have been used to cut features tens of microns in size [63]. As a promising manufacture method for milli-scale robots, the Smart Composite Manufacturing (SCM) method can create layered mechanisms with integrated flexural joints with elements at the mm or cm-scale [8]. These mechanisms are designed in 2D, but are then folded to create complex 3D mechanisms [196]. However, this method will likely not scale down well to the sub-mm size due to the required assembly processes and reliance on complex layered designs.

Microrobotic parts are assembled using self-assembly or precision robotic micro-assembly. The techniques used depend on the functionality needed, with special materials required for magnetic actuation, and specific geometric components needed for all designs.

A major advantage of many microfabrication techniques is the parallel bulk nature. Commonly fabricated on a silicon wafer, hundreds or thousands of microrobotic parts are typically made on a wafer in a single process. Limitations of these techniques are that they typically only support 2D planar shapes, and the materials available for a particular process are limited. These techniques can be divided into wafer-level processes and pattern transfer [182]. In this section, we

also introduce other methods used in the fabrication of microrobots, including surface coatings, microassembly, and self-assembly and briefly cover the use of biocompatible materials for relevant applications.

2.3.1 Wafer-Level Processes

Wafer-level processes include cleaning and materials deposition. The first method of deposition is physical vapor deposition (PVD), which can be evaporation or sputtering. Evaporation can be used to deposit metals, and is commonly used for seed layers or electrodes. Sputtering uses an inert gas plasma to knock atoms from a target surface, which then reach the substrate to be coated.

Electroplating is used to deposit ions from solution onto a surface. Gold, copper, chromium, nickel, and iron–nickel magnetic alloys are commonly deposited with electroplating, and this method is capable of forming thicker layers than PVD, sputtering, or chemical vapor deposition.

Spin casting is a simple mechanical method of spreading a drop of liquid onto a wafer by spinning the wafer. Centrifugal forces balance with the solution surface tension to form a uniform thickness dependent on the spinning rate. This is the typical method to apply photoresist, which is later used in photolithography, and can form microrobotic structures or act as a masking layer for further processes.

2.3.2 Pattern Transfer

Microrobot designs can be transferred to the materials used by pattern transfer. In the commonly used optical transfer, light is selectively shown through a patterned photomask onto the substrate material. This substrate material is then selectively altered by the patterned light. One common optically sensitive material is photoresist, which forms cross-link bond in the presence or the absence of light. Thus, regions exposed by the mask become etch resistant or prone in subsequent chemical etching steps, leaving behind only an extruded structure corresponding to the mask shape.

Soft lithography is another method of pattern transfer which uses polymer molds to transfer patterns [225]. Poly(dimethylsiloxane)

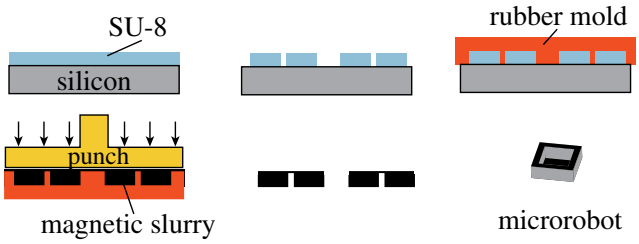

Fig. 2.2 Replica molding process based on photolithography, used to fabricate magnetic microrobots. This process allows for the creation of arbitrary 2D shapes at size scales from μm to mm scale.

(PDMS) or other rubbers are often used as the mold, and the master pattern is often created using lithography and etching from photoresist or silicon. Final parts can be created from polymers using the mold (shown in Figure 2.2) or the mold can be used for transfer printing of thin films. Soft lithography allows for reusable molds, and offers a simple, rapid method.

One relatively new fabrication method involves the inclusion of flexible elastomer elements in silicon features [74]. This allows for the creation of flexure hinges and elastic energy storage elements in a traditional MEMS process. This or similar processes could greatly increase the design freedom for microscale mechanisms in microrobotics applications.

2.3.3 Functionalization

Magnetic or electric functionalization of microrobot parts can be achieved through material choice and coatings. For magnetic actuation, a magnetic material such as nickel, iron, cobalt, or their alloys can be included as a bulk material, or as particles mixed into a polymer binder. Electrodeposited nickel or iron–nickel (Permalloy) can be patterned and formed to thicknesses of up to several hundred microns [231]. Ground particles of iron, iron oxide, or rare earth magnet materials can be included directly with photoresists [174], or in molded plastic parts [155].

For electrical functionalization, microrobot features can be made electrically insulating using a polymer construction, or conductive using metallic construction or coating.

Other functionalizations can be applied for passive remote sensing by chemical patterning, as shown in Ergeneman et al. for an optically excited and read oxygen sensor coating [58].

2.3.4 Precision Microassembly

While it is simplest to fabricate microrobots in their final form using bulk manufacturing techniques, it is also possible to assemble parts, especially to achieve out-of-plane 3D features. While manual methods such as tweezers can be used to assemble parts down to roughly 100 μm in size, precision assembly is only accomplished by robotic micromanipulation systems. In [231], multiple planar electroplated nickel parts of several hundred μm in size are assembled using such a system. These microassembly methods are serial processes which may not be compatible with bulk fabrication.

2.3.5 Self-assembly

An alternative to precision robotic assembly is so-called self-assembly, where micro-scale interaction forces between parts cause parallel assembly. Such behaviors have been shown for specially designed parts using capillary, magnetic, and electric forces at the microscale [136]. Compared with microassembly techniques, self-assembly can in general be done smaller, faster in parallel and in a self-correcting manner.

Self-assembly can be particularly useful in microrobotics to overcome the common limitation of 2D fabrication methods for microscale components. As one example of this, self-folding patterned 2D sheets have been shown to create complex 3D shapes as shown in Figure 2.3 [62] and shapes with advanced electrical characteristics [166]. Such capabilities could be used to create functional 3D microrobot features for locomotion, sensing, or form tools for manipulation of microscale parts at size scales down to tens of micrometers.

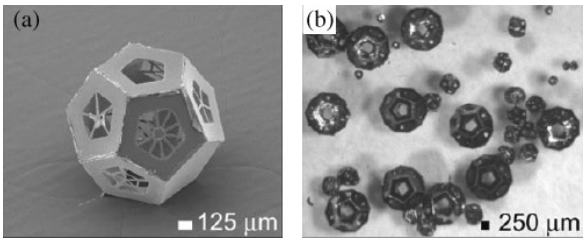

Fig. 2.3 3D polyhedra folded from 2D patterns using directed capillary self-assembly, from [62].

2.3.6 Biocompatibility

For biological applications in fluidic chips or medical applications inside the fluid cavities of the human body, biocompatibility of microrobots is a major concern. Many materials commonly used in microrobot fabrication are not biocompatible, including most magnetic materials. Most microrobot studies do not address biocompatibility, with one exception being [208], where mouse myoblasts are shown to grow on micron-scale IP-L and SU-8 photoresist microhelices. The use of surface coatings could render microrobots made from other materials biocompatible, although further study is required. For example, parylene or polypyrrole, common biocompatible polymers, could be coated over the other functional materials [164, 190, 194]. The use of such coatings in microrobotics is just beginning to be investigated, and warrants further study.

3

Approaches

This section provides a tutorial and review of the commonly used remote microrobot actuation methods. In light of the challenges associated with fabrication and control at the microscale, unique solutions have been developed to reliably deliver remote power and signals to untethered microrobots. We first introduce the main remote actuation methods that are used to power and control mobile microrobots from a practical perspective, namely magnetic and electrostatic actuation. The widespread use of magnetic and electrostatic actuation in the literature prompts us to focus largely on these methods when discussing the practical control of microrobots. We then review the specific approaches taken, and provide examples and case studies to illustrate the advantages and disadvantages of the different methods.

3.1 Actuation Methods

Before surveying the achieved mobile microrobot technologies, we will discuss some of the practical aspects of actuating microrobots remotely. This will allow the reader to understand the technical challenges and limitations associated with delivering power and signals. As they are

used so commonly and hold promise for use in many possible microrobot applications, we now review the creation of magnetic and electric fields for microrobot actuation from a distance.

3.1.1 Magnetic Actuation

Magnetic actuation is widely used for remote microrobot power and control. Due to their ability to penetrate most materials (including biological materials), magnetic fields are naturally suited to control microscale objects in remote, inaccessible spaces. It is possible to independently apply magnetic forces and torques onto a magnetic microrobot using the magnetic field and its spatial gradient, leading to a wide range of microrobot design and actuation possibilities. As we will see, magnetic forces and torques can be relatively strong, offering the ability to do work not possible with other actuation schemes. In addition, several magnetic materials can be integrated with existing microfabrication methods. While magnetic effects have been observed by man for millennia, developments in magnetic materials continue today, driven primarily by the magnetic motor and digital recording industries. New magnetic materials have been discovered within the last several decades, allowing for more freedom in magnetic actuator design, and significant increases in the magnitude of magnetic forces that can be applied.

Magnetic forces and torques are applied to move a microrobot using fields created using magnetic coils or permanent magnets outside the workspace. The magnetic force $\vec{F}_m$ exerted on a microrobot with magnetic moment $\vec{m}$ in a magnetic field $\vec{B}$, assuming that no electric current is flowing in the workspace, is given by

$$\begin{aligned} \vec{F}_m &= (\vec{m} \cdot \nabla)\, \vec{B} \\ &= \begin{pmatrix} \dfrac{\partial \vec{B}}{\partial x} & \dfrac{d\vec{B}}{\partial y} & \dfrac{\partial \vec{B}}{\partial z} \end{pmatrix}^T \vec{m}, \end{aligned} \tag{3.1}$$

and the magnetic torque $\vec{T}_m$ is given by

$$\vec{T}_m = \vec{m} \times \vec{B}. \tag{3.2}$$

Table 3.1. Typical magnetic material hysteresis characteristics. The first materials are referred to as magnetically "hard", while the last ones are "soft", and possess low remanence and coercivity.

Material	Coercivity (kA/m)	Remanence (kA/m)	Saturation M_s (kA/m)
SmCo	3,100 [35]	∼700 [35]	
NdFeB	620 [45]	∼1,000 [35]	
Ferrite	320 [45]	110–400 [35]	
Alnico V	40 [45]	950–1700 [35]	
Nickel	small	<1 [35]	522 [38]
Cobalt	small	<1 [35]	1120–1340 [11]
Permalloy (Ni–Fe)	small	<1 [35]	500–1250 [35]
Iron	0.6 [45]	<1 [35]	1732 [38]

Thus, magnetic torques are generated from the magnitude and direction of the applied field, and act to bring a magnetic moment into alignment with the applied field. Magnetic forces, however, are generated from the magnetic spatial field gradient, and operate on a magnetic moment in a less-intuitive manner. As we shall see later, by controlling both the magnetic field and its gradients in the microrobot workspace, it is possible to provide independent magnetic torques and forces.

Magnetic materials can be classified as either magnetically hard, retaining their internal magnetization in the absence of a magnetic field, or magnetically soft, having an internal magnetization that is dependent upon the applied field. Hard magnets, also called permanent magnets, are never truly permanently magnetized, but will behave as such until a large reverse field is applied to demagnetize them. Such a *coercive field* is typically much larger than the fields that are used to actuate microrobots, so the materials can often be treated as permanent. The strength of a permanent magnet after a saturating field is removed is referred to as the *remanence*, and is an indication of the strength of the material. The coercivity and remanence of some commonly used magnetic materials are given in Table 3.1.

The magnetic strength of soft magnets depends on the magnitude of the applied field $\vec{H}$ as

$$M = \chi|\vec{H}|, \tag{3.3}$$

where χ is the magnetic susceptibility of the material. Susceptibility varies greatly with material, and is only constant up to the saturation of the material. At applied fields larger than the saturation field, the magnetization is constant. For soft magnetic materials, the saturation magnetization can be a more relevant parameter than the remanence or coercivity, so these values are given in Table 3.1 also.

Two mechanisms of magnetism are typically dominant in materials used for microrobots, namely ferromagnetism and paramagnetism. The origin and study of ferromagnetism is complex, but it is the most common mechanism for most microscale magnetic robot materials. Some common ferromagnetic materials can be iron, cobalt, nickel, alnico, samarium cobalt (SmCo), and neodymium iron boron (NdFeB) and their alloys. In microrobotics applications, such materials are typically considered to be either perfectly soft or perfectly hard.

Paramagnetic materials are characterized as magnetically soft, and possess a low magnetic susceptibility χ. However, some materials such as iron oxides behave as *superparamagnets* when in fine powder form, possessing large susceptibility. Such submicron particles can possess large magnetic moments, and are commonly used in small magnetic microrobots. For a detailed description of the origin and behavior of ferromagnets and paramagnets, the reader is referred to [35].

While magnetic forces do play a part in the motion of magnetic microrobots, at certain scales their effect is small when compared to magnetic torques. For example, for a permanent magnetic microrobot with dimensions $250 \times 130 \times 100$ μm^3 and magnetization of $M = 200$ kA/m (typical for a microrobot molded from rare-earth magnet material), the magnetic force a typical electromagnet can apply, with a gradient of $\nabla B = 55$ mT/m, is approximately $F_m = 36$ nN. By comparison, using Equation (3.2), a magnetic torque of $T_m = 1.82 \times 10^{-9}$ Nm can be applied from the same coil with a field of $B = 2.8$ mT perpendicular to the direction of the microrobot magnetization. This torque, when treated as a pair of forces acting in opposite directions on the ends of the microrobot, acts as opposing forces each approximately 7.3 μN. Thus, the effects of magnetic torques can dominate microrobot behavior at this size scale and are often used for actuation. In some such cases, the magnetic force can be neglected for analysis.

Table 3.2. Units and conversions for magnetic properties [78]. To get SI units from cgs, multiply by the conversion factor.

	Symbol	cgs units	Conversion	SI units
Magnetic flux density	B	gauss	10^{-4}	tesla (T)
Magnetic field strength	H	oersted	$10^3/(4\pi)$	A/m
Volume magnetization	M	emu/cm^3	10^3	A/m
Magnetic moment	m	emu	10^{-3}	A m^2

The units of magnetism are notoriously difficult to understand. Both SI and cgs systems are used in the literature, with different governing relations for each system. Units for some magnetic vector properties are given in Table 3.2. The magnetic field and magnetic flux density are often used interchangeably in the microrobotics literature, and are related through the relationship

$$B = H + 4\pi M \quad \text{(cgs units)} \tag{3.4}$$

and

$$B = \mu_0 (H + M) \quad \text{(SI units)}, \tag{3.5}$$

where $\mu_0 = 4\pi \cdot 10^{-7}$ H/m is the permeability of free space. Outside a magnetic material, $M = 0$, so the B and H fields are proportional to each other. In some cases, B and H are thus used interchangeably for the magnetic field, although they do have distinct physical interpretations.

3.1.1.1 Magnetic field safety

For the use of magnetic fields penetrating the human body for remote actuation of mobile magnetic microrobots, the safety of high-strength magnetic fields can be a concern. However, the strength of a static magnetic field is not deemed dangerous upto 8 T [1, 177]. This very large field threshold is not likely to be encountered in any microrobot actuation methods. However, time-varying magnetic fields can potentially pose a risk due to heating of tissue. The U.S. Food and Drug Administration (FDA) guidelines suggests (as a nonbinding resolution) a range of safe amount of absorbed energy due to magnetic resonance imaging using large field changes over time, as measured by the specific

absorption rate (SAR) [1]. For whole-body absorption averaged over a 15-min period, this rate is 4 W/kg. Specific parts of the body such as torso or the extremities can experience larger SAR, as detailed in the report. The field-rate-of-change to generate these SARs will depend on the tissue details as well as on the field strength and rate of change. FDA guidelines suggest that the field rate of change should be less than 20 T/s, which is three times less than the rate of change observed to stimulate peripheral nerves [163]. Many institutions such as the Institute of Electrical and Electronics Engineers (IEEE) have published guidelines which generally limit the field rate of change to 0.1–1 T/s for frequencies of up to 100 Hz [140]. These rates of change can be encountered in some of the magnetic actuation systems used in the microrobotics community. However, devices utilizing large fields are approved for medical use on a case-by-case basis using this report as a general guideline, as the exact conditions for operational safety depend on many other factors such as body position and exposure time. Thus, devices using larger fields or field-rate-of-change can be approved for use. Most of the regulatory reports have focused on MRI exposure, and may not be directly applicable for other medical devices. Thus, regulatory hurdles could be present if high rate of change magnetic fields is required for a medical microrobot application.

Of course, even small magnetic fields may be dangerous if the patient has pacemakers, surgical implants, etc. In addition, the use of very large permanent or electromagnetic coils can also have safety considerations in the operation room. Just like an MRI operation room, the use of magnetic materials in such environments should be restricted.

3.1.1.2 Magnetic field creation

Magnetic fields for actuating magnetic microrobots can be supplied by magnetic coils or by large permanent magnets outside the microrobot workspace. Magnetic coils have the major advantage that they can deliver varying fields with no moving parts, and can be designed in a variety of ways to create spatially uniform magnetic fields and gradients. Permanent magnets, however, can provide large fields without the use of large electrical currents. The field in this case can be modulated

by translating or rotating one or more external magnets, but in general cannot be turned off without moving the external magnets far from the workspace. We first discuss practicalities of generating magnetic fields and gradients using magnetic coils.

Magnetic coils are often designed to surround all or part of the microrobot workspace. The field created is typically assumed to be proportional to the current through the coils, an assumption which is valid if there are no nearby materials with nonlinear magnetization hysteresis characteristics. The coil current I is governed by a differential equation (Equation (3.6)), and depends on the voltage V_c across the coil, the coil resistance R_a, and inductance L_a as

$$\frac{dI}{dt} = \frac{-1}{R_a L_c} I + \frac{1}{L_a} V_c. \tag{3.6}$$

The control input is the voltage on the coil, and the current can be sensed using Hall effect current sensors if precise feedback control is required.

The magnetic field produced by a cylindrical coil is found by applying the Biot–Savart law for each turn over the path S as [30]

$$\vec{B}_{ec}(x,y,z) = \frac{\mu_0 N_t I}{4\pi} \int_S \frac{\vec{dl} \times \vec{a}_R}{|\vec{r}|^2}, \tag{3.7}$$

where $\vec{B}_{ec}(x,y,z)$ is the magnetic field at the microrobot's position (x,y,z) due to the electromagnets, N_t is the number of wire turns in the coil, $\vec{dl}$ is an infinitesimal line segment along the direction of integration, $\vec{a}_R$ is the unit vector from the line segment to the point in space of interest, and $|\vec{r}|$ is the distance from the line segment to the point of interest.

The principle of superposition holds for multiple field sources (assuming that the workspace is free from soft magnetic materials), so the contributions from each coil can be summed to determine the total field. The full solution of Equation (3.7) is given in [70], and here we give only the axial component of this solution for brevity. The flux density for N_t round loops of radius a, parallel to the x–y plane, centered at $z = 0$, is given by

$$\vec{B}_z = \frac{\mu_0 N_t I}{2\pi} \left[K(k) + \frac{a^2 - \rho^2 - z^2}{(a-\rho)^2 + z^2} E(k) \right]. \tag{3.8}$$

Here, $K(k)$ and $E(k)$ are the elliptic integrals of the first and second kinds, respectively, which are given by

$$K(k) = \int_0^{\pi/2} \frac{d\theta}{\sqrt{1 - k^2 \sin^2 \theta}} \quad \text{and} \tag{3.9}$$

$$E(k) = \int_0^{\pi/2} \sqrt{1 - k^2 \sin^2 \theta} d\theta, \tag{3.10}$$

where

$$k^2 = \frac{4a\rho}{(a + \rho)^2 + z^2}. \tag{3.11}$$

A typical 2D magnetic coil setup is used in [28] to apply magnetic fields and gradients in-plane for 2D motion. This system uses orthogonal coil pairs to create these fields.

3.1.1.3 Special Coil Configurations

By pairing two coils along a single dimension, a special condition of spatial field or gradient uniformity can be obtained. Thus, the field can be assumed, within a small margin, to be invariant in space. To maximize the area of field uniformity, a Helmholtz configuration is used, where the space between the two parallel coils is equal to the coil radius [172]. By driving both coils equally in the same direction, a large region of uniform field is created between the two. This typically results in a nested configuration of the three orthogonal coil pairs is required due to the geometric constraints of using the Helmholtz configuration [130].

To maximize the area of field gradient uniformity, a Maxwell configuration is used, where the space between the two parallel coils is $\sqrt{2/3}$ times the coil radius and the coils are driven equally but in opposition to each other. It can be possible to combine independent Maxwell and Helmholtz coil pairs in one system to achieve both uniform fields and gradients.

3.1.1.4 Non-uniform field setups

Alternative coil configurations could have advantages when compared with the Helmholtz or Maxwell configuration, such as an increased

level of controllable microrobot DOFs, at the expense of reduced areas of uniformity [115]. To calculate the fields and gradients created from a general coil system, we can use the following relations

$$\vec{B} = \mathbf{B}\vec{I}, \tag{3.12}$$

$$\frac{\partial \vec{B}}{\partial x} = \mathbf{B}_x\vec{I}; \quad \frac{\partial \vec{B}}{\partial y} = \mathbf{B}_y\vec{I}; \quad \frac{\partial \vec{B}}{\partial z} = \mathbf{B}_z\vec{I}, \tag{3.13}$$

where each element of $\vec{I}$ is current through each of the c coils, $\mathbf{B}$ is a $3 \times c$ matrix mapping these coil currents to the magnetic field vector $\vec{B}$, and $\mathbf{B}_x$, $\mathbf{B}_y$, $\mathbf{B}_z$ are the $3 \times c$ matrices mapping the coil currents to the magnetic field spatial gradients in the x, y, and z directions, respectively. These mapping matrices are calculated for a given coil arrangement using Equation (3.8) or by treating the coils as magnetic dipoles in space and are calibrated through workspace measurements as outlined in Refs. [115, 141].

Thus, using Equations (3.12)–(3.13) with Equation (3.1) for a desired field and force on a single magnetic microrobot we arrive at

$$\begin{bmatrix} \vec{B} \\ \vec{F} \end{bmatrix} = \begin{bmatrix} \mathbf{B} \\ \vec{m}^T\mathbf{B}_x \\ \vec{m}^T\mathbf{B}_y \\ \vec{m}^T\mathbf{B}_z \end{bmatrix} \vec{I} = \mathbf{A}\vec{I}, \tag{3.14}$$

where $\mathbf{A}$ is the $6 \times c$ matrix mapping the coil currents $\vec{I}$ to the field $\vec{B}$ and force $\vec{F}$. The equation can be solved if $\mathbf{A}$ is full rank, i.e., the number of coils c is greater than or equal to 6. The solution can be accomplished for $c \neq 6$ through the pseudoinverse, which finds the solution which minimizes the 2-norm of $\vec{I}$ as

$$\vec{I} = \mathbf{A}^+ \begin{bmatrix} \vec{B} \\ \vec{F} \end{bmatrix}. \tag{3.15}$$

If $c < 6$, then the solution will be a least-squares approximation. Having greater than six coils leads to a better conditioned $\mathbf{A}$ matrix, which means a more isotropic workspace, reduction of singularity configurations, and lower coil current requirements. Systems designed to create such arbitrary 3D forces and torques have been created with six or

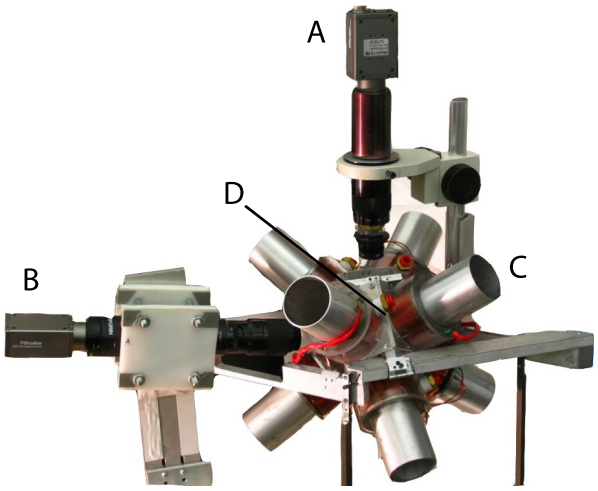

Fig. 3.1 Eight-coil system, capable of applying 5DOF magnetic force and torque in a several cm-sized workspace. This system is capable of applying fields of strength 25 mT and field gradients up to 1 T/m using optional iron cores. A: Top camera. B: Side camera. C: Magnetic coils. D: Workspace.

eight coils arranged around the workspace in a packed configuration, first shown in [141] for moving magnetic seeds through the brain and more recently for microrobot actuation (the Octomag system) in [115]. The Octomag system is designed to provide easy access to one face, so all coils are on one side of the workspace. A similar but smaller system was shown in [181]. Another system with the coils completely surrounding the workspace is shown in Figure 3.1. The distance of each coil to the center of the workspace is the same for all coils, and they are arranged along the vertices of a cube, with the four lower coils rotated 45° about the z-axis to break symmetry (which would result in a singular $\mathbf{A}$ matrix). Here, two cameras view the microrobot from the top and side.

3.1.1.5 Driving electronics

Control of the currents driving electromagnetic coils is typically performed by a PC with a data acquisition system at a high control bandwidth up to several kHz, and the coils are powered by linear electronic amplifiers with optional Hall-effect current sensors for feedback.

Coil currents of several A are typical, with higher currents used in conjunction with air or liquid cooling.

3.1.1.6 Fields applied by permanent magnets

In some cases it can be advantageous to use permanent magnets to create fields rather than electromagnets. Permanent magnets require no electrical power to generate and maintain a field, and thus are often well suited for creating large fields. However, modulating the field created by a permanent magnet requires moving or rotating the magnet. In addition, it is impossible in most cases to turn off the field created by permanent magnets, as is possible with electromagnets.

While complex changes to a magnetic field can be created by rotating arrays of permanent magnets in place such as in a Halbach array [21], many systems for microrobotics use a single external permanent magnet which is translated and rotated in space using a robotic actuator. Far from the external permanent magnet, the field can be approximated using the dipole model to simplify the calculations. The field $\vec{B}$ supplied by a magnetic dipole of moment $\vec{m}$ is given by

$$\vec{B}(\vec{m},\vec{r}) = \frac{\mu_0}{4\pi}\frac{1}{|\vec{r}|^5}\left[3\vec{r}(\vec{m}\cdot\vec{r}) - \vec{m}\,(\vec{r}\cdot\vec{r})\right], \tag{3.16}$$

where $\vec{r}$ is the vector from the dipole to the point of interest. While the dipole model is accurate in cases with a spherical external permanent magnet, the accuracy declines for other geometries, and may contain a significant error when the distance from the magnet is small. As rectilinear and cylindrical magnets are widely available from commercial suppliers, optimal aspect ratios have been found for these designs [159]. For rectilinear shapes, the best aspect ratio is 1:1:1, or a cube, and for cylinders magnetized along the axial direction, the best diameter-to length ratio is $\sqrt{4/3}$.

Many microrobot actuation schemes necessarily rely on rotating magnetic fields. A closed-form solution has been determined for the rotation axis of an external permanent magnet to create a desired magnetic field rotation at a point [129]. In this work it was shown that a simple linear transformation can map the desired microrobot rotation axis to the required rotation axis of the external permanent

magnet. Thus, the position of the external permanent magnet can be controlled independently of the required microrobot motion (with some constraints). Swimming microrobots have been shown to move using such methods, actuated by a single external permanent magnet tens of mm from the microrobot [68]. The permanent magnet in these cases is held by a multi-DOF robotic arm. Such results show that actuation using a single external permanent magnet could be sufficient for many clinical applications of microrobots inside the human body.

A related permanent magnet system called the Niobe (Stereotaxis) uses two very large permanent magnets moved with 3 DOF to create a field of approximately 80 mT over a space large enough to accommodate a human torso [209]. While this system is designed for steering magnetic catheters, it demonstrates that such permanent magnet systems are capable of being scaled up for clinical procedures.

3.1.1.7 Magnetic actuation by MRI

Magnetic actuation using a clinical MRI machine could leverage existing equipment infrastructure for navigating magnetic microrobots inside the human body. An MRI machine also has the potential to provide near-simultaneous microrobot localization in addition to propulsion.

Clinical MRI systems are designed for imaging and thus have several limitations for the propulsion of magnetic microrobots. Unlike the previously discussed magnetic coil systems which can control the coil currents in each coil independently, an MRI machine provides a static field down the length of the system. This static field is provided by large superconducting magnets, and typically can be 1.5 T or higher, especially in MRI systems used for research. Thus the MRI system is well suited for the control of soft magnetic microrobots because this large field can saturate most soft magnetic materials. It could also be used with permanent magnetic materials although the microrobot magnetization axis would be constrained to align with the static field direction. For imaging, magnetic field gradients up to $\sim$40 mT/m can be created in any direction. These gradients can be used for microrobot propulsion

by gradient pulling, and can potentially be increased through custom coil installations [131].

The excess heat created by the MRI system is also a major practical constraint. As the systems are designed for periodic imaging only, they cannot provide large duty cycles at full field gradient generation. Thus, for continuous microrobot propulsion, the system must be operated below its maximum achievable gradient field capabilities [137].

It has been shown that the gradients required for navigation in difficult areas such as the cardiovascular system could be achievable using a clinical MRI system depending on the microrobot size [137]. In [138] it is suggested that custom gradient coils with strength of 100–500 mT/m would be required to target tumors through the microvasculature using microparticles.

Due to these mentioned constraints, MRI-based control of microrobots in complex environments such as the human cardiovascular system requires sophisticated control algorithms. In [17], a high-level path planner is proposed to integrate the magnetic gradient steering and multiplexed feedback microrobot tracking. Such planning requires a detailed map of the environment, here acquired from preoperative MRI images. A trajectory is planned using the Fast Marching Method, and a controller is developed to guide the microrobot in the presence of time-varying blood flow. Model-based control with adaptive algorithms [10] has the ability to increase the quality and robustness of microrobot tracking in such environments where instabilities and unmodeled dynamics consistently appear.

3.1.2 Electric Field Creation

A common alternative to actuation by magnetic fields is the use of electric fields. These can exert attractive or repulsive forces at small distances up to tens of microns for microrobot actuation and control on a 2D surface or at larger distances in an electrophoresis setup.

Localized high strength electric fields are created by high voltage electrodes under the surface. These electrodes can provide actuation power to microrobots through capacitive coupling, which is used to

directly drive microrobots in [52]. In [156], the substrate upon which microrobots move has an array of independently controlled interdigitated electrodes to provide electrostatic anchoring for addressable multi-robot control. SU-8 is used as a barrier between the electrodes and the microrobot as it is inexpensive and has a high dielectric strength (112 V/μm), which will support the generation of the large electric fields necessary to anchor a microrobot without damaging the substrate. For experiments, a surface with four independent electrostatic pads was fabricated.

For the case of a conductive microrobot above an SU-8 insulation layer covering a set of interdigitated electrodes at an applied voltage difference of V_{id}, the conductor will assume a potential halfway between the two, or $V_{id}/2$, if it overlaps equal areas of electrodes at both voltages. With this assumption and considering negligible fringing, an estimate of the anchoring force F_{id} exerted by the interdigitated electrodes onto the microrobot is

$$F_{id} = \frac{1}{8} V_{id}^2 \frac{\epsilon_0 \epsilon_r}{g^2} A_{id}, \tag{3.17}$$

where A_{id} is the area of the electrodes overlapping the microrobot, g is the insulator thickness, ϵ_0 is the permittivity of free space, and ϵ is the relative static permittivity of the insulating material ($\epsilon = 4.1$ for SU-8).

Electrokinetic forces can also be used to pull electrically charged microrobots in fields of several V/cm at cm-length scales. The actuation system contains a central workspace chamber surrounded by four large electrode chambers containing an ionic solution (Steinberg's solution) [174].

3.1.3 Control/Vision/Planning/Learning

Due to the inherently unstable nature of actuation by magnetic fields [54], feedback control of such microrobotic systems is necessary to maintain a desired microrobot position or trajectory. A typical control system is shown in Figure 3.2. Here, the desired system input $\vec{p}_{\text{des}}$ is often a vector of position and orientation information, the size of which depends on the system DOF. The control system calculates a signal

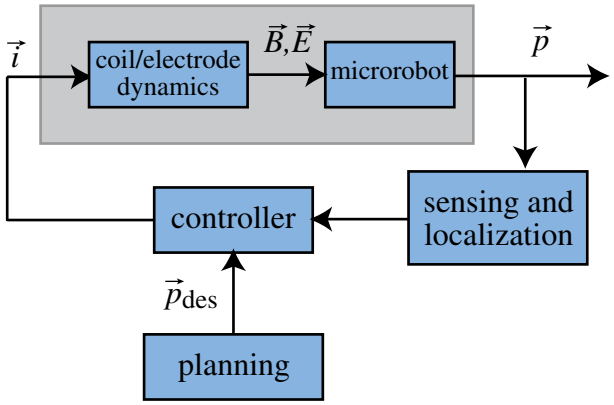

Fig. 3.2 Components of feedback control of a general microrobotic system.

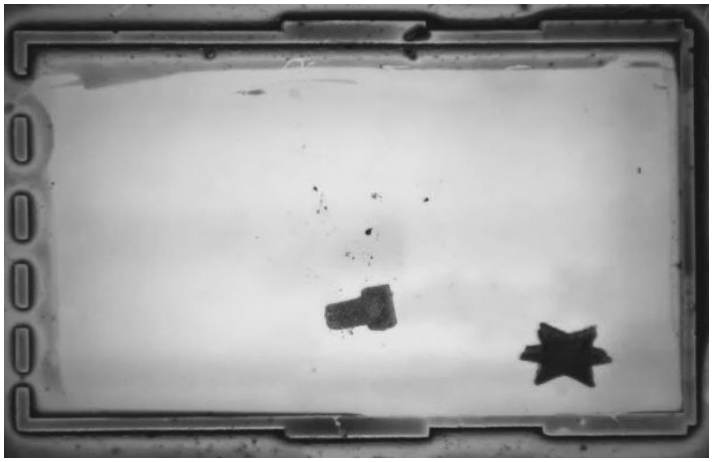

Fig. 3.3 A picture of a 500-μm star-shaped Mag-μBot pushing a plastic peg into a gap in a 2D planar assembly task. The arena width is 4 mm.

which is sent to the coil or electrode system as $\vec{i}$. The coil/electrode dynamics result in an electric or magnetic field $\vec{E}$ or $\vec{B}$ at the location of the microrobot. The position and possibly orientation of the microrobot is then observed using a microscope with machine vision or other localization scheme, which is fed back to the system controller.

Machine vision is often used to track the position of a microrobot. The task is to locate the microrobot in 2D or 3D space using one or more camera images in real time, and in the presence of optical noise

and a cluttered environment. In some cases where background clutter can be controlled, relatively simple processing algorithms using thresholding and centroid finding are adequate to reliably locate a microrobot. However, in other cases, the addition of background subtraction, edge finding, dilation, particle filter algorithms [154], colorspace evaluation [18], and other methods are required [111]. Knowledge about the size, shape, and color of the microrobot can greatly aid in these processes, as in the feature based tracking method (FTM). In FTM, features are determined from an object so that it can be recognized in any context. A scale invariant feature transform (SIFT) is then used to track the object under different image magnifications and rotations [126, 127]. A region-based tracking method is also commonly used when tracking with a relatively high frame rate, whereby tracked microrobots are assumed to be found in a location near the location found in the previous frame. As a further aid in microrobot localization, experiments can be performed in a low-clutter environment with high contrast background and lighting.

One challenge when operating a microrobot in 3D space is that a single camera can only easily provide 2 DOF position information. This problem can be addressed by using two cameras arranged orthogonally to each other [115] or by using subtle information contained in the image from a single camera. Such clues can rely on the changing size and shape of a microrobot when it moves out of plane, or rely on the predictable appearance of a defocused image which depends on the out-of-plane distance [224, 230]. This single-camera 3D tracking has been performed in the presence of the optical distortion of looking through the lenses of the eye through compensation [19].

In practice, image processing and control feedback are typically performed at tens of Hz on a desktop computer system. Such low feedback rates are usually limited by camera frame rates and image processing speed.

3.2 Microrobot Locomotion Methods

Remote actuation of microrobots has been the major topic of research in the field, resulting in a variety of actuation schemes. In general,

actuation methods leverage the unique balance of physical effects of small scales to overcome adhesion, friction, and fluid drag to move and execute tasks. Here we review some novel methods including actuation by magnetic and electric fields, light, chemical reactions, electroosmotic flow, piezoelectric effects, hydrophobic forces, and biohybrid propulsion using bacteria. Methods are capable of motion on 2D surfaces or in 3D fluid environments. These areas have been shown through proof-of-concept demonstrations as promising for untethered microrobot actuation. Other actuation methods, such as shape memory alloys [233] and electroactive polymers [102], ionic composite polymers [83], are commonly used for milli-scale robotic systems, but have not been commonly used in microrobotic applications due to challenges in remote power and fabrication. The coverage given here is not comprehensive, but is meant to expose the reader to the wide variety of actuation methods and discuss their relative benefits and limitations. While much progress has been made microrobot actuation methods, this is still an active area of research.

3.2.1 Magnetic Crawling

Crawling or walking on 2D surfaces using magnetically actuated microrobots has been explored using a number of different approaches, spanning a wide length scale. These approaches use a combination of magnetic gradient pulling forces, induced torques, and internal deflections to achieve translation across a 2D surface. While magnetic forces can be used to move microrobots, such forces are relatively weak compared with those resulting from magnetic torques [34]. Thus, many actuation methods make use of strong magnetic torques, for crawling in 2D. One major challenge addressed in these designs is overcoming high surface friction and adhesion. Many designs use a vibrating motion to periodically break the adhesion to allow for controlled motion with constant velocity. These approaches have accomplished fast and precise motion with full 3 DOF position and orientation control. Some of the methods are reviewed here.

The Mag-Mite system [71] uses low strength, high-frequency fields to excite a resonant microrobot structure for smooth crawling motion.

Speeds of tens of mm/s are achieved in an air environment, and lower speeds in liquid. The $300 \times 300 \times 70$ μm microrobot consists of two magnetic masses which are free to vibrate relative to each other, connected by a meandering microfabricated spring. The high-speed oscillation helps break static friction. Due to the small size of the microrobot, the resonant frequency of this oscillation is several kHz. The Mag-Mite is steered by applying a small DC field which orients the entire microrobot in the plane. Motion reliability is increased through the use of a structured electrode surface which adds asymmetric clamping forces to increase the directed motion amplitude. A version with increased biocompatibility is made using polymer springs with ferromagnetic masses using a simpler manufacturing process and similar performance [210].

A thin microrobot can be driven by the magnetostrictive response of certain materials. Magnetostriction is the internal realization of magnetic field-induced stress, analogous to the piezoelectric effect which is electric field induced. Using terfenol-D as a high-strain material, several microns of steady-state deflection are created in a 580 μm microrobot. By driving with a 6-kHz pulsed magnetic field, a steady walking motion is achieved, with stated velocities up to 75 mm/s achieved in the NIST mobile microrobotics competition in 2010 [106]. Using controlled gradient fields, limited 2D path following is also achieved with this method.

A magnetic-torque-based approach has been implemented which allows for a simple magnetic microrobot to translate using stick-slip actuation, termed the Mag-μBot system [155]. Due to the relatively strong magnetic torques which can be created from small magnetic fields, this approach is robust to environmental disturbances such as debris surface roughness or fluid flow at scales of tens to hundreds of microns. This method has been demonstrated in air, liquid, and vacuum environments, and thus is appealing for use in a variety of microrobotics applications. One major advantage is that the pulsed stepping motion results in small steps with a known step size. By regulating the pulsing frequency and angle sweep of each step, step sizes can be reduced to several microns. Additionally, the microrobot can be driven using large steps in conjunction with magnetic field gradients at speeds of several hundred mm/s, albeit with less precision control capability. This

approach has also been used in [173] at a smaller length scale down to tens of microns. An even simplier method using magnetic torques is a rolling magnetic microrobot [105].

3.2.2 Case Study: Stick-Slip-Based Walking

As a case study, we will now study the dynamics of microrobot crawling motion using stick-slip dynamics, as presented in [155]. This locomotion method results in consistent and controllable motion in the presence of high surface adhesion forces which tend to restrict microrobot motion. High-strength magnetic pulling forces can be used to move the microrobot, but in this case the microrobot will experience high accelerations, leading to unpredictable behavior. To move reliably, a rocking motion is induced in the microrobot by using time-varying magnetic fields, which results in a controllable stick-slip motion across the surface using only magnetic torques, with no magnetic forces being required. In this method the microrobot is rocked back and forth, with the microrobot angle being described by a sawtooth waveform. This results in a small slip to occur when the field angle is reduced quickly, and a sticking phase when the angle is increased slowly. This period is referred to as one step, and to study the motion in detail the microrobot dynamics must be studied in full. As these dynamics are described by piece-wise functions when the microrobot is in contact versus out-of-contact with the surface, a computer numerical simulation is used to solve for the motion.

To simulate the dynamics of the magnetic microrobot in [155], only motion in the x–z plane is modeled, as shown in Figure 3.4. The robot has a center of mass (COM) at $\vec{X}$, an orientation angle θ measured clockwise from the ground, a distance r from its COM to a corner, and an angle $\phi = \tan^{-1}(H/L)$ determined from geometry. The robot experiences several forces, including its weight, mg, a normal force from the surface, N, an adhesive force to the surface, F_{adh}, an x-directed externally applied magnetic force, F_x, a z-directed externally applied magnetic force, F_z, a linear damping force in the x-direction, L_x, a linear damping force in the z-direction, L_z, an externally applied magnetic torque, T_y, a rotational damping torque, D_y, and a Coulomb

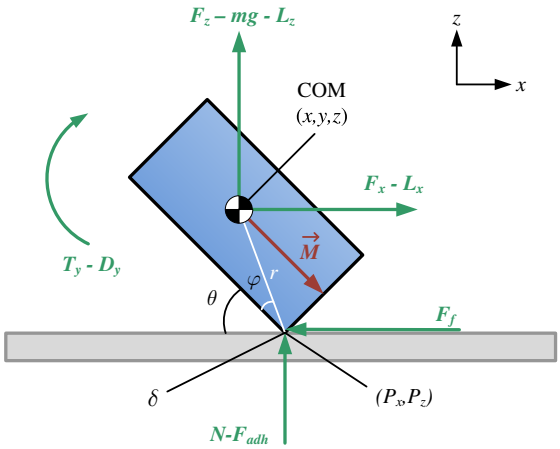

Fig. 3.4 Schematic of a rectangular magnetic microrobot with applied external forces and torques. Here, the typical dimensions are several hundred microns on a side, and the microrobot is made from a mixture of NdFeB magnetic powder and a polyurethane binder. The magnetization vector is denoted by $\vec{M}$. The external forces include the magnetic force and torque F, T, the fluid damping force and torque L and D, the friction force f, the adhesion force F_{adh}, the weight mg, and the normal force N.

sliding friction force F_f. F_f depends on N, the sliding friction coefficient μ, and the velocity of the contact point, $\frac{dP_x}{dt}$, where (P_x, P_z) is the bottom-most point on the microrobot (nominally in contact with the surface). Using these forces, we develop the dynamic relations:

$$m\ddot{x} = F_x - F_f - L_x \tag{3.18}$$

$$m\ddot{z} = F_z - mg + N - F_{adh} - L_z \tag{3.19}$$

$$\begin{aligned} J\ddot{\theta} = {} & T_y + F_f \cdot r \cdot \sin(\theta + \phi) \\ & -(N - F_{adh}) r \cdot \cos(\theta + \phi) - D_y \end{aligned} \tag{3.20}$$

where J is the polar moment of inertia of the robot, calculated as $J = m(H^2 + L^2)/12$.

In the simulation, the robot is first assumed pinned to the surface at (P_x, P_y), where $0 < \theta < \frac{\pi}{2}$. This gives the following additional equations:

$$\begin{aligned} x &= P_x - r \cdot \cos(\theta + \phi) \\ \ddot{x} &= \ddot{P}_x + r\ddot{\theta}\sin(\theta + \phi) - r\dot{\theta}^2 \cos(\theta + \phi) \end{aligned} \tag{3.21}$$

$$\begin{aligned} z &= P_z + r \cdot sin(\theta + \phi) \\ \ddot{z} &= \ddot{P}_z + r\ddot{\theta}\cos(\theta + \phi) - r\dot{\theta}^2 \sin(\theta + \phi) \end{aligned} \tag{3.22}$$

To solve Equations (3.18)–(3.22), we realize that there are seven unknown quantities (N, $\ddot{\theta}$, $\ddot{x}$, $\ddot{z}$, $\ddot{P}_x$, $\ddot{P}_z$, F_f) and five equations, indicating an under-defined system. As the stick-slip motion in this system is similar to the case outlined by Painlevé's paradox, we resolve the paradox by taking the friction force, F_f, as an unknown value (instead of assuming $F_f = \mu N$) [199]. Using the pinned assumption, we can set $\ddot{P}_x = \ddot{P}_z = 0$; then, Equations (3.18)–(3.22) are solved analytically. There are three possible types of solutions that can occur during each time step:

Case 1: The solution results in $N < 0$ (an impossible case). This implies that the pinned assumption was false, and the microrobot has broken contact with the surface. Equations (3.18–3.22) are resolved using $N = 0$ and $F_f = 0$, with $\ddot{P}_x$ and $\ddot{P}_z$ as unknowns.

Case 2: The solution results in $F_f > F_{fmax}$, where $F_{fmax} = \mu N$. This also implies that the pinned assumption was false, and the point of contact is slipping. Therefore, the robot is translating in addition to rocking. Equations (3.18)–(3.22) are resolved using $F_f = F_{fmax}$, $\ddot{P}_z = 0$, and $\ddot{P}_x$ as an unknown.

Case 3: All of the variables being solved for are within physically reasonable bounds. The robot is in contact with the surface at the pinned location and is rocking in place.

When a satisfactory solution for all seven variables is reached in each time step, these solutions for acceleration are used in the solver to determine the velocities and positions, which are in turn used as initial conditions in the next time step.

3.2.2.1 Solver

To simulate the microrobot's motion, a fifth order Runge–Kutta solver is used to solve the time-dependent system. A magnetic pulsing signal is given as a voltage waveform, and the magnetic field is solved for. With given initial conditions, the magnetic force and torque equations are used to determine the magnetic field forces, and Equations (3.18)–(3.22) are solved for the three position states of the microrobot: x, z, and θ. An example simulation case is compared with the experimental results in Figure 3.5. Here it is seen that the simulation and

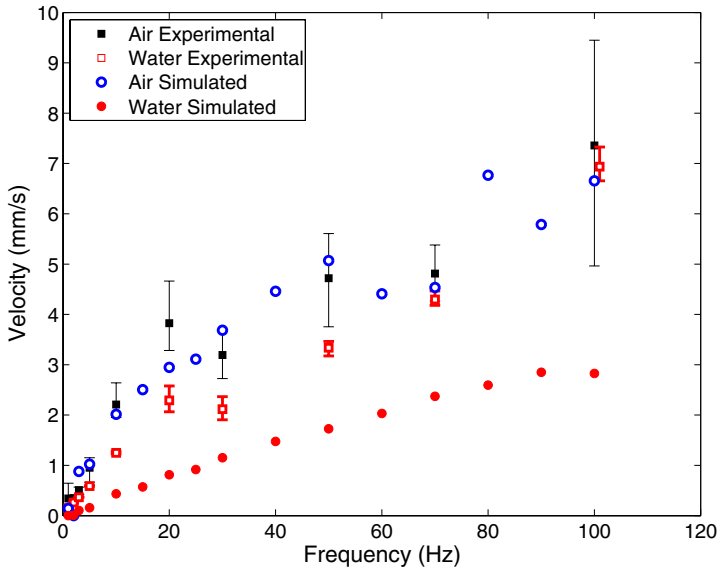

Fig. 3.5 Example comparison of experimental and simulation microrobot speed values, from [155] using stick-slip motion on a flat silicon surface. Average microrobot speeds are given for operation in two different operating environments, air and water. Error bars denote standard deviation in experimental results.

experimental results can match in some cases but vary widely in other cases, where the only change is a single material change. This highlights the sensitivity of the microrobot motion to microscale friction and adhesion parameters, which are difficult to measure accurately. Also note the relatively large error bars in the plot, which demonstrate the stochastic nature of the motion.

From this case study we see that many different forces can play a significant role in microrobot motion, including friction and adhesion, fluid drag, and body inertia. The relative force magnitudes encountered in this case study are summarized in Table 3.3. The strong nonlinearities associated with some of these forces highlight the need for analytical, numerical, or even finite-element solutions as indispensable *design tools* for studying and designing microrobot motions. To study the scaling of this particular motion method, we directly compare these physical forces for an isometric scaling of the microrobot size in Figure 3.6. Here, we scale the microrobot size while keeping the actuating coils and

Table 3.3. Approximate force magnitudes encountered in the magnetic microrobot stick-slip walking case study. Torques are treated as a pair of equivalent forces at opposite ends of the microrobot. For these comparisons, we assume a microrobot approximately 200 μm on a side with magnetization 50 kA/m, operating in a water environment on glass at a speed of tens of body-lengths per second in an applied field several mT in strength. Torques are treated as a pair of equivalent forces on opposite ends of the microrobot.

Force	Approximate magnitude
Magnetic torques	1s of μN
Fluid damping torques	1s of μN
Friction forces	100s of nN
Normal forces	100s of nN
Adhesion	100s of nN
Weight	100s of nN
Magnetic forces	10s of nN
Fluid damping forces	1s of nN

coil-workspace distance constant as these will likely be fixed in a real microrobot application. We see that magnetic and fluid drag torques dominate the motion of the microrobot down to size scales of tens of microns. The relatively small size of the magnetic forces at sizes smaller than 1 mm motivates the use of microrobot propulsion methods which utilize the magnetic torque.

Of interest when scaling below tens of microns in size is the increasing effect of thermal fluctuations, which lead to Brownian motion. As a rough indication of the strength of such forces, we can approximate the equivalent thermal forces by using the Stokes fluid drag equation (Equation (2.27)), where we find the velocity using the average thermal energy relation $\frac{1}{2}m\bar{v}^2 = \frac{3}{2}k_BT$, where m is the mass, $\bar{v}$ is the average velocity, $k_B = 1.38 \times 10^{-23}$ J/K is Boltzmann's constant, and T is the temperature in kelvin. This relation thus will give us an indication as to the induced thermal fluctuation forces acting on a microsphere. When this force is calculated for a 1-μm diameter sphere of density 4,500 kg/m^3 at 293 K, we arrive at an equivalent approximate force of 1.6×10^{-11} N. However, a similar object slightly larger at 10 μm experiences an equivalent thermal force of only 5.2×10^{-12} N. Thus, it can be seen that such thermal fluctuations could dominate the motion of microrobots of several microns or smaller.

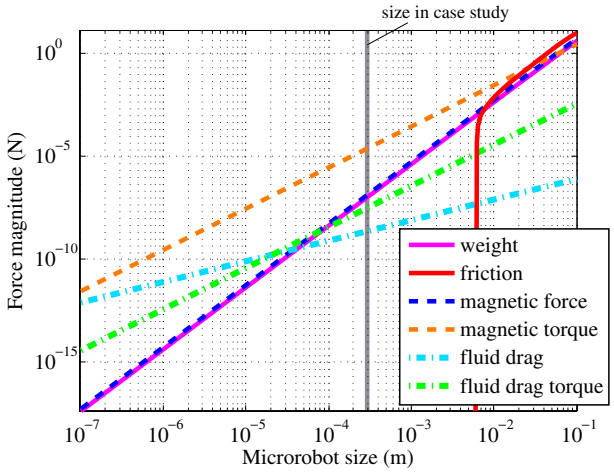

Fig. 3.6 Mag-μBot force scaling from the case study. Equivalent forces are computed from torques by dividing by the microrobot size. The fluid environment is assumed as water with viscosity $\mu = 8.9 \times 10^{-4}$ Pa·s, and the microrobot density is 5,500 kg/m^3. The microrobot velocity is 1 mm/s and its rotation rate is taken as swinging through an angle of 40° at a rate of 50 Hz, or about 70 rad/s. The magnetic field is taken as 6 mT and the field gradient as 112 mT/m, with a microrobot magnetization of 50 kA/m. To calculate surface friction, the interfacial shear strength is taken as one-third the shear strength, as $\tau = 20$ MPa and the contact area is varying with load as given in Equation (2.19). The gap size for adhesion calculation is taken as 0.2 nm. The coefficient of friction μ_f is taken as 0.41. The work of adhesion W_{132} is calculated in water for the surfaces polyurethane and silicon, and is found to be negative, indicating repulsion. This material pairing was chosen specifically to yield this negative value. This results in a steep drop in the friction force when the microrobot weight overcomes this repulsive force at a microrobot size of about 7 mm. In a model with nonsmooth surfaces, the friction would be positive at smaller scales.

3.2.3 Magnetic Gradient Pulling

For motion in 3D, magnetic field gradients can be used to directly exert forces on a microrobot strong enough for levitation. Due to high accelerations possible with microscale components, high damping is often required to maintain control with this method. While larger robotic systems at the mm-scale have achieved controlled levitation in air [57] using high-speed feedback control, microscale systems have been limited to operation in liquid environments. To manipulate a rigid-body magnetic microrobot in 3D levitation requires a high level of control. This is accomplished with a set of electromagnetic coils arranged around the workspace which can simultaneously control the

field and field gradient directions. Building on the work of Meeker et al. [141], a system capable of manipulating microscale robots uses eight independently controlled electromagnets, dubbed the OctoMag system, as shown in Figure 3.2 [115]. Such a system can achieve 5 DOF control of a simple magnetic microrobot for levitation in liquid. The sixth DOF, rotation about the magnetization vector, is not controllable unless creative use of magnetic anisotropy in complex soft-magnetic shapes is considered [3]. In the OctoMag system, precise 3D position and 2 DOF orientation control of soft-magnetic or permanent microrobots is demonstrated in a workspace of several cm, in a high viscosity silicone oil.

3.2.4 Magnetic Swimming

Swimming in low-Re environments requires methods different from large-scale swimming. Since the first published in-depth study of the fluid mechanics of such swimming in 1951 [205], many fluid dynamics studies have been conducted to understand these propulsion styles, as reviewed in [121]. Two primary means of swimming have been demonstrated at the microscale, both of which are inspired by biological methods: helical propulsion and flapping wave propulsion. These two methods are shown conceptually in Figure 3.7. In helical swimming, a rotary motion activates a helical-shaped body to propel through the viscous liquid. The fluid mechanics of helical swimming devices has been studied in depth, and the reader is referred to [160, 161] for a full review. In short, torque is generated in microrobotic helical swimmers using a magnetic head or tail and a uniform rotating magnetic field. The tail of such a swimmer is typically fabricated to be stiff, and can be formed using stress-engineered curling thin films [236], wound wire [92], by glancing angle deposition [75], or microstereolithography [227].

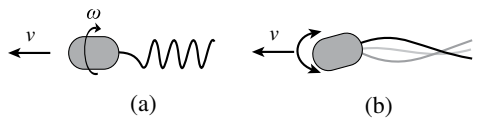

Fig. 3.7 Microscale swimming methods. (a) Rotation of a stiff helix. (b) Oscillation of a head propagating through an elastic tail.

The swimming force and torque on a rigid body are determined for a known rotation rate ω, applied driving torque τ, applied driving force f, and forward velocity v as [165]

$$\begin{bmatrix} f \\ \tau \end{bmatrix} = \begin{bmatrix} a & b \\ b & c \end{bmatrix} \begin{bmatrix} v \\ \omega \end{bmatrix}, \tag{3.23}$$

where the matrix parameters a, b, and c can be determined for the shape geometry. For a helix with helix angle θ, these are given as

$$a = 2\pi n D \left(\frac{\xi_{\parallel} \cos^2\theta + \xi_{\perp} \sin^2\theta}{\sin\theta} \right), \tag{3.24}$$

$$b = 2\pi n D^2 \left(\xi_{\parallel} - \xi_{\perp} \right) \cos\theta, \tag{3.25}$$

$$c = 2\pi n D^3 \left(\frac{\xi_{\perp} \cos^2\theta + \xi_{\parallel} \sin^2\theta}{\sin\theta} \right), \tag{3.26}$$

where n is the number of helix turns, D is the helix major diameter, r is the filament radius, and $\xi_{\parallel}$ and $\xi_{\perp}$ are the viscous drag coefficients found by resistive force theory parallel and perpendicular to the filament, respectively as [124]

$$\xi_{\perp} = \frac{4\pi\eta}{\ln\left(\frac{0.18\pi D}{r \sin\theta}\right) + 0.5} \text{ and} \tag{3.27}$$

$$\xi_{|} = \frac{2\pi\eta}{\ln\left(\frac{0.18\pi D}{r \sin\theta}\right)}. \tag{3.28}$$

As a second method of swimming, traveling wave propulsion uses an elastic tail driven by an oscillating head affixed at one end, as seen in Figure 3.7(b). This oscillation is transmitted down the filament as a traveling wave. Analyzing such motion requires solution of a coupled elastic–hydrodynamic interaction, and is thus quite complex. Approximate solutions have been found for small deformation with impulsive or oscillatory inputs [221] and by using numerical simulation [118], but no full analytical solution is available.

This type of actuation has been demonstrated at very small scales using magnetic field actuation. In [53], a crude traveling wave is induced in a 24-μm flexible filament attached to a red blood cell. As the filament

in this case is symmetric, the presence of the red blood cell acts to break the symmetry and allows for motion. It is also shown that other methods of breaking the symmetry of such swimmers are also effective, such as the presence of a local filament defect [169].

In [5], a detailed comparison of magnetically powered swimmers is performed, and it is found that helical and traveling-wave microsystems exhibit similar performance in terms of swimmer velocity for a given driving torque and that both swimming methods compare favorably to magnetic gradient pulling as the microrobot size decreases.

3.2.5 Light Propulsion

Focused light energy can be used to remotely actuate a microrobot by heating or momentum transfer. These approaches require line-of-sight access to the microrobot, but have some benefits such as potential for simultaneous multirobot control using multiple light sources.

In [201], a microrobot resting on thin metal bimorph legs is actuated by thermal expansion caused by a focused laser. By applying an asymmetric excitation, the dynamic heating, and cooling behavior results in a forward step hundreds of nm in size. This can be applied with periods of several ms, resulting in directed crawling motion with speeds up to 150 μm/s. Because the motion relies on thermal gradients throughout the structure, a minimum device size of approximately 5 μm is stated. Below this size the heating covers the entire microrobot instead of being restricted to a single leg, resulting in no motion. Such a laser-based excitation method is limited to crawling on smooth 2D surfaces. In another approach, light pressure is used to push 5 μm wedge-shaped "sailboats" across a flat surface [27]. The driving pressure of approximately 0.6 Pa arises due to momentum transfer from the reflected light, and drives the microrobots at a speed of about 10 μm/s.

A third method propels an air-bubble microrobot in liquid by localized heating using a focused laser or other light [96]. In this method, thermocapillary effects move the air bubble toward higher temperature regions. Thus, the bubble follows a light spot focused on the substrate. In this setup, an air bubble is to be created and trapped in a thin layer of water or oil approximately 300 μm in thickness. Bubble

motion has been created with bubbles in the 100–500 μm size range, and at relatively high speeds up to 1.5 mm/s.

3.2.6 Electric Field Propulsion

While electric fields are used secondarily in several microrobot actuation schemes, some designs use the electrostatic force as direct actuation. In [51], an MEMS-designed scratch drive actuator is used to locomote on a 2D electrode surface in an air environment. Through careful design, an untethered actuator is achieved which can be steered through the use of an integrated turning arm [50]. The actuator is 200 μm in width, and consists of a flat plate suspended slightly above the substrate. When high strength electric fields are applied, the plate bends downward toward the substrate. Through an asymmetric driving pattern, a stick-slip crawling motion is achieved, with step sizes less than 10 nm. By applying these steps quickly, speeds up to 1.5 mm/s are achieved. These scratch-drive microrobots are maneuverable in space when a very high voltage is applied to the substrate, which pulls the turning arm into contact with the surface. In this reversible state, the microrobot rotates about the arm contact point.

Electric fields can also be used to pull directly on charged objects in a fluid by the Coulomb force. In Sakar et al. [174], a hybrid actuation approach is used whereby DC electric fields of several V/cm in strength apply electrokinetic force to a charged microrobot body. The electrophoretic force is proportional to the electric field magnitude and the charge on the object. Speeds of up to 7 μm/s are achieved using a 20×22 μm^2 microrobot in this way.

A major limitation of electrostatic actuation is the necessary requirement for electrodes in the workspace. As high field strengths are typically required, this could also limit applicability for biological or remote environments.

3.2.7 Chemical Propulsion

Chemical reactions could provide a remote and replenishable power supply for microrobots. In [193], a micron-scale tube is used as a "jet" for motion in 3D through liquid. Propulsion comes from a stream of

oxygen bubbles which form inside the tube through a catalytic reaction with the liquid medium. These tubes of length 100 μm are made from layered Ti–Fe–Au–Pt which rolls up passively due to residual stress. The Pt inner layer is allowed to react with the H_2O_2 solution to form oxygen gas inside the tube. As the 5.5 μm diameter tube is naturally larger on one end, the bubbles exit from this end, and new solution is drawn in through the narrow end to feed the reaction. With frequent bubble ejection, speeds up to 2 mm/s are observed. By integrating a magnetic Fe/Co layer into the assembly, the orientation of the tube can be controlled using low strength magnetic fields for steering in 3D.

The nature of chemical propulsion could lead it to be difficult to use for operation in arbitrary fluid environments. In addition, it could be difficult to harness such chemical reactions for sophisticated feedback control.

3.2.8 Electrochemical and Electroosmotic Propulsion

Electric fields in a fluid can be used to create electoosmotic propulsion for swimming microrobots. Such methods can be compatible with living organisms, and could be used in conjunction with other actuation methods. Electroosmosis puts to use a natural electrical diffuse layer which surrounds any object in liquid. This layer is typically tens of nanometers thick, and contains a nonzero electric potential called the zeta potential ζ. In an electric field the ions in this layer are pulled in the field direction. This motion drags the surrounding liquid, resulting in hydrodynamic pressure on the body, the speed of which depends on the zeta potential. A microrobot which moves using this method utilizes a large surface area-to-volume ratio to increase the propulsive force, but can be made in any shape. One example maximizes the surface area by using a helical shape [98]. This swimmer is made of n-type GaAs, which adopts a negative charge in water. Using a 74 μm helix and a 240 V/mm electric field magnitude, a max speed of 1.8 mm/s was achieved.

Requirements for high-strength electric fields could limit the use of electrochemical or electroosmotic actuation in biological applications.

3.2.9 Piezoelectric Propulsion

Due to high levels of surface adhesion and friction in small-scale robotics, the breaking of this stiction is a major concern. One solution has been through the use of the high accelerations possible with piezoelectric materials. These materials experience strain in the presence of electric fields, and are typically driven by high voltage potentials of several hundred volts. In [28], a lead zirconate titanate (PZT) piezoelectric element is integrated with a magnetic layer to form a hybrid microrobot. To actuate, a high voltage impulse is applied between two electrode layers above and below the microrobot, and the generated strain in the PZT causes the microrobot to jump slightly, breaking the surface adhesion and momentarily reducing translational friction. High-strength magnetic field gradients supplied by magnetic coil pairs then act to pull the microrobot in the desired direction. Using this method, very high translational velocities up to nearly 700 mm/s can be achieved, although precise control of microrobots at such high speeds is very challenging. As the dynamics of such actuation are very fast, precisely modeling the behavior of this actuation style is difficult. Due to high accelerations and velocities, this method also may not be well suited to fine manipulation or assembly tasks.

More sophisticated use of piezoelectric elements in mechanical mechanisms, as is done at the milli-scale [128, 195], requires on-board high-voltage power sources. Thus, miniaturization of such technology to the microscale could be challenging.

3.2.10 Electrowetting Propulsion

Electrowetting is a technique for manipulating fluid interfaces using an electric field. The surface energy of the electrolytic fluid is modified using an electrode embedded in the substrate, which can result in motion of the fluid interface [114]. Such effects have long been observed, and have been used extensively in microfluidics [29, 81]. Recently this effect has been demonstrated in a form like a mobile microrobot. In [176], a "fluidic microrobot" is formed from a water droplet trapped between two electrode layers and moved by electrowetting. By applying high voltages to embedded patterned electrodes in the supporting

substrate, the hydrophobicity of one edge of the bubble can be changed, which results in horizontal forces on the bubble. This microrobot can thus be pulled in 2D, depending on the configuration of the embedded electrodes. While high speeds of up to 250 μm/s have been achieved with this system, the liquid nature of the microrobot renders it difficult to use as a contact manipulator, and it is restricted to operation in an air environment. However, the system does naturally lend itself to parallel operation with multiple bubble microrobots working in tandem.

3.2.11 Biohybrid Actuation

A relatively new propulsion methodology uses the power of microorganisms such as bacteria and algae for true on-board actuation [13, 187]. The biomotors of these organisms use nutrients available in the environment such as glucose, and do not necessarily require top–down control signals to move and navigate. Such a biohybrid approach is naturally a small-scale methodology, existing typically at the several-microns size scale [40, 42, 113, 197, 219]. The two major challenges in this field are harnessing the bacteria to do useful work and controlling the motion of these actuators.

The bacterium *Serratia marcescens* (*S. marcescens*) is a multiflagellated species that is a highly agile and efficient swimmer in viscous low Reynolds number environments [56]. Moreover, the sensors within the bacterium can allow for steering via chemotaxis or phototaxis [197]. The use of *S. marcescens* for microscale manipulation and actuation has been well documented in a variety of applications. For example, *S. marcescens* was used to accomplish active mixing by adsorbing swarmer cells onto polydimethylsiloxane (PDMS) surfaces, and also for the propulsion of microscale objects by attaching them to the microobject surface [40]. With an ultraviolet light source, *S. marcescens* has been also able to accomplish active mixing in microfluidic channels, as well as the propulsion of PDMS microbarges by the same bacteria via phototaxis [113, 197]. Behkam and Sitti have explored the behavior of bacteria-propelled objects of various geometries in a static fluid, in addition to investigating a chemical switching method to establish on/off control of the bacteria-propelled objects

[14, 15]. Moreover, to reduce effects of bacteria attached on opposite sides of each microobject pushing against each other counterproductively, they proposed chemical and physical patterning techniques to allow for controlled bacteria adhesion in order to achieve higher speeds and more directional motion trajectories [15, 16]. The motion of these systems can be studied through stochastic analysis of the individual contributions from individual bacteria [7]. Recently, bacteria-attached microbeads have been shown to exhibit clear directional behavior in the presence of linear chemical gradients [110]. Chemical gradients could be used to steer bacteria-propelled objects through complex channels or environments toward a chemical source. This self-guided navigation is appealing in applications where feedback-controlled top–down navigation is not feasible, such as in remote areas of the human body.

A second method to "steer" such biohybrid systems uses magnetic fields to exert a magnetic torque on the bacteria itself. This can be done using magnetotactic bacteria, which include natural [135] or artificially embedded [99] magnetic particles. These magnetic bacteria respond to low-strength magnetic fields, and can be controlled in a robotic system for path-following or collective motion behaviors. The advantage of such a magnetic control system is that the magnetic fields can penetrate most environments to control the bacteria inside enclosed spaces such as inside the human body.

Some limitations of such a biohybrid approach could include limited actuation duration due to limited organism lifetime, high organism sensitivity to environmental conditions, potential pathogenic effects of these cells for medical applications, and difficulties in coordinating the motion of many stochastic bioactuators. However, bacteria-propelled microrobotic systems could have unique potential for self-directed swarm navigation at very small scales.

3.3 Buoyancy

For microrobots moving in 3D, the ability to levitate is complicated by the need for microrobot weight compensation. Thus, it could be desirable to achieve neutral buoyancy in a microrobot. In Kratochvil

et al. [115], magnetically actuated untethered CoNi microrobots are studied for complex motion in 3D liquid environments. For weight compensation, vertical forces must always be applied in addition to control forces, negatively influencing motion control. In the vertical orientation of the applied magnetic field, a 300 μm microrobot of buoyant weight 0.95 μN in water experiences a maximum upward magnetic driving force of 2.2 μN. Therefore, the weight of the microrobot is around 25% of the maximum force the magnetic system can deliver in that direction. The absence of weight compensation could allow the application of more equal forces in every direction and hence better movement. Neutral buoyancy in magnetic microrobots is especially difficult because magnetic materials are dense. The approximate density of relevant materials are listed in Table 3.4. Palagi and Pensabene [152] uses a low-density gel to lighten a near-spherical soft microrobot. Ikuta et al. [227] create 3D magnetic microstructures featuring low density hollow glass microcapsules for buoyancy. These are mixed with photocurable polymer and formed using a laser into intricate 3D shapes such as helices. In medicine, blood, cerebrospinal fluid, and the urinary tract are all regions of high focus, given the potential benefits of microrobot technology. Each of these fluid environments has density values close to water (1,000 kg/m^3), and so this is often chosen as a microrobot target density. A similar fabrication method by Jena et al. [104] takes advantage of large trapped air cavities for buoyancy. This design is fabricated

Table 3.4. Densities of common materials in microrobotics studies.

Material	Density ρ (kg/m^3)
Water	1,000
Silicone oil	960
Human blood	1,043–1,057 [88]
Human urine	1,000–1,030
Human vitreous humor	1,005–1,009 [22]
Human cerebral spinal fluid	1,003–1,005 [64]
Air	1.14
NdFeB	7,610
Iron	7,870
Nickel	8,900
Polyurethane	1140 (TC-892, BJB Enterprises)

by photolithography to include a large cavity, which is capped manually using polymer caps. This design has the advantage that it can be tuned to the correct density, and consists of only magnetic material and binding polymer.

3.4 Microrobot Localization

Determining the location of untethered microrobots in a space is a major challenge, depending on the operational environment. Nearly all current microrobot control techniques rely on vision-based localization using conventional machine vision-automated tracking algorithms. Vision requires line-of-sight access to the microrobot workspace, and may require more than one viewpoint to achieve 3D localization. For confined spaces such as inside the human body, however, alternative localization techniques must be developed. As will be seen below, techniques to localize microrobots down to hundreds of microns in size pose significant challenges, although some concepts have been proven for tracking objects as small as tens of microns. Limits in microrobot localization capability could motivate the use of microrobot swarms, which could be easier to track in aggregate form.

3.4.1 Optical Tracking

Optical tracking is possible for environments which offer line-of-sight access to the workspace. Using one or more cameras fitted to microscope optics, the position of a microrobot can be obtained. Standard machine vision techniques such as thresholding, background subtraction, edge detection, particle filters, and color-space techniques [18] can be used to process an image in real-time, providing position and potentially orientation information to the user or a feedback controller. More details are given in Section 3.1.3.

3.4.2 Magnetic Tracking

3.4.2.1 Electromagnetic tracking

Electromagnetic tracking is possible using a paired magnetic field generator and sensor. As the magnitude and direction of the generated

field is position dependent, a field reading can be used to determine the position of the sensor relative to the field emitter. Such devices are available commercially in a tethered form (Aurora from ND, Flock from Ascension), with operating workspaces up to tens of cm in size. As they depend on a precisely known magnetic field over the workspace, such devices are sensitive to the presence of magnetic materials in the proximity [69]. For increased sensitivity, these systems place the field sensor in the workspace, as the sensor can be made much smaller than the field emitter. An inverse setup could be possible, where the sensors are outside the workspace and the field generator is being tracked [178], but will suffer from very small tracking range for a small field generator. Due to these challenges of low signal strength and magnetic distortions, there have been no examples of such wireless magnetic tracking at the scale relevant to untethered microscale robots. Enabling such a solution could require a significant advance in microscale remote field sensors on-board the microrobot or increased signal-to-noise ratio detection of the microrobot field.

3.4.2.2 Tracking by MRI

The clinical MRI machine is naturally suited to track the 3D position of microrobots [77]. If integrated with motion capabilities, the MRI machine could perform time-multiplexed localization and motion procedures for nearly simultaneous feedback control [137, 17, 37, 131]. The MRI image created also has the advantage of visualizing the structure of the entire workspace. For applications involving soft tissue such as inside the human body, this could be critical information for navigation and diagnosis. As MRI machines use magnetic fields for imaging, strong ferromagnetic microrobots can distort the local image, causing artifacts which impede localization [37].

The MRI signature of microscale components containing magnetic and nonmagnetic components has been studied. Using a $\sim$150 μm cubic microcontainer, it was shown that the geometry and magnetic properties of the container greatly can change the resulting image [77]. However, through careful shielding, localization accuracies several times smaller than the object size could be obtained. Indeed, it has been

shown that magnetic microrobotic elements much smaller than the imaging resolution of the MRI machine can be localized by analyzing susceptibility artifacts, tracking steel microspheres as small as 15 μm in diameter [149].

Thus, the MRI machine represents a useful tool for microrobot actuation and tracking studies as well as a potential infrastructure for future microrobot healthcare applications. However, the high cost of MRI machine operation could limit their appeal.

3.4.3 X-ray Tracking

X-ray imaging has been used for medical imaging for many years, and in particular adept at imaging objects with a unique density compared with their surroundings. X-ray imaging works by transmitting high-frequency electromagnetic waves through the workspace. An image is generated by sensing the attenuated signal after it passes through the workspace. In this way, it could be ideal for imaging microrobots moving in areas of soft tissue inside the human body.

Images in 3D can be generated from a series of X-rays taken in different planes using computed tomography (CT) scanning. Such 3D X-ray images typically have resolutions of 1–2 mm, while static X-rays have improved resolution of less than 1 mm [218]. Modern techniques could improve the resolution to several hundred microns [148]. Fluoroscopy uses an X-ray source to achieve continuous imaging with resolutions as high as several hundred microns using advanced detectors [39]. Thus, the use of X-rays for the localization of microrobots could be feasible and useful in certain applications.

A major downside in using X-ray imaging is the amount of ionizing radiation a patient is exposed to during imaging. This could limit its use in healthcare or other biological applications.

3.4.4 Ultrasound Tracking

Ultrasound imaging is a low-risk alternative to X-rays for medical applications. It excels at localization in soft tissue, and can provide frame rates over 100 fps or even higher for custom setups [41]. Ultrasound imaging works by transmitting a sound wave of several MHz and

detecting the echoes to form an image. Ultrasound systems are commonly used and low-cost, and can easily provide accuracies better than 1 mm [220]. In general, higher frequency operation yields better spatial resolution but less tissue penetration ability. One major challenge when using ultrasound is that it does not work well in the presence of bone or gas, and a skilled operator is required to operate and interpret the ultrasound images.

Passive ultrasound tracking has not been used in the localization of microrobots, but a mm-scale device which is remotely excited to emit ultrasound waves has been shown to result in high-resolution localization in a proof-of-concept demonstration [146]. This ultrasound emitter was excited remotely using high-frequency magnetic fields at approximately 4 kHz, and simulations suggest that an imaging resolution of 0.5 mm could be achieved if the frequency is increased to 30 kHz, and the sensor placed 10 cm from the emitter.

3.5 Multi-Robot Control

One significant challenge in microrobotics is the control of multiple untethered agents. Some microrobotic systems are naturally well suited for addressable multi-robot control, including those driven by focused light [95, 96, 201]. However, some of the commonly used actuation schemes including control by magnetic or electric field operate remotely using a single global control signal. Thus, multi-robot control is difficult with these systems because driving signals are typically uniform in the workspace, so all agents receive identical control inputs. Without on-board circuitry and actuators to decode selective control signal, mechanical selection methods must be developed for the full control of multiple microrobots. Here we review some of the approaches used to address microrobots which operate using a single global control input.

Researchers have shown the coupled control of multiple microrobots through the use of specialized addressing surfaces or through differing dynamic responses of heterogeneous microrobot designs, all in 2D on a flat operating surface. While some of these methods show promise for the distributed operation of many microrobots as a team, the limitation to operation on a 2D surface is significant as further developments in

microrobots, especially for medical applications, will require 3D motion in liquid volumes.

Multi-robot operation on a 2D planar surface has been achieved in three ways: localized selective trapping, through the use of heterogeneous microrobot designs, and through selective magnetic disabling methods. Operatoin in 3D has been demonstrated through heterogeneous microrobot designs. Here we introduce these addressing methods and discuss their utility for potential distributed microrobot tasks using teams of independently controlled microrobots.

3.5.1 Addressing through Localized Trapping

In localized trapping, a spatially varying actuation is applied to only retard the motion of a single agent. This has taken the form of localized electrostatic [156] or magnetic [48] trapping, and is capable of completely independent (noncoupled) control of multiple agents, at the cost of required embedded electrodes or magnets at a distance comparable with the spatial resolution of the addressing.

Motion of multiple magnetic microrobots has been achieved by employing a surface divided into a grid of cells, where each cell on the surface contains an addressable electrostatic trap capable of anchoring individual microrobots to the surface by capacitive coupling; this prevents them from being actuated by the external magnetic fields 3.8. This approach is related to that found in the field of *distributed manipulation* [23], where parts are manipulated in parallel using programmable force fields, but here the distributed cells provide only a retarding force while the actuation magnetic force is globally applied to all modules. For multiple microrobot control, the substrate upon which the robot moves has an array of independently controlled interdigitated electrodes to provide selective electrostatic anchoring. For experiments, a surface with four independent electrostatic pads was fabricated.

The electrostatic clamping force provided by these electrodes was given by Equation (3.17). In short, the force is proportional to the square of the applied voltage and inverse square of the electrode-microrobot gap. In [156], such trapping forces are used with patterned electrodes to selectively trap magnetic microrobots which move using

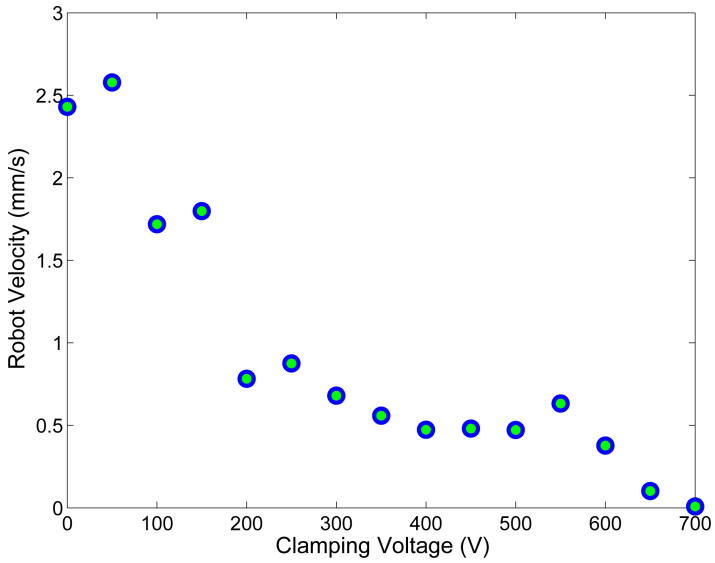

Fig. 3.8 Robot velocity versus electrostatic anchoring voltage for a microrobot on a 6-μm thick SU-8 layer, as studied in [156]. A critical voltage of 700 V is required to affix the microrobot. Videos of the motion were recorded and analyzed to determine velocities. A pulsing frequency of 20 Hz was used for translation.

the stick-slip crawling method from Section 3.2.1. As the dynamics of the this crawling motion involve complex surface interactions, it is difficult to predict the reduction in crawling speed in the presence of electrostatic trapping forces. In Figure 3.8, an experimental plot of microrobot velocity versus electrostatic anchoring voltage is shown, where it is seen that the required voltage is about 700 V to stop robot motion. Robot velocity does not monotonically decrease as voltage is increased, but experiences a local maximum near 550 V. For the purpose of multi-robot control, however, the critical voltage for effective anchoring is of importance.

This selective electrostatic trapping surface is useful as a potentially scalable method for multi-robot control in 2D. Some limitations include the requirement for high-strength electric fields, which may not be compatible with the manipulation of biological samples, and the limitation that all microrobots which are not trapped move in parallel with the direction of applied magnetic field.

3.5.2 Addressing through Heterogeneous Robot Designs

In addressing through heterogeneous robot designs, the agents are designed to respond differently to the same input signals. To achieve independent responses, where robot motions are not linearly related to one another, some type of dynamic response is required. In Donald et al. [52], different critical turning voltages are used to independently steer up to four electrostatically actuated microrobots, already introduced in Section 3.2.6. A similar approach uses microrobots with unique turning rates for differentiation [153]. Using appropriate control algorithms, independent positioning can be achieved with this method, albeit with limited control over the path taken. Turning arms are fabricated using stress-engineered MEMS techniques, to snap into contact at different critical voltages, which depend on the stiffness and geometry of the arm and its height above the electrode substrate. Unique voltages are created by changing these parameters, specifically the height and size of the arm. Microrobot actuation is accomplished through low-voltage "stepping cycle", while arm state changes are accomplished periodically with a short applied V_{arm}, which ranges from 140 to 190 V. The snap-into-contact also exhibits hysteresis characteristics, which allows for more than two arms to be independently controlled by nesting the "snap-down" and "snap-up" voltages appropriately for each design. The actuation "stepping" voltage then must lie between the "snap-down" and "snap-up" voltages to allow for motion without altering the turning state of the microrobots.

In Diller et al. [43, 65], a dynamic stick-slip crawling motion is used to achieve independent but coupled velocity responses, as shown in Figure 3.9. This allowed for arbitrary positioning of up to three microrobots to goal positions in 2D, following a desired path within a span of a few body-lengths. Vartholomeos et al. [213] use a similar method which relies on the nonlinear drag of millimeter-scale capsules with different sizes. This method could not be scaled down to the micron-scale due to the reliance on inertial drag forces which are negligible at smaller scales.

In Frutiger et al. [71], multiple resonant magnetic crawling microrobots are designed with different resonant frequencies, allowing

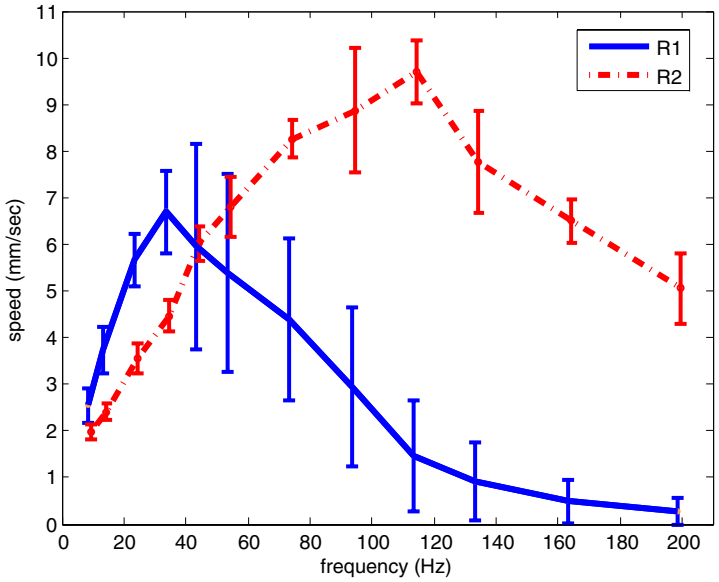

Fig. 3.9 Experimental velocity responses of twoMag-μBots with varying aspect ratios but similar values of effective magnetization, from [43, 65]. The maximum field strength was held at 1.1 mT. Data points are mean values and error bars represent standard deviations for ten trials.

for independent motion demonstrated on a specialized electrostatic surface. The frequency response of these resonant microrobots has relatively sharp peaks. Such independent addressing has been shown for two Mag-Mite microrobots using an associated electrostatic surface to aid microrobot motion.

When moving in 3D, available actuation techniques are reduced to swimming and direct pulling because there is no solid surface to push against as is used in the crawling 2D methods. To control multiple microrobot independently, the selective trapping method cannot be used because it relies on a nearby functionalized surface to provide trapping forces. Thus, the use of independent responses of heterogeneous microrobot designs is the only viable method for independent control in 3D. This has been accomplished for small groups of magnetic microrobots which are pulled using magnetic field gradients [44]. Here, selection is accomplished by designing each microrobot to respond uniquely to rotating magnetic fields through different magnetic and fluid drag

properties. This allowed for a unique magnetic force to be exerted on each microrobot, enabling independent path following in 3D using vision feedback control. This remains the only experimentally demonstrated multi-robot control technique for 3D motion.

However, as another potentially viable method for microrobotic control in 3D, Zhang et al. [237] have shown the differing velocity response of unique artificial flagella with differing drag torque or magnetic properties, but has not achieved independent positioning of multiple microrobots, presumably due to the inherent difficulties in controlling such swimming microrobots. Tottori et al. [207] have used an oscillating magnetic field to independently drive two artificial flagella swimming microrobots with different soft magnetic head designs. This also has not been used to achieve independent positioning of multiple microrobots.

3.5.3 Addressing through Selective Magnetic Disabling

One method uses multiple magnetic materials with varying magnetic hysteresis characteristics in tandem to achieve addressable control. The magnetization of so-called "permanent" magnet materials in fact can be reversed by applying a large field against the magnetization direction and the field required to perform this switch (i.e., the magnetic coercivity, H_c) is different for each magnetic material. For permanent magnetic materials, the coercivity field is much larger than the fields at which the microrobots are actuated for motion, allowing for motion actuation and magnetic switching to be performed independently. By using multiple materials with different magnetic coercivities, the magnetic reversal of each can also be performed independently by applying magnetic fields of the correct strength.

This independent magnetic switching can be used in microrobotic actuators to achieve addressable control of microrobotic elements. Our first addressable actuation scheme consists of several heterogeneous (each made from a different magnetic material) micromagnet modules interacting locally via magnetic forces. Selectively reversing the magnetization of one module can change the system from an attractive to a repulsive state. We present an experiment of this form, containing a set of heterogeneous magnetic modules floating on a liquid surface which

can be remotely reconfigured by application of a field of varying magnitude. In such a way, the morphology of the assembly can be altered arbitrarily into a number of states using a single applied field of varying strengths. This implementation could be used for shape-changing microrobots which adapt to the task at hand.

To achieve many-state magnetic control of a number of microrobotic actuators, we require a number of magnetic materials with different hysteresis characteristics [45, 46, 144]. The magnetic coercivity and remanence (retained magnetization value when the applied field H is reduced to zero) for a few commonly used materials are compared in Table 3.1, with coercivity values for ground powders measured in an alternating gradient force magnetometer (AGFM). In addition, the experimentally measured hysteresis loops for ground NdFeB, ferrite, alnico, and iron are shown in Figure 3.10. These materials cover a wide range of hysteresis values, from NdFeB and $SmCo_5$, which are permanent under all but the largest applied fields, to iron, which exhibits almost no hysteresis. For comparison, the magnetic fields applied to actuate magnetic microactuators are smaller than 12 kA/m, which is only strong enough to remagnetize the iron. Thus, the magnetic states of SmCo, NdFeB, ferrite, and alnico can be preserved when driving an actuator. This

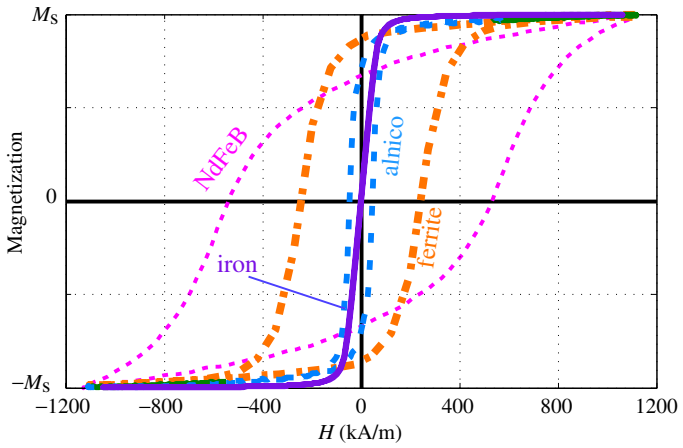

Fig. 3.10 H-m hysteresis loops of microrobot magnetic materials, taken in an AGFM for applied field up to 1,110 kA/m shows distinct material coercivity values. The magnetization is normalized by the saturation magnetization M_s of each sample.

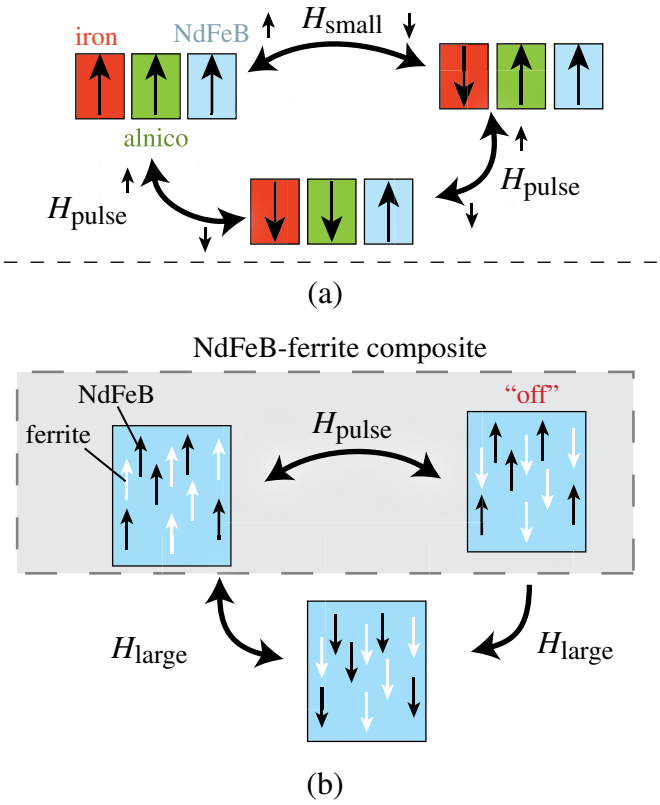

Fig. 3.11 Schematic showing the multiple magnetic states which can be achieved through the use of a variety of magnetic materials [45]. (a) Three separate magnetic actuators, each made from a different magnetic material, the magnetization of which can be independently addressed by applying magnetic field pulses of various strengths. Here, H_{pulse} is a large field pulse and H_{small} is a small static field. (b) A single magnetic composite actuator can be switched between the "up", "off", or "down" states by applying pulses of different strengths. Here H_{large} is a very large field pulse.

can be used to independently control the magnetization of each material, even when they share the same workspace. By applying a series of pulses in the desired direction greater than the coercivity field (H_c) of a particular material, an independent magnetization state of each magnet material can be achieved, as shown schematically in Figure 3.11(a) for a set of three independent micromagnetic elements. Here, a set of three magnetic actuators made from iron, NdFeB, and alnico are shown, and

the magnetization direction of each actuator can be selectively switched by applying small or large magnetic fields.

As a second actuation scheme, a pair of magnetic materials can work together in one actuator, forming a magnetic composite whose magnetic moment sum interacts with externally applied or locally induced fields. Experimentally, we introduce a microscale permanent magnet composite material that can be remotely and reversibly turned off and on by the application of a magnetic field pulsed along the magnetic axis which reverses the magnetization of one of the materials. For completely remote operation, this pulsed field is supplied by electromagnetic coils outside the device workspace. This scheme is similar to *electropermanent magnets*, in which electromagnetic coils are wrapped directly around some of an array of switchable permanent magnets. When a strong current is pulsed through the coils, the magnetization of some of the permanent magnets is flipped, allowing for an off–on net magnetization of the set. Electropermanent magnets were originally used as centimeter-scale or larger magnetic work holders as an alternative to a mechanical vice [24]. While millimeter-scale *electropermanent magnets* have been fabricated [76], they contain integrated switching coils, preventing their scaling down to the micrometer scale for untethered operation.

The magnetic composite material proposed in this monograph can be scaled down to the micron-scale and enables remote wireless control. The anisotropic composite is made from two materials of equal magnetic moment: one permanent magnet material of high coercivity and one material which switches magnetization direction by applied fields. By switching the second material's magnetization direction, the two magnets either work together or cancel each other, resulting in distinct on and off behavior of the device. The device can be switched on or off remotely using a field pulse of short duration. Because the switching field pulse covers the entire workspace, this method could be used to selectively disable and enable many microdevices concurrently based on their orientations. Orientation control is achieved by a multistep process using a field gradient to select a device for disabling by controlling each device's orientation.

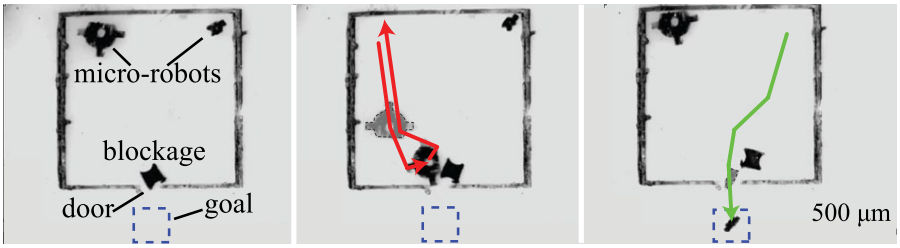

Fig. 3.12 Addressable microrobot teamwork task, requiring the cooperative contribution of two mobile microrobots of different sizes working together to reach a goal, as performed in [45]. Frames show two superimposed frames, with the microrobot paths traced and midpoints outlined. (a) Both microrobots lie inside an enclosed area. The door to the goal is blocked by a plastic blockage. Only the larger microrobot can move the blockage, while only the smaller microrobot is small enough to fit through the door. (b) The larger microrobot is enabled, and moved to remove the blockage while the smaller disabled microrobot remains in place. The larger microrobot is returned to its staring point and disabled. (c) The smaller microrobot is enabled and is free to move through the door to the goal.

To demonstrate the usefulness of a team of microrobots, a simple cooperative teamwork task is shown in Figure 3.12, where two microrobots of different sizes attempt to reach a goal location. Here, the two microrobots begin trapped in an enclosed area. The arena walls are made from polyurethane molded in a replica molding process similar to that used to fabricate the molded microrobots. The door to the goal is covered by a plastic blockage. As the large microrobot is too big to fit through the door and the small microrobot is too small to move the blockage, both must work together as a team to reach the goal.

4

Potential Applications

As it advances, microrobot technology has begun to be used in practical applications. Here, we overview a few of the potential applications for remotely actuated microrobots. Some progress has been made in initial studies for these application areas, but much work needs to be done before the technology truly proves itself in an application area.

4.1 Microobject Manipulation

Manipulation could be used at the microscale to assemble parts or deliver payloads to goal locations. Such manipulation at the microscale requires precise actuation and control over adhesion forces to release manipulated parts [142]. This has traditionally made microscale manipulation very challenging using microgrippers controlled by large robotic arms. Microrobots could offer advantages over these systems by providing remote manipulation inside enclosed spaces and could solve adhesion problems through liquid-based manipulation.

Methods for manipulating micron-scale objects can be classified into two categories: contact and noncontact manipulation. The distinction between the two is based upon the presence or absence of

physical contact when manipulating microobjects. In general, contact manipulation is preferred for the study of microobjects that will not be damaged by any resulting contact forces. Contact manipulation can also supply larger pushing forces, and increased speed. Noncontact methods are employed when manipulation forces must be comparatively low, if very fine precision is required, or if the microobject is too fragile to be grasped by physical contact.

4.1.1 Contact-Based Pushing Manipulation

Manipulation by direct contact can be accomplished down to the micron-scale by using "traditional" manipulation techniques using grippers fabricated using MEMS techniques. Such grippers are typically tethered, but one example [57] has made an untethered MEMS thermal gripper actuated by a focused laser. This design has been integrated into a levitating mm-scale microrobot which has three translational degrees of freedom over a small working space in an air environment. The manipulator is able to grasp and move objects from $100\,\mu$m to 1 mm in size for simple assembly tasks. However, as with all microgrippers operating in an air environment, the release of parts is a critical problem.

Remotely actuated manipulators must provide the precision and strength of traditional manipulators to be effective. While progress has been made, this is the major challenge in this application area.

In [157], mm-scale magnetically levitated robots which are moved by integrated electrical coil traces under the operating surface are used to assemble simple cm-scale structures from a "bin" of parts. Solid parts are picked up using passive arms, and liquids, such as glue, are placed using a simple dipping arm. High speed and excellent potential for large-scale distributed manipulation are achieved with this system, with submicron precision when returning to a patterned trace location.

At the sub-mm scale, object manipulation becomes more difficult as controlled motion is difficult, and adhesive forces begin to overwhelm actuation forces. Therefore, all manipulation by sub-mm untethered

microrobots has been conducted in a liquid environment to provide fluid damping and greatly reduced adhesive forces.

Simple magnetic microrobots are used to directly push microbeads [67] and cells [173] of sizes down to several microns. With controllable locomotion as slow as several microns per second, very precise manipulation is possible by direct pushing using a relatively simple magnetic actuation. No specialized grippers are required for this manipulation.

The use of helical microswimmers offers 3D motion capability in liquid environments. In [208], microhelices are fabricated using 3D direct laser writing and vapor deposition and consist of a helical tail and a cage-like head to trap microparticles. Driving the helix toward a 6-μm colloidal particle resting on the substrate surface results in the particle being trapped in the cage, such that the helix can carry the particle in 3D to a goal. The particle is released by driving the helix in the reverse direction.

Preliminary demonstrations of manipulation using biohybrid microrobots has been shown [135] [cite others too], but more work must be done to steer such cargo for transport and delivery.

4.1.2 Noncontact Fluidic Manipulation

It is also possible to manipulate objects in a low-Re fluid environment by using noncontact fluidic manipulation. In Floyd et al. [67], a microrobot of several hundred microns in size is used to manipulate microobjects in a precise manner using fluid-based forces. The microrobot operates in a water environment, and translates past a microobject to exert forces. The motion of microobjects in the induced flow is a balance between the fluid drag force and the friction and adhesion which acts to hold the particle still. The fluid boundary layer around the translating microrobot was studied in detail, with regions of influence defined for 1% of the maximum flow velocity. Using a 250 μm magnetic microrobot, 50 and 230 μm polystyrene spheres were manipulated without contact in this method. We now give a more detailed case study of this noncontact manipulation analysis for a single case of microrobot translation.

Fig. 4.1 (a) A teleoperated star-shaped microrobot and a 210-μm microsphere for side-pushing under liquid on a glass surface, from [154]. (b) The microrobot moves past the microsphere from its side, causing the sphere to displace a small amount D_s, primarily due to the fluid interactions. Arrow on microrobot indicates the direction of its motion.

4.1.2.1 Case study: Noncontact manipulation using magnetic microrobot

Here we report on a single case of noncontact manipulation using a translating magnetic microrobot near a microobject, from [154]. The case we consider is when the magnetic microrobot translates by the object, as shown in Figure 4.1.

For this analysis we ignore any contact manipulation forces, and focus solely on the fluidic and surface adhesive forces. The surface forces between the microobject and the surface are taken from Section 2.1.2.1. Due to the choice of materials (polystyrene microspheres on glass in a water environment), the surface adhesion is negative, implying that its effects can be neglected. Viscous fluid drag is analyzed as shown in Section 2.1.2.3. As these objects are operating in a low-Re regime, the inertial effects of the microspheres can be neglected.

The fluid motion induced by the translating microrobot is attained by finite element modeling (FEM) using COMSOL Multiphysics (COMSOL Inc.). The low-Re (Stokes flow) physics is used, and the fluid velocity is found in the workspace. The microrobot is here modeled as stationary at an angle of $\pi/8$ radians with respect to the surface (an approximate average angle of the microrobot during its stick-slip locomotion), and a bounding box defines the finite element simulation volume. The front and rear bounding faces are treated as a flow inlet and outlet, respectively, with a flow of 0.4 mm/s.

The fluid velocity due to the translating microrobot is shown in Figure 4.2, and the simulated particle motion found using a Runge–Kutta solver (ODE23s in MATLAB, Mathworks, Inc.).

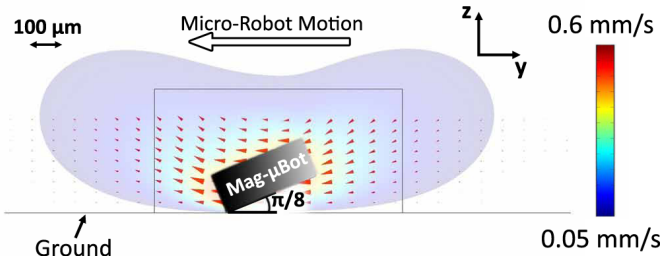

Fig. 4.2 A side-view slice of the finite element modeling (FEM) solution for the flow around a star-shaped microrobot as it traverses through the environment, from [154]. The microrobot is moving toward the left in these images, and the flow velocities correspond to y-directed flow, depicted by arrows. Half the microrobot is modeled in this analysis.

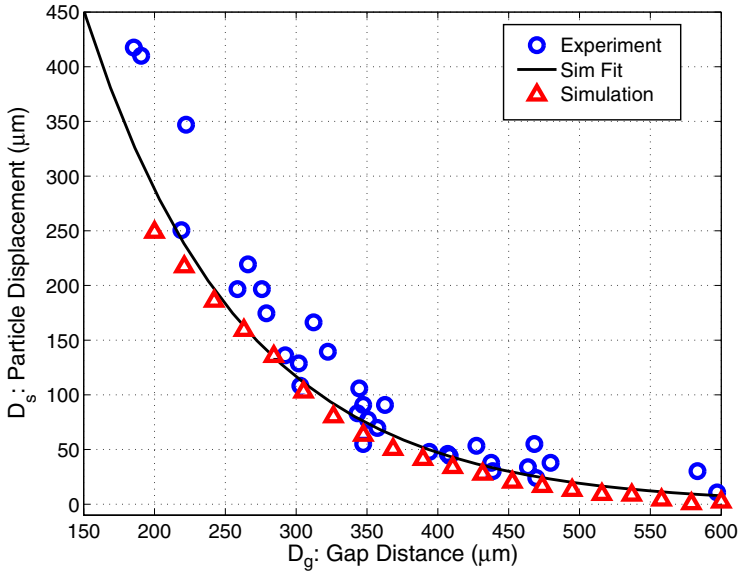

Fig. 4.3 Simulation and experiment of a star-shaped microrobot manipulating a 210-μm microsphere from the side, from [154]. Vertical division indicates whether sphere contact occurs with the microrobot's edge, determined from the simulation. The simulation fit "Sim Fit" is from the dynamic simulation, while "Sim Fit Lin" is a linear approximation to this fit, which can be used for control using these results.

This case study has shown the key physical parameters which dictate the motion of microparticles in a robot-induced fluid flow. The fluid flow from a moving microrobot can be used to manipulate particles within microrobot body-lengths away at very slow speeds. This can be used for very precise object positioning. As we have seen, to analyze

this problem a full model of the microrobot motion, fluid flow from finite-element solutions and microobject adhesion and friction model are required.

4.1.2.2 Rotational noncontact manipulation

As a related method in [48, 228], a constantly spinning micromanipulator was used to induce a rotational fluid flow which moves microobjects in the region. Using a 380-μm microrobot, 200-μm particles are able to be moved at speeds up to 3.5 mm/s in a rotation motion. In addition, by using teams of these microrobots arranged in a reconfigurable grid pattern in 2D, complex "virtual channels" can be created which allow the microrobots to pass the object along for long distance fast transport, as shown in Figure 4.4. By tilting the microrobot rotation axis slightly from the vertical, rolling is achieved, which allows for precise microrobot positioning during manipulation. It is observed that a certain size of particle will become trapped near the microrobot for certain rotation speeds, and so the microrobot can carry the particle over long distances using this method. By combining these long distance and slower precision rotational flow manipulation methods, a coarse–fine object placement is demonstrated.

At a smaller scale, this was also executed using a rotating nanowire or self-assembled collection of microbeads [158, 238]. Using a weak

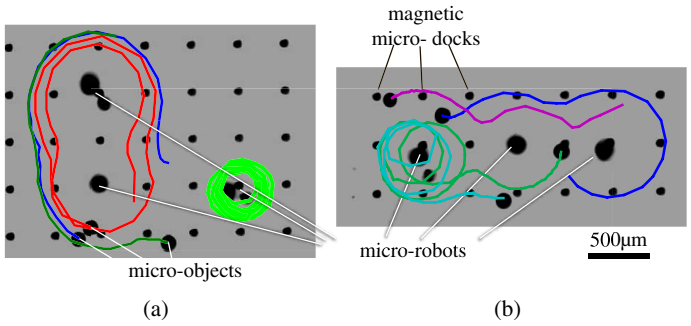

Fig. 4.4 Team noncontact manipulation by three microrobots simultaneously spinning, as was shown in [48]. The microrobot positions are trapped at discrete locations by magnetic docks embedded in the surface. Microsphere paths are tracked by colored lines. Reprinted with permission from [48]. Copyright 2012, AIP Publishing LLC.

rotating magnetic field, this approach was used to move microspheres and cells using a 13-μm nickel nanowire. Thus, such noncontact manipulation methods have shown their effectiveness across several size scales.

Artificial bacterial flagella can also be used for noncontact object manipulation. The rotational motion of these microrobots naturally creates a rotational fluid flow, which can be used to move objects [239]. The coordinated manipulation of many microobjects has been shown in this way for example to clear an area of particles, although it is not clear if this can be used for precision manipulation of particles to goal positions as the fluid flow is necessarily coupled to the microhelix translation.

4.1.3 Autonomous Manipulation

One difficulty with precision manipulation using noncontact methods is that any motion of the microrobot in the region moves the target objects. As such, even removing the microrobot after manipulation becomes a problem. Using principles of manipulation from [67], an autonomous particle manipulation controller has been developed which uses physical models and a learning controller to precisely manipulate particles using nonconstant fluid forces [154]. Even in the presence of unknown disturbance forces, the model-based feedforward input of this controller allows for precise manipulation and removal of the microrobot afterward. In addition, this work presented the assembly of two particles together, a task which is generally difficult using nonconstant manipulation.

4.1.4 Bio-object Manipulation

The manipulation of bio-objects by untethered microrobots has much promise for lab-on-a-chip applications, individual cell study, and tissue scaffolds. A major requirement for such manipulation is gentle pushing so as not to damage the object, as well as biocompatibility. In [95], a bubble microrobot is shown to manipulate a number of hydrogels functionalized with yeast cells. The gels are arranged into a tight heterogeneous 2D grid by the microrobots, and after time the yeast

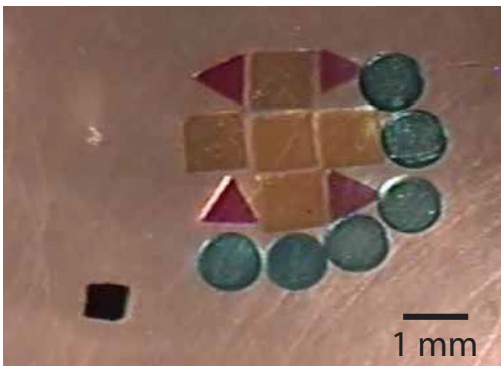

Fig. 4.5 Microgel blocks are arranged using a magnetically driven microrobot on a planar surface.

cells are cultured on the scaffold. Such a demonstration has potential use for complex cell culture experiments or for *in-vitro* growth of tissues or even organs. A similar microgel assembly experiment using a magnetically-driven microrobot is shown in Figure 4.5.

4.1.5 Team Manipulation

Manipulation of microobjects by teams of microrobots could have major advantages in speed and capability. In Floyd et al. [66], multiple magnetic microrobots are moved independently using an electrostatic trapping surface. As every untrapped microrobot moves in parallel, this approach requires careful planning to increase manipulation speed over a single-robot case.

Using teams of microrobots trapped at "docking" sites in the substrate, rotating magnetic microrobot teams have been used to perform noncontact manipulation of objects in a liquid environment [48]. As the location of the spinning microrobots is variable, the microrobots in this case form "virtual channels" which move objects in a versatile manner appropriate for use in microfluidic channels.

As a method which naturally allows for multi-robot control, optically controlled bubble microrobots have been used to perform team manipulation of objects [95]. In this work, two microrobots are used to sandwich microobjects for precise and fast manipulation.

These team demonstrations are promising for distributed and parallel manipulation, but must prove their advantage over the much simpler single-robot manipulation case for it to be adopted.

4.1.6 Microfactories

Microrobots working in 2D or 3D could be used to assemble microparts in ways difficult using conventional fabrication. Of particular interest is the assembly of 3D parts which require orientation and position control. Microrobots could apply adhesives, position parts, and repair defects in a desktop setup. As such a process would likely be a serial assembly process, it could benefit greatly from parallel microrobot assembly teams. While microobject manipulation thus far has not approached the sophistication required for such a microfactory, the potential is great, and the concept has been proven at a slightly larger size scale. Pelrine et al. [157] have shown such a process with mm-scale magnetic robots levitating on a diamagnetic surface. Each robot in this study was equipped with a tool such as gripper, adhesive applicator, or weighing pan for distributed operation.

4.2 Healthcare

Remote microrobots have great promise for medical applications. Some of the potential application areas for medical microrobots operating inside the human body are thoroughly outlined in [147], and are listed below. The reader is referred to this article for further discussion and review of the opportunities and challenges for microrobots in healthcare.

- Drug delivery/brachytherapy
- Marking target therapy areas
- Sensing of chemical concentrations
- Electrode implantation
- Occlusion/stent construction
- Tissue scaffold creation
- Biopsy sampling
- Thermal or mechanical ablation
- Hyperthermia treatment

Some of the targeted areas of the body could include the circulatory system, central nervous system, urinary tract, the eye, and the auditory canal.

As first steps toward these application areas, a magnetically controlled needle has been shown to operate inside artificial and *ex-vivo* eyes [115]. As a healthcare application area, the inside of the eye is a natural first step as the volume of the eye is visible through a microscope. This preliminary therapy has aimed to puncture the vasculature. Navigation in the eye is, however, complicated by the complex optics of the eye. An algorithm to compensate for this optical distortion has been presented [19] which obtains the 3D position of an intraocular microrobot, assuming that the microrobot geometry is known. Drug delivery in the eye has been investigated with a diffusion-based drug coated on a microrobot surface [49] for potential treatment of retinal vein occlusion.

Progress in the other potential medical application areas will come with refinement of microrobot motion strategies in 3D liquid environments and development of relevant integrated microtools.

4.3 Reconfigurable Microrobotics

The field of reconfigurable robotics proposes versatile robots that can reform into various configurations depending on the task at hand [232]. These types of robotic systems consist of many independent and often identical modules, each capable of motion, and capable of combining with other modules to create assemblies. These modules can then be disassembled and reassembled into alternate configurations. For example, Shen et al. [183] demonstrate SuperBot; this robot consists of 20 modules that can combine to form a mobile mechanism that can roll across the ground for 1 km and then reconfigure into one that can climb obstacles.

Another concept in the field of reconfigurable robotics is *programmable matter*, which is matter that can assemble and reconfigure into arbitrary 3D shapes, giving rise to *synthetic reality* [80]. This is similar to virtual or augmented reality, where a computer can generate and modify an arbitrary object. However, in *synthetic reality*, this

object has physical realization. A primary goal for *programmable matter* is scaling down the size of each individual module, with the aim of increasing spatial resolution of the final assembled product. Currently, the smallest deterministic, actuated module in a reconfigurable robotic system fits inside a 2-cm cube [234], which is a self-contained module that is actuated using shape memory alloy. Scaling down further into the submillimeter scale brings new issues, including module fabrication, control, and communication.

For the purposes of micron-scale assembly using microrobots, Donald et al. [52] demonstrate the assembly of four MEMS-fabricated silicon microrobots, each under 300 μm in all dimensions, actuated by electric fields. Once assembled, however, they cannot detach and reconfigure, because the electrostatic driving fields do not allow for disassembly. Lipson et al. have demonstrated reconfigurable assemblies using 500 μm planar silicon elements [206] and cm-scale 3D elements [108]. By controlling the local fluid flow in these systems, the elements can be deterministically assembled and disassembled into target shapes. This system relies on an active substrate to provide fluid flow and control and so the assembled micron-scale elements have limited mobility.

In [47], sub-millimeter scale untethered permanent magnet microrobots (Mag-μBots) are actuated by external magnetic fields as components of magnetic micromodules (Mag-μMods), for creating deterministic reconfigurable 2D microassemblies; this implies that the Mag-μMods will be able to both assemble and disassemble. Strong permanent magnet modules will attract each other with large magnetic forces; therefore it is necessary to reduce this magnet force between modules to facilitate disassembly. This can be done by adding an outer shell to the Mag-μBot for the design of a module. The outer shell prevents two magnetic modules from coming into close contact, where magnetic forces will become restrictively high. However, they are still sufficiently close together to yield a mechanically stable assembly.

Motion of multiple Mag-μMods is achieved by employing a surface divided into a grid of cells, where each cell on the surface contains an addressable electrostatic trap capable of anchoring individual Mag-μMods to the surface by capacitive coupling; this prevents them from

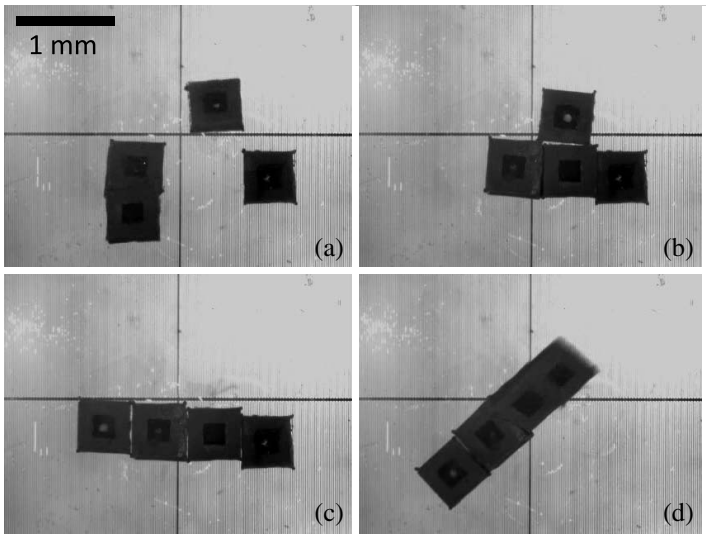

Fig. 4.6 Frames from a movie with four teleoperated Mag-μMods assembling into a reconfigurable structure, from [47]. Arrows indicate direction of magnetization. (a) Four Mag-μMods prepare for assembly. (b) All four modules are assembled in a T-configuration. (c) One module is broken free by rotation and reattaches in a new configuration. (d) The new assembly is mobile, and is shown moving to a new location.

being actuated by the external magnetic fields. This approach is related to that found in the field of *distributed manipulation* [23], where parts are manipulated in parallel using programmable force fields, but here the distributed cells provide only a retarding force while the actuation magnetic force is globally applied to all modules. Unanchored Mag-μMods can move on the surface due to the imposed magnetic fields, and move in parallel. This technique is identical to controlling multiple Mag-μBots, explained in detail in [156]. Assembling two Mag-μMods is straightforward – by moving an unanchored Mag-μMod toward an anchored one, magnetic forces eventually dominate and cause the two Mag-μMods to self-assemble.

For disassembly of two Mag-μMods to occur, the magnetic attraction between them must be overcome and the two separated. To do this, the electrostatic grid surface is used to anchor parts of assembled modules, and examine the effectiveness of externally applied magnetic torques to disassemble unanchored modules from the assembly.

Figure 4.6 shows the concept of multiple Mag-μMods assembling, disassembling, and reconfiguring into a different configuration. Because the Mag-μMods are magnetic, they can only assemble into configurations that are magnetically stable, implying that they form single closed flux loops.

4.4 Scientific Tools

Untethered microrobots are capable of exerting forces on objects potentially inaccessible by other methods. Such action can be used to probe living organisms or microscale structures as a diagnostic investigation of material properties and mechanical response. While sophisticated investigations have begun with tethered microrobotic setups [61, 171], the use of untethered microrobots has potential to perform these studies in natural environments. The direct manipulation of cells can also be important for study in microfluidic channels. It has been demonstrated that a magnetic microrobot can push live cells without damaging the cells [173] for localized observation and probing.

The physical probing of individual cells to investigate mechanobiological response has been studied [109]. In this work, a magnetic microtool (MMT) is integrated with an on-board force sensor based on visual detection of beam deflection. The MMT has a sharp tip and is used in a preliminary work to mechanically stimulate a 100-μm diatom cell while the response is observed.

These preliminary studies have shown that microrobots can form tools for study of phenomena at the microscale. It is expected that similar applications in materials research, biotechnology, microfluidics, and other areas will be possible with appropriately designed microrobots with the ability to move object, apply precise forces, measure chemical concentrations, and other abilities.

Remote sensing using a mobile microrobot could be used as a tool to investigate and map chemical concentrations, temperature, etc. in enclosed spaces with high resolution. Optical-based oxygen sensors have been integrated with mobile microrobots capable of 3D motion for interrogation inside the human eye [58]. Additional modalities such as resonant-based sensors read by reflected light [25] or magnetic fields [103] could increase the versatility of these remote measurements.

5

Conclusions and Open Challenges

5.1 Status Summary

The field of microrobotics has proven itself as an exciting potential solution to problems in confined microscale spaces. Research thus far has focused on extending robotics principles of precise top–down control to the sub-mm size scale for motion and interaction with the environment. Many novel solutions have been designed to operate effectively in the presence of microscale physics, in particular with high surface adhesion and viscous fluid flow. Current demonstrations in microrobotics have primarily focused on methods of moving in 2D or 3D. Solutions in 2D have included crawling on surfaces in air or liquid environments using a wide variety of actuation methods. The diversity of the approaches is promising, as each method contains particular advantages and disadvantages which could align with potential application areas. The demonstrated methods are capable of precisely moving microrobots using traditional robotics techniques such as path-planning and obstacle avoidance, and have been shown in remote inaccessible spaces such as inside microfluidic channels. In 3D, motion has been accomplished by swimming or pulling by chemical reactions or magnetic forces. Some

of these methods have been biologically inspired, using novel swimming mechanisms from microorganisms to move in viscous low-Re fluid environments. These methods have allowed for feedback-control path-following in 3D, and have been proven to work in difficult environments such as in the presence of fluid flow.

Feedback of microrobot position has thus far primarily taken the form of vision through a microscope. This has provided precise localization in 2D using a single camera or in 3D using multiple cameras or advanced vision algorithms, which is naturally suited for machine vision feedback control. While alternate localization by ultrasound, X-ray and MRI have been investigated, these techniques are still in the proof-of-concept stage for microrobotics.

Some progress has been made toward microrobot applications in object manipulation, healthcare, and as tools for scientific study. Thus far, these have only been proof-of-concept demonstrations, but such research has been increasing recently as more microrobot capabilities increase.

5.2 What Next?

Despite such progress, many open challenges remain in the field of microrobotics. Some of these have been identified in this review, and some are inevitably yet to be known at all due to the fast-changing nature of the field. The desired microrobot capabilities are primarily driven by the potential applications. Some of the areas where concrete advances are required are listed below:

- **Motion**. Significant progress must be made in microrobot motion in 2D and 3D. In particular, precision, speed, and high force capabilities must be improved to allow microrobots to be useful tools for microscale applications. Current methods are promising, but must be moved out of the concept stage and be developed into "technologies" which can be applied to solve other problems.
- **Multi-robot control**. While a few methods for multi-robot control have been demonstrated, these methods suffer from poor scalability to large numbers of microrobots. For parallel

distributed operation to show its full potential, very large numbers of microrobots must operate in tandem in 2D or 3D. Whether this takes the form of greater numbers of individually addressed microrobots, or swarm-like interactions between agents resulting in emergent team behaviors, this challenging research area could have a large impact on the usefulness of microrobots over existing technologies.

- **Localization**. Optical microscope-based localization is adequate for a few microrobotics applications such as in microfactories or microfluidics, but is not compatible with many applications, most notably used inside the human body. Thus, alternate methods must be developed which provide precision, high feedback rates, and compatibility with medical procedures.
- **Object manipulation**. Manipulation procedures must be improved to allow for precise part transport and assembly. Methods for moving objects in 3D and over long distances must be designed to open up the design space for microassembly applications. Applications for micromanipulation by microrobots must target areas where existing microassembly by photolithography or other methods is inadequate. These could include creating complex 3D assemblies, or in providing a versatile and flexible assembly paradigm.
- **Tools**. Integrated tools must be designed to exploit the full potential of mobile microrobots. Methods for heating, gripper, cutting, or others which are wirelessly actuated along with the microrobot could transform microrobots from interesting novelties to truly useful devices for interacting with the environment.
- **Sensing**. The ability to create mobile sensors which can access remote spaces is a great potential achievement for microrobotics. Such mobile microsensors could probe microfluidic channels or the inside of the human body in a location-specific manner not possible by any other method. The sensing method must work remotely, with or without visual line-of-sight.

- **Biocompatibility**. For any biotechnology or medical applications, microrobots must be compatible. High-strength electric fields, toxic magnetic materials, or high temperatures are all potential problem areas for biocompatibility. This problem will be solved by a judicious choice of actuation method along with biocompatible coatings for toxic microrobot materials.
- **Automation and learning**. As the complexity of microrobotic systems increases, more sophisticated control algorithms, including autonomous control must be further developed. Most demonstrated microrobot tasks thus far have been controlled via teleoperation or simple path following algorithms. In addition, to accommodate changing experimental conditions and fabrication errors, adaptive learning control algorithms will be required for robust operation.

Logical approaches to some of these action areas have been identified, while the best approach to other areas is still an open question.

5.3 Conclusions

This monograph has provided a review and tutorial of the field of microscale robotics. It has presented progress in light of the relevant physical challenges present at the microscale, and we hope that it will help to guide those designing future microrobot technologies. While the review was not completely comprehensive in every area, it was intended to expose the reader to the novel approaches used thus far for microrobot motion, manipulation, and other tasks. The rapid pace of development in the field is exciting, and we look forward to the next solutions to the problems discussed here.

Nomenclature

α	Coefficient of thermal expansion
χ	Magnetic susceptibility
ϵ	Relative dielectric constant
ϵ_0	Permittivity of free space
ϵ_t	Thermal strain
γ	Intrinsic surface energy
γ_l	Liquid surface tension
κ_d	Ellipsoid shape factor
λ	Elasticity parameter
λ_w	Electromagnetic signal wavelength
μ	Fluid viscosity
μ_0	Permeability of free space
μ_f	Friction coefficient
ν	Poisson's ratio
ω	Rotation rate
ω_o	Oscillation frequency
ρ	Density
ρ_1	Number of atoms in an interacting body
τ	Fluid drag transient time

θ	Liquid–solid contact angle
$\vec{B}$	Magnetic flux density
$\vec{F}_m$	Magnetic force
$\vec{H}$	Magnetic field
$\vec{M}$	Volume magnetization
$\vec{m}$	Magnetic moment
$\vec{r}$	Vector to a point of interest
$\vec{T}_m$	Magnetic torque
ξ	Viscous drag coefficient
ζ_e	Electrical damping ratio
ζ_m	Mechanical damping ratio
A	Hamaker constant
a	Ellipsoid major axis
A_f	Contact area
A_o	Oscillation amplitude
b	Ellipsoid minor axis
b_r	Root-mean square roughness of a surface
C	Coefficient in a particle–particle pair interaction
D	Helix major diameter
d_w	Immersion depth of a sphere
E	Young's modulus
$E(k)$	Elliptic integral of the second kind
f	Friction force
F_d	Drag force on a sphere
F_e	Electrostatic force
F_w	Drag force on a sphere near a wall
F_{id}	Electrostatic anchoring force
F_{KR}	Kahn–Richardson fluid drag force
F_{vdW}	Van der Waals force
g	Acceleration due to gravity
g	Gap between a microrobot and a substrate
h	Separation distance between two surfaces
h_c	Height of a liquid in a tube due to surface tension forces
I	Current through a coil
K	Equivalent elastic modulus of contact
$K(k)$	Elliptic integral of the first kind

L	Characteristic length
L_a	Coil inductance
L_c	Object characteristic length in a fluid flow
N	Normal force
n	Number of helix turns
N_t	Number of turns in a magnetic coil
p	Pressure
P_D	Pull-off force, Dugdale model
P_e	Electrical power available to a resonant energy scavenging system
P_f	Fluid pressure
P_i	Interface pressure
P_r	RF power transfer
R	Sphere radius
R_a	Coil resistance
R_e	Effective radius of contact
R_g	Gas constant
r_k	Fluid meniscus radius
r_s	Interatomic spacing
r_t	Tube radius
R_{tr}	Distance between transmitter and receiver
S	Surface area
T	Temperature
T_d	Drag torque on a sphere
T_w	Fluid drag torque on a sphere near a wall
U	Fluid velocity
u	Fluid velocity
u_∞	Fluid characteristic velocity
V	Volume
v	Velocity
V_c	Voltage across a coil
W	Work of adhesion
w	Interaction potential
blps	Body lengths per second

References

[1] "Criteria for significant risk investigations of magnetic resonance diagnostic devices," Technical Report, U.S. Food and Drug Administration, 2003.

[2] "Solid surface energy data (SFE) for common polymers," http://www.surface-tension.de/solid-surface-energy.htm, 2012.

[3] J. J. Abbott, O. Ergeneman, M. P. Kummer, A. M. Hirt, and B. J. Nelson, "Modeling magnetic torque and force for controlled manipulation of soft-magnetic bodies," *2007 IEEE/ASME International Conference on Advanced Intelligent Mechatronics*, vol. 23, no. 6, pp. 1–6, September 2007.

[4] J. J. Abbott, Z. Nagy, F. Beyeler, and B. Nelson, "Robotics in the small, part I: Microbotics," *Robotics & Automation Magazine*, vol. 14, no. 2, pp. 92–103, June 2007.

[5] J. J. Abbott, K. E. Peyer, M. C. Lagomarsino, L. Zhang, L. Dong, I. K. Kaliakatsos, and B. J. Nelson, "How Should Microrobots Swim?," *The International journal of Robotics Research*, vol. 28, no. 11–12, p. 1434, July 2009.

[6] A. Adamson, *Physical Chemistry of Surfaces*. Wiley-Interscience, 6th ed., 1997.

[7] V. Arabagi, B. Behkam, E. Cheung, and M. Sitti, "Modeling of stochastic motion of bacteria propelled spherical microbeads," *Journal of Applied Physics*, vol. 109, no. 11, p. 114702, 2011.

[8] V. Arabagi, L. Hines, and M. Sitti, "Design and manufacturing of a controllable miniature flapping wing robotic platform," *The International Journal of Robotics Research*, vol. 31, no. 6, pp. 785–800, February 2012.

[9] F. Arai, D. Ando, T. Fukuda, Y. Nonoda, and T. Oota, "Micro manipulation based on micro physics — strategy based on attractive force reduction and stress measurement," in *IEEE/RSJ International Conference on Intelligent Robots and Systems*, vol. 2, pp. 236–241, Pittsburgh, PA, 1995.

[10] L. Arcese, M. Fruchard, F. Beyeler, A. Ferreira, and B. J. Nelson, "Adaptive backstepping and MEMS force sensor for an MRI-guided microrobot in the vasculature," in *International Conference on Robotics and Automation*, pp. 4121–4126, 2011.

[11] M. Aus, C. Cheung, and B. Szpunar, "Saturation magnetization of porosity-free nanocrystalline cobalt," *Journal of materials science letters*, vol. 7, pp. 1949–1952, 1998.

[12] S. P. Beeby, M. J. Tudor, and N. M. White, "Energy harvesting vibration sources for microsystems applications," *Measurement Science and Technology*, vol. 17, no. 12, pp. R175–R195, December 2006.

[13] B. Behkam and M. Sitti, "Design methodology for biomimetic propulsion of miniature swimming robots," *Journal of Dynamic Systems, Measurement, and Control*, vol. 128, no. 1, p. 36, 2006.

[14] B. Behkam and M. Sitti, "Bacterial flagella-based propulsion and on/off motion control of microscale objects," *Applied Physics Letters*, vol. 90, p. 023902, 2007.

[15] B. Behkam and M. Sitti, "Effect of quantity and configuration of attached bacteria on bacterial propulsion of microbeads," *Applied Physics Letters*, vol. 93, no. 22, p. 223901, December 2008.

[16] B. Behkam and M. Sitti, "Characterization of bacterial actuation of micro-objects," in *International Conference on Robotics and Automation*, pp. 1022–1027, May 2009.

[17] K. Belharet, D. Folio, and A. Ferreira, "Endovascular navigation of a ferromagnetic microrobot using MRI-based predictive control," in *2010 IEEE/RSJ International Conference on Intelligent Robots and Systems*, pp. 2804–2809, October 2010.

[18] C. Bergeles, G. Fagogenis, J. Abbott, and B. Nelson, "Tracking intraocular microdevices based on colorspace evaluation and statistical color/shape information," in *International Conference on Robotics and Automation*, pp. 3934–3939, 2009.

[19] C. Bergeles, B. E. Kratochvil, and B. J. Nelson, "Visually servoing magnetic intraocular microdevices," *IEEE Transactions on Robotics*, vol. 28, no. 4, pp. 798–809, 2012.

[20] P. Bernhard and P. Renaud, "Microstereolithography: Concepts and applications," in *International Conference on Emerging Technologies and Factory Automation*, pp. 289–298, 2001.

[21] R. Bjork, C. R. H. Bahl, A. Smith, and N. Pryds, "Comparison of adjustable permanent magnetic field sources," *Journal of Magnetism and Magnetic Materials*, vol. 322, no. 22, pp. 3664–3671, November 2010.

[22] J. Black, *Handbook of Biomaterial Properties*. Springer, 1998.

[23] K.-F. Böhringer, B. R. Donald, and N. C. MacDonald, "Programmable force fields for distributed manipulation, with applications to MEMS actuator arrays and vibratory parts feeders," *The International Journal of Robotics Research*, vol. 18, no. 2, pp. 168–200, February 1999.

[24] P. Braillon Magnetic plate comprising permanent magnets and electropermanent magnets, 1978.

[25] T. Braun, V. Barwich, M. Ghatkesar, A. Bredekamp, C. Gerber, M. Hegner, and H. Lang, "Micromechanical mass sensors for biomolecular detection in a physiological environment," *Physical Review E*, vol. 72, no. 3, pp. 1–9, 2005.

[26] W. C. Brown, "The history of power transmission by radio waves," *IEEE Transactions on Microwave Theory and Techniques*, vol. 32, no. 9, pp. 1230–1242, 1984.

[27] A. Buzas, L. Kelemen, A. Mathesz, L. Oroszi, G. Vizsnyiczai, T. Vicsek, and P. Ormos, "Light sailboats: Laser driven autonomous microrobots," *Applied Physics Letters*, vol. 101, no. 4, p. 041111, 2012.

[28] N. Chaillet and S. Régnier, "First experiments on MagPieR: a planar wireless magnetic and piezoelectric microrobot," in *IEEE International Conference on Robotics and Automation*, pp. 102–108, 2011.

[29] H.-C. Chang and L. Yeo, *Electrokinetically-Driven Microfluidics and Nanofluidics*. Cambridge University Press, 2009.

[30] D. K. Cheng, *Field and Wave Electromagnetics*. Addison-Wesley Publishing Company, Inc., 2nd ed., 1992.

[31] J.-W. Choi, E. MacDonald, and R. Wicker, "Multi-material microstereolithography," *The International Journal of Advanced Manufacturing Technology*, vol. 49, no. 5–8, pp. 543–551, December 2009.

[32] R. Clift, J. Grace, and M. E. Weber, *Bubbles, Drops, and Particles*. Academic Press, 2005.

[33] K. A. Cook-Chennault, N. Thambi, and A. M. Sastry, "Powering MEMS portable devices — a review of non-regenerative and regenerative power supply systems with special emphasis on piezoelectric energy harvesting systems," *Smart Materials and Structures*, vol. 17, no. 4, p. 043001, August 2008.

[34] O. Cugat, J. Delamare, and G. Reyne, "Magnetic micro-actuators and systems (MAGMAS)," *IEEE Transactions on Magnetics*, vol. 39, no. 6, pp. 3607–3612, November 2003.

[35] B. Cullity and C. Graham, *Introduction to Magnetic Materials*. Wiley-IEEE Press, 2008.

[36] T. Czerwiec, N. Renevier, and H. Michel, "Low-temperature plasma-assisted nitriding," *Surface and Coatings Technology*, vol. 131, pp. 267–277, 2000.

[37] C. Dahmen, D. Folio, T. Wortmann, A. Kluge, A. Ferreira, and S. Fatikow, "Evaluation of a MRI based propulsion/control system aiming at targeted micro/nano-capsule therapeutics," in *International Conference on Intelligent Robots and Systems*, pp. 2565–2570, 2012.

[38] H. Danan, A. Herr, and A. Meyer, "New determinations of the saturation magnetization of nickel and iron," *Journal of Applied Physics*, vol. 39, no. 2, p. 669, 1968.

[39] J. H. Daniel, A. Sawant, M. Teepe, C. Shih, R. A. Street, and L. E. Antonuk, "Fabrication of high aspect-ratio polymer microstructures for large-area electronic portal x-ray imagers," *Sensors and Actuators. A, Physical*, vol. 140, no. 2, pp. 185–193, November 2007.

[40] N. Darnton, L. Turner, K. Breuer, and H. C. Berg, "Moving fluid with bacterial carpets," *Biophysical journal*, vol. 86, no. 3, pp. 1863–70, March 2004.

[41] T. Deffieux, J.-L. Gennisson, M. Tanter, and M. Fink, "Assessment of the mechanical properties of the musculoskeletal system using 2-D and 3-D very high frame rate ultrasound," *IEEE Transactions on Ultrasonics, Ferroelectrics, and Frequency Control*, vol. 55, no. 10, pp. 2177–2190, October 2008.

[42] R. Di Leonardo, L. Angelani, D. Dell'arciprete, G. Ruocco, V. Iebba, S. Schippa, M. P. Conte, F. Mecarini, F. De Angelis, and E. Di Fabrizio, "Bacterial ratchet motors," *Proceedings of the National Academy of Sciences of the United States of America*, vol. 107, no. 21, pp. 9541–5, May 2010.

[43] E. Diller, S. Floyd, C. Pawashe, and M. Sitti, "Control of multiple heterogeneous magnetic microrobots in two dimensions on nonspecialized surfaces," *IEEE Transactions on Robotics*, vol. 28, no. 1, pp. 172–182, 2012.

[44] E. Diller, J. Giltinan, and M. Sitti, "Independent control of multiple magnetic microrobots in three dimensions," *The International Journal of Robotics Research*, vol. 32, no. 5, pp. 614–631, May 2013.

[45] E. Diller, S. Miyashita, and M. Sitti, "Magnetic hysteresis for multi-state addressable magnetic microrobotic control," in *International Conference on Intelligent Robots and Systems*, pp. 2325–2331, 2012.

[46] E. Diller, S. Miyashita, and M. Sitti, "Remotely Addressable Magnetic Composite Micropumps," *RSC Advances*, vol. 2, no. 9, pp. 3850–3856, February 2012.

[47] E. Diller, C. Pawashe, S. Floyd, and M. Sitti, "Assembly and disassembly of magnetic mobile micro-robots towards deterministic 2-D reconfigurable microsystems," *The International Journal of Robotics Research*, vol. 30, no. 14, pp. 1667–1680, September 2011.

[48] E. Diller, Z. Ye, and M. Sitti, "Rotating magnetic micro-robots for versatile non-contact fluidic manipulation of micro-objects," in *IEEE International Conference on Robots and Systems*, pp. 1291–1296, 2011.

[49] G. Dogangil and O. Ergeneman, "Toward targeted retinal drug delivery with wireless magnetic microrobots," in *International Conference on Intelligent Robots and Systems*, pp. 1921–1926, 2008.

[50] B. R. Donald and C. G. Levey, "An untethered, electrostatic, globally controllable MEMS micro-robot," *Journal of Microelectromechanical Systems*, vol. 15, no. 1, pp. 1–15, 2006.

[51] B. R. Donald, C. G. Levey, C. D. McGray, D. Rus, and M. Sinclair, "Power delivery and locomotion of untethered microactuators," *Journal of Microelectromechanical Systems*, vol. 12, no. 6, pp. 947–959, 2003.

[52] B. R. Donald, C. G. Levey, and I. Paprotny, "Planar microassembly by parallel actuation of MEMS microrobots," *Journal of Microelectromechanical Systems*, vol. 17, no. 4, pp. 789–808, 2008.

[53] R. Dreyfus, J. Baudry, M. L. Roper, M. Fermigier, H. A. Stone, and J. Bibette, "Microscopic artificial swimmers," *Nature*, vol. 437, no. 7060, pp. 862–865, October 2005.

[54] S. Earnshaw, "On the nature of the molecular forces which regulate the constitution of the luminiferous ether," *Transactions of the Cambridge Philosophical Society*, vol. 7, pp. 97–112, July 1842.

[55] J. Edd, S. Payen, B. Rubinsky, M. Stoller, and M. Sitti, "Biomimetic propulsion for a swimming surgical micro-robot," in *International Conference on Intelligent Robots and Systems*, pp. 2583–2588, 2003.

[56] M. R. Edwards, R. W. Carlsen, and M. Sitti, "Near and far-wall effects on the three-dimensional motion of bacteria-driven microbeads," *Applied Physics Letters*, vol. 102, p. 143701, 2013.

[57] C. Elbuken, M. Khamesee, and M. Yavuz, "Design and implementation of a micromanipulation system using a magnetically levitated MEMS robot," *IEEE/ASME Transactions on Mechatronics*, vol. 14, no. 4, pp. 434–445, August 2009.

[58] O. Ergeneman and G. Chatzipirpiridis, "In vitro oxygen sensing using intraocular microrobots," *IEEE Transactions on Biomedical Engineering*, vol. 59, no. 11, pp. 3104–3109, September 2012.

[59] H. Faxen, "Die Bewegung einer starren Kugel längs der Achse eines mit zäher Flüssigkeit gefüllten Rohres," *Arkiv foer Matematik, Astronomi och Fysik*, vol. 17, no. 27, pp. 1–28, 1923.

[60] R. Fearing, "Survey of Sticking Effects for Micro Parts Handling," in *IEEE/RSJ International Conference on Intelligent Robots and Systems*, pp. 212–217, Pittsburgh, PA, 1995.

[61] D. Felekis, S. Muntwyler, H. Vogler, F. Beyeler, U. Grossniklaus, and B. J. Nelson, "Quantifying growth mechanics of living, growing plant cells in situ using microrobotics," *Micro & Nano Letters*, vol. 6, no. 5, p. 311, 2011.

[62] D. J. Filipiak, A. Azam, T. G. Leong, and D. H. Gracias, "Hierarchical self-assembly of complex polyhedral microcontainers," *Journal of Micromechanics and Microengineering*, vol. 19, no. 7, pp. 1–6, July 2009.

[63] S. Filiz, L. Xie, L. E. Weiss, and O. Ozdoganlar, "Micromilling of microbarbs for medical implants," *International Journal of Machine Tools and Manufacture*, vol. 48, no. 3–4, pp. 459–472, March 2008.

[64] R. A. Fishman, *Cerebrospinal Fluid in Diseases of the Nervous System*. Saunders, 2nd ed., 1980.

[65] S. Floyd, E. Diller, C. Pawashe, and M. Sitti, "Control methodologies for a heterogeneous group of untethered magnetic micro-robots," *The International Journal of Robotics Research*, vol. 30, no. 13, pp. 1553–1565, March 2011.

[66] S. Floyd, C. Pawashe, and M. Sitti, "Microparticle manipulation using multiple untethered magnetic micro-robots on an electrostatic surface," in *IEEE/RSJ International Conference on Intelligent Robots and Systems, 2009. IROS 2009*, pp. 528–533, October 2009.

[67] S. Floyd, M. Sitti, and C. Pawashe, "Two-dimensional contact and non-contact micro-manipulation in liquid using an untethered mobile magnetic microrobot," *IEEE Transactions on Robotics*, vol. 25, no. 6, pp. 1332–1342, 2009.

[68] T. W. R. Fountain, P. V. Kailat, and J. J. Abbott, "Wireless control of magnetic helical microrobots using a rotating-permanent-magnet manipulator," in *IEEE International Conference on Robotics and Automation*, pp. 576–581, May 2010.

[69] D. D. Frantz and A. D. Wiles, "Accuracy assessment protocols for electromagnetic tracking systems," *Physics in Medicine and Biology*, vol. 48, no. 14, pp. 2241–2251, 2003.

[70] W. M. Frix, G. G. Karady, and B. A. Venetz, "Comparison of calibration systems for magnetic field measurement equipment," *IEEE Transactions on Power Delivery*, vol. 9, no. 1, pp. 100–108, 1994.

[71] D. R. Frutiger, K. Vollmers, B. E. Kratochvil, and B. J. Nelson, "Small, fast, and under control: Wireless resonant magnetic micro-agents," *The International Journal of Robotics Research*, vol. 29, no. 5, pp. 613–636, November 2009.

[72] B. Gady, D. Schleef, R. Reifenberger, D. Rimai, and L. DeMejo, "Identification of electrostatic and van der Waals interaction forces between a micrometer-size sphere and a flat substrate," *Physical Review. B, Condensed Matter*, vol. 53, no. 12, pp. 8065–8070, March 1996.

[73] M. Gauthier, S. Régnier, P. Rougeot, and N. Chaillet, "Analysis of forces for micromanipulations in dry and liquid media," *Journal of Micromechatronics*, vol. 3, no. 3–4, pp. 389–413, 2006.

[74] A. P. Gerratt, I. Penskiy, and S. Bergbreiter, "SOI/elastomer process for energy storage and rapid release," *Journal of Micromechanics and Microengineering*, vol. 20, no. 10, p. 104011, October 2010.

[75] A. Ghosh and P. Fischer, "Controlled propulsion of artificial magnetic nanostructured propellers," *Nano Letters*, vol. 9, no. 6, pp. 2243–5, June 2009.

[76] K. Gilpin, A. Knaian, and D. Rus, "Robot pebbles: One centimeter modules for programmable matter through self-disassembly," in *IEEE International Conference on Robotics and Automation*, pp. 2485–2492, 2010.

[77] B. Gimi, D. Artemov, T. Leong, D. H. Gracias, and Z. M. Bhujwalla, "MRI of regular-shaped cell-encapsulating polyhedral microcontainers," *Magnetic resonance in medicine*, vol. 58, no. 6, pp. 1283–1287, December 2007.

[78] R. B. Goldfarb and F. R. Fickett, *Units for Magnetic Properties*. US Department of Commerce, National Bureau of Standards, 1985.

[79] A. J. Goldman, R. G. Cox, and H. Brenner, "Slow viscous motion of a sphere parallel to a plane wall-I Motion through a quiescent fluid," *Chemical Engineering Science*, vol. 22, no. 4, pp. 637–651, 1967.

[80] S. C. Goldstein, J. D. Campbell, and T. C. Mowry, "Programmable Matter," *Computer*, vol. 38, no. 6, pp. 99–101, 2005.

[81] J. Gong, S.-K. Fan, and C.-J. Kim, "Portable digital microfluidics platform with active but disposable lab-on-chip," in *International Conference on Micro Electro Mechanical Systems*, vol. 3, pp. 355–358, 2004.

[82] J. J. Gorman, C. D. McGray, and R. A. Allen, "Mobile microrobot characterization through performance-based competitions," in *Proceedings of the 9th Workshop on Performance Metrics for Intelligent Systems*, pp. 122–126, New York, NY, USA: ACM Press, 2009.

[83] S. Guo and Y. Hasegaw, "Fish-like underwater microrobot with multi DOF," in *International Symposium on Micromechatronics and Human Science*, pp. 63–68, 2001.

[84] M. Hagiwara, T. Kawahara, T. Iijima, and F. Arai, "High-speed magnetic microrobot actuation in a microfluidic chip by a fine V-groove surface," *Transactions on Robotics*, vol. 29, no. 2, pp. 363–372, 2013.

[85] J. Happel and H. Brenner, *Low Reynolds Number Hydrodynamics*. Prentice-Hall, 1965.

[86] F. Heslot, A. Cazabat, P. Levinson, and N. Fraysse, "Experiments on wetting on the scale of nanometers: Influence of the surface energy," *Physical Review Letters*, vol. 65, no. 5, pp. 599–602, 1990.

[87] P. Hess, "Laser diagnostics of mechanical and elastic properties of silicon and carbon films," *Applied Surface Science*, vol. 106, pp. 429–437, 1996.

[88] H. Hinghofer-Szalkay and J. E. Greenleaf, "Continuous monitoring of blood volume changes in humans," *Journal of Applied Physiology*, vol. 63, no. 3, pp. 1003–1007, September 1987.

[89] N. M. Holbrook and M. A. Zwieniecki, "Transporting water to the tops of trees quick study," *Physics Today*, vol. 61, pp. 76–77, 2008.

[90] S. Hollar, A. Flynn, S. Bergbreiter, S. Member, and K. S. J. Pister, "Robot leg motion in a planarized-SOI, two-layer poly-Si process," *Journal of Microelectromechanical Systems*, vol. 14, no. 4, pp. 725–740, 2005.

[91] A. Holmes and G. Hong, "Axial-flow microturbine with electromagnetic generator: Design, CFD simulation and prototype demonstration," in *IEEE International Conference on Micro Electro Mechanical Systems*, pp. 568–571, 2004.

[92] T. Honda, K. I. Arai, and K. Ishiyama, "Micro swimming mechanisms propelled by external magnetic fields," *IEEE Transactions on Magnetics*, vol. 32, no. 5, pp. 5085–5087, 1996.

[93] S. B. Horowitz, M. Sheplak, L. N. Cattafesta, and T. Nishida, "A MEMS acoustic energy harvester," *Journal of Micromechanics and Microengineering*, vol. 16, no. 9, pp. S174–S181, 2006.

[94] D. L. Hu, B. Chan, and J. W. M. Bush, "The hydrodynamics of water strider locomotion," *Nature*, vol. 424, no. 6949, pp. 663–666, August 2003.

[95] W. Hu, K. S. Ishii, Q. Fan, and A. T. Ohta, "Hydrogel microrobots actuated by optically generated vapour bubbles," *Lab on a Chip*, vol. 12, no. 19, pp. 3821–6, August 2012.

[96] W. Hu, K. S. Ishii, and A. T. Ohta, "Micro-assembly using optically controlled bubble microrobots," *Applied Physics Letters*, vol. 99, no. 9, p. 094103, 2011.

[97] W. Hu, B. Yang, C. Peng, and S. W. Pang, "Three-dimensional SU-8 structures by reversal UV imprint," *Journal of Vacuum Science & Technology B: Microelectronics and Nanometer Structures*, vol. 24, no. 5, p. 2225, 2006.

[98] G. Hwang, R. Braive, L. Couraud, A. Cavanna, O. Abdelkarim, I. Robert-Philip, A. Beveratos, I. Sagnes, S. Haliyo, and S. Regnier, "Electro-osmotic propulsion of helical nanobelt swimmers," *The International Journal of Robotics Research*, vol. 30, no. 7, pp. 806–819, June 2011.

[99] D. Hyung Kim, P. Seung Soo Kim, A. Agung Julius, and M. Jun Kim, "Three-dimensional control of Tetrahymena pyriformis using artificial magnetotaxis," *Applied Physics Letters*, vol. 100, no. 5, p. 053702, 2012.

[100] K. Ishiyama, M. Sendoh, A. Yamazaki, and K. I. Arai, "Swimming micromachine driven by magnetic torque," *Sensors and Actuators A: Physical*, vol. 91, no. 1–2, pp. 141–144, June 2001.

[101] J. Israelachivili, *Intermolecular and Surface Forces*. Academic Press, 1992.

[102] E. W. Jager, E. Smela, and O. Inganäs, "Microfabricating conjugated polymer actuators," *Science*, vol. 290, no. 5496, pp. 1540–5, November 2000.

[103] M. K. Jain and C. A. Grimes, "A wireless magnetoelastic micro-sensor array for simultaneous measurement of temperature and pressure," *IEEE Transactions on Magnetics*, vol. 37, no. 4, pp. 2022–2024, July 2001.

[104] P. Jena, E. Diller, J. Giltinan, and M. Sitti, "Neutrally Buoyant Microrobots for Enhanced 3D Control," in *International Conference on Intelligent Robots and Systems, workshop on Magnetically Actuated Multiscale Medical Robots*, 2012.

[105] G.-L. Jiang, Y.-H. Guu, C.-N. Lu, P.-K. Li, H.-M. Shen, L.-S. Lee, J. A. Yeh, and M. T.-K. Hou, "Development of rolling magnetic microrobots," *Journal of Micromechanics and Microengineering*, vol. 20, no. 8, p. 085042, August 2010.

[106] W. Jing, X. Chen, S. Lyttle, and Z. Fu, "A magnetic thin film microrobot with two operating modes," in *International Conference on Robotics and Automation*, pp. 96–101, 2011.

[107] D. H. Kaelble and J. Moacanin, "A surface energy analysis of bioadhesion," *Polymer*, vol. 18, no. 5, pp. 475–482, May 1977.

[108] M. Kalontarov, M. T. Tolley, H. Lipson, and D. Erickson, "Hydrodynamically driven docking of blocks for 3D fluidic assembly," *Microfluidics and Nanofluidics*, vol. 9, no. 2–3, pp. 551–558, February 2010.

[109] T. Kawahara and M. Sugita, "On-chip manipulation and sensing of microorganisms by magnetically driven microtools with a force sensing structure," in *International conference on Robotics and Automation*, pp. 4112–4117, 2012.

[110] D. H. Kim, A. Liu, E. Diller, and M. Sitti, "Chemotactic steering of bacteria propelled microbeads," *Biomedical Microdevices*, vol. 14, no. 6, pp. 1009–1017, September 2012.

[111] D. H. Kim, E. B. Steager, U. K. Cheang, D. Byun, and M. J. Kim, "A comparison of vision-based tracking schemes for control of microbiorobots," *Journal of Micromechanics and Microengineering*, vol. 20, no. 6, p. 065006, June 2010.

[112] M. Kim, "Influence of substrates on the elastic reaction of films for the microindentation tests," *Thin Solid Films*, vol. 168, pp. 12–16, 1996.

[113] M. J. Kim and K. S. Breuer, "Use of bacterial carpets to enhance mixing in microfluidic systems," *Journal of Fluids Engineering*, vol. 129, no. 3, p. 319, 2007.

[114] D. Klarman, D. Andelman, and M. Urbakh, "A model of electrowetting, reversed electrowetting and contact angle saturation," *Langmuir*, vol. 27, no. 10, pp. 6031–6041, 2011.

[115] M. P. Kummer, J. J. Abbott, B. Kratochvil, R. Borer, A. Sengul, and B. J. Nelson, "OctoMag: An electromagnetic system for 5-DOF wireless micromanipulation," *IEEE Transactions on Robotics*, vol. 26, no. 6, pp. 1006–1017, 2010.

[116] A. Kurs, A. Karalis, R. Moffatt, J. D. Joannopoulos, P. Fisher, and M. Soljacic, "Wireless power transfer via strongly coupled magnetic resonances," *Science*, vol. 317, no. 5834, pp. 83–86, July 2007.

[117] J. Kymissis, C. Kendall, J. Paradiso, and N. Gershenfeld, "Parasitic power harvesting in shoes," in *IEEE International Conference on Wearable Computing*, pp. 132–139, 1998.

[118] M. C. Lagomarsino, F. Capuani, and C. P. Lowe, "A simulation study of the dynamics of a driven filament in an Aristotelian fluid," *Journal of Theoretical Biology*, vol. 224, no. 2, pp. 215–224, September 2003.

[119] A. Lai, R. Duggirala, and S. Tin, "Radioisotope powered electrostatic microactuators and electronics," in *International Conference on Solid-State Sensors, Actuators and Microsystems*, pp. 269–273, 2007.

[120] P. X. Lan, J. W. Lee, Y.-J. Seol, and D.-W. Cho, "Development of 3D PPF/DEF scaffolds using micro-stereolithography and surface modification," *Journal of materials science. Materials in medicine*, vol. 20, no. 1, pp. 271–9, January 2009.

[121] E. Lauga and T. R. Powers, "The hydrodynamics of swimming microorganisms," *Reports on Progress in Physics*, vol. 72, no. 9, p. 096601, September 2009.

[122] J. S. Lee, W. Yim, C. Bae, and K. J. Kim, "Wireless actuation and control of ionic polymer-metal composite actuator using a microwave link," *International Journal of Smart and Nano Materials*, vol. 3, no. 4, pp. 244–262, 2012.

[123] H. Li and A. Lal, "Self-reciprocating radioisotope-powered cantilever," *Journal of Applied Physics*, vol. 92, no. 2, pp. 1122–1127, 2002.

[124] J. Lighthill, "Flagellar hydrodynamics," *SIAM Review*, vol. 18, no. 2, pp. 161–230, 1976.

[125] Q. Liu and A. Prosperetti, "Wall effects on a rotating sphere," *Journal of Fluid Mechanics*, vol. 657, pp. 1–21, 2010.

[126] D. G. Lowe, "Object recognition from local scale-invariant features," in *Proceedings of the Seventh IEEE International Conference on Computer Vision*, vol. 2, pp. 1150–1157, 1999.

[127] D. G. Lowe, "Distinctive image features from scale-invariant keypoints," *International Journal of Computer Vision*, vol. 60, no. 2, pp. 91–110, November 2004.

[128] K. Y. Ma, P. Chirarattananon, S. B. Fuller, and R. J. Wood, "Controlled flight of a biologically inspired, insect-scale robot," *Science*, vol. 340, no. 6132, pp. 603–607, May 2013.

[129] A. W. Mahoney, D. L. Cowan, and K. M. Miller, "Control of untethered magnetically actuated tools using a rotating permanent magnet in any position," in *International conference on Robotics and Automation*, pp. 3375–3380, 2012.

[130] A. W. Mahoney, J. C. Sarrazin, E. Bamberg, and J. J. Abbott, "Velocity control with gravity compensation for magnetic helical microswimmers," *Advanced Robotics*, vol. 25, no. 8, pp. 1007–1028, May 2011.

[131] S. Martel, O. Felfoul, J.-B. Mathieu, A. Chanu, S. Tamaz, M. Mohammadi, M. Mankiewicz, and N. Tabatabaei, "MRI-based medical nanorobotic platform for the control of magnetic nanoparticles and flagellated bacteria for target interventions in human capillaries," *The International Journal of Robotics Research*, vol. 28, no. 9, pp. 1169–1182, September 2009.

[132] S. Martel, J. Mathieu, O. Felfoul, A. Chanu, E. Aboussouan, S. Tamaz, P. Pouponneau, G. Beaudoin, G. Soulez, and M. Mankiewicz, "Automatic navigation of an untethered device in the artery of a living animal using a conventional clinical magnetic resonance imaging system," *Applied Physics Letters*, vol. 90, p. 114105, 2007.

[133] S. Martel, J. J.-B. Mathieu, O. Felfoul, A. Chanu, E. Aboussouan, S. Tamaz, P. Pouponneau, G. Beaudoin, G. Soulez, M. Mankiewicz, and L. Yahia, "Automatic navigation of an untethered device in the artery of a living animal using a conventional clinical magnetic resonance imaging system," *Applied Physics Letters*, vol. 90, no. 11, p. 114105, 2007.

[134] S. Martel and M. Mohammadi, "Using a swarm of self-propelled natural microrobots in the form of flagellated bacteria to perform complex micro-assembly tasks," in *International Conference on Robotics and Automation*, pp. 500–505, 2010.

[135] S. Martel, C. Tremblay, S. Ngakeng, and G. Langlois, "Controlled manipulation and actuation of micro-objects with magnetotactic bacteria," *Applied Physics Letters*, vol. 89, p. 233904, 2006.

[136] M. Mastrangeli, S. Abbasi, C. Varel, C. Van Hoof, J.-P. Celis, and K. F. Böhringer, "Self-assembly from milli- to nanoscales: methods and applications," *Journal of Micromechanics and Microengineering*, vol. 19, no. 8, p. 083001, July 2009.

[137] J. B. Mathieu, G. Beaudoin, and S. Martel, "Method of propulsion of a ferromagnetic core in the cardiovascular system through magnetic gradients generated by an MRI system," *IEEE Transactions on Biomedical Engineering*, vol. 53, no. 2, pp. 292–299, 2006.

[138] J. B. Mathieu and S. Martel, "In vivo validation of a propulsion method for untethered medical microrobots using a clinical magnetic resonance imaging system," in *International Conference on Intelligent Robots and Systems*, pp. 502–508, 2007.

[139] D. Maugis, "Adhesion of spheres: The JKR-DMT transition using a Dugdale model," *Journal of Colloid and Interface Science*, vol. 150, no. 1, 1992.

[140] D. W. McRobbie, "Occupational exposure in MRI," *The British Journal of Radiology*, vol. 85, no. 1012, pp. 293–312, April 2012.

[141] D. C. Meeker, E. H. Maslen, R. C. Ritter, and F. M. Creighton, "Optimal realization of arbitrary forces in a magnetic stereotaxis system," *IEEE Transactions on Magnetics*, vol. 32, no. 2, pp. 320–328, November 1996.

[142] A. Menciassi, A. Eisinberg, I. Izzo, and P. Dario, "From macro to micro manipulation: Models and experiments," *IEEE/ASME Transactions on Mechatronics*, vol. 9, no. 2, pp. 311–320, June 2004.

[143] S. Meninger, J. O. Mur-Miranda, R. Amirtharajah, A. Chandrakasan, and J. Lang, "Vibration-to-electric energy conversion," in *International Symposium on Low Power Electronics and Design*, pp. 48–53, 1999.

[144] S. Miyashita, E. Diller, and M. Sitti, "Two-dimensional magnetic micromodule reconfigurations based on inter-modular interactions," *The International Journal of Robotics Research*, vol. 32, no. 5, pp. 591–613, May 2013.

[145] B. Munson, D. Young, and T. Okiishi, *Fundamentals of Fluid Mechanics*. John Wiley and Sons, Inc., 2002.

[146] Z. Nagy, M. Fluckiger, and O. Ergeneman, "A wireless acoustic emitter for passive localization in liquids," in *IEEE International Conference on Robotics and Automation*, pp. 2593–2598, Kobe, 2009.

[147] B. J. Nelson, I. K. Kaliakatsos, and J. J. Abbott, "Microrobots for minimally invasive medicine.," *Annual review of biomedical engineering*, vol. 12, pp. 55–85, August 2010.

[148] G. Neumann, P. DePablo, A. Finckh, L. B. Chibnik, F. Wolfe, and J. Duryea, "Patient repositioning reproducibility of joint space width measurements on hand radiographs," *Arthritis Care & Research*, vol. 63, no. 2, pp. 203–207, February 2011.

[149] N. Olamaei, F. Cheriet, G. Beaudoin, and S. Martel, "MRI visualization of a single 15 m navigable imaging agent and future microrobot," in *Annual International Conference of the IEEE Engineering in Medicine and Biology Society*, pp. 4355–8, January 2010.

[150] D. Olsen and J. Osteraas, "The critical surface tension of glass," *Journal of Physical Chemistry*, vol. 68, no. 9, pp. 2730–2732, 1964.

[151] C. D. Onal, O. Ozcan, and M. Sitti, "Automated 2-D nanoparticle manipulation using atomic force microscopy," *IEEE Transactions on Nanotechnology*, vol. 10, no. 3, pp. 472–481, 2011.

[152] S. Palagi and V. Pensabene, "Design and development of a soft magnetically-propelled swimming microrobot," in *International conference on Robotics and Automation*, pp. 5109–5114, 2011.

[153] I. Paprotny, C. G. Levey, P. K. Wright, and B. R. Donald, "Turning-rate selective control: A new method for independent control of stress-engineered MEMS microrobots," in *Robotics: Science and Systems*, 2012.

[154] C. Pawashe, S. Floyd, E. Diller, and M. Sitti, "Two-dimensional autonomous microparticle manipulation strategies for magnetic microrobots in fluidic environments," *IEEE Transactions on Robotics*, vol. 28, no. 2, pp. 467–477, 2012.

[155] C. Pawashe, S. Floyd, and M. Sitti, "Modeling and experimental characterization of an untethered magnetic micro-robot," *The International Journal of Robotics Research*, vol. 28, no. 8, pp. 1077–1094, 2009.

[156] C. Pawashe, S. Floyd, and M. Sitti, "Multiple magnetic microrobot control using electrostatic anchoring," *Applied Physics Letters*, vol. 94, no. 16, p. 164108, 2009.

[157] R. Pelrine, A. Wong-Foy, B. McCoy, D. Holeman, R. Mahoney, G. Myers, J. Herson, and T. Low, "Diamagnetically levitated robots: An approach to massively parallel robotic systems with unusual motion properties," in *International Conference on Robotics and Automation*, pp. 739–744, 2012.

[158] T. Petit, L. Zhang, K. E. Peyer, B. E. Kratochvil, and B. J. Nelson, "Selective trapping and manipulation of microscale objects using mobile microvortices," *Nano letters*, vol. 12, no. 1, pp. 156–60, January 2012.

[159] A. Petruska and J. Abbott, "Optimal permanent-magnet geometries for dipole field approximation," *IEEE Transactions on Magnetics*, vol. 49, no. 2, pp. 811–819, 2013.

[160] K. E. Peyer, S. Tottori, F. Qiu, L. Zhang, and B. J. Nelson, "Magnetic helical micromachines," *Chemistry (Weinheim an der Bergstrasse, Germany)*, pp. 1–12, November 2012.

[161] K. E. Peyer, L. Zhang, and B. J. Nelson, "Bio-inspired magnetic swimming microroobts for biomedical applications," *Nanoscale*, vol. 5, pp. 1259–1272, 2013.

[162] O. Piétrement and M. Troyon, "General equations describing elastic indentation depth and normal contact stiffness versus load," *Journal of Colloid and Interface Science*, vol. 226, no. 1, pp. 166–171, June 2000.

[163] R. Price, "The AAPM/RSNA physics tutorial for residents: MR imaging safety considerations," *Imaging and Therapeutic Technology*, vol. 19, no. 6, pp. 1641–1651, 1999.

[164] T. Prodromakis, K. Michelakis, T. Zoumpoulidis, R. Dekker, and C. Toumazou, "Biocompatible encapsulation of CMOS based chemical sensors," in *IEEE Sensors*, pp. 791–794, October 2009.

[165] E. M. Purcell, "Life at low Reynolds number," *American Journal of Physics*, vol. 45, no. 1, pp. 3–11, 1977.

[166] J. S. Randhawa, S. S. Gurbani, M. D. Keung, D. P. Demers, M. R. Leahy-Hoppa, and D. H. Gracias, "Three-dimensional surface current loops in terahertz responsive microarrays," *Applied Physics Letters*, vol. 96, no. 19, p. 191108, 2010.

[167] S. Rhee, "Surface energies of silicate glasses calculated from their wettability data," *Journal of Materials Science*, vol. 12, pp. 823–824, 1977.

[168] J. Richardson and J. Harker, *Chemical Engineering,* vol. 2. Butterworth and Heinemann, 5th ed., 2002.

[169] M. Roper, R. Dreyfus, J. Baudry, M. Fermigier, J. Bibette, and H. A. Stone, "On the dynamics of magnetically driven elastic filaments," *Journal of Fluid Mechanics*, vol. 554, no. 1, pp. 167–190, April 2006.

[170] S. Roundy, "On the effectiveness of vibration-based energy harvesting," *Journal of Intelligent Material Systems and Structures*, vol. 16, no. 10, pp. 809–823, 2005.

[171] A.-L. Routier-Kierzkowska, A. Weber, P. Kochova, D. Felekis, B. J. Nelson, C. Kuhlemeier, and R. S. Smith, "Cellular force microscopy for in vivo measurements of plant tissue mechanics," *Plant Physiology*, vol. 158, no. 4, pp. 1514–15122, April 2012.

[172] M. E. Rudd, "Optimum spacing of square and circular coil pairs," *Review of Scientific Instruments*, vol. 39, no. 9, p. 1372, 1968.

[173] M. S. Sakar and E. B. Steager, "Wireless manipulation of single cells using magnetic microtransporters," in *International Conference on Robotics and Automation*, pp. 2668–2673, 2011.

[174] M. S. Sakar, E. B. Steager, D. H. Kim, A. A. Julius, M. Kim, V. Kumar, and G. J. Pappas, "Modeling, control and experimental characterization of microbiorobots," *The International Journal of Robotics Research*, vol. 30, no. 6, pp. 647–658, January 2011.

[175] M. Samuelsson and D. Kirchman, "Degradation of adsorbed protein by attached bacteria in relationship to surface hydrophobicity," *American Society for Microbiology*, vol. 56, pp. 3643–3648, 1990.

[176] E. Schaler, M. Tellers, A. Gerratt, I. Penskiy, and S. Bergbreiter, "Toward fluidic microrobots using electrowetting," *2012 IEEE International Conference on Robotics and Automation*, pp. 3461–3466, May 2012.

[177] J. F. Schenck, "Safety of strong, static magnetic fields," *Journal of Magnetic Resonance Imaging*, vol. 12, no. 1, pp. 2–19, July 2000.

[178] V. Schlageter, "Tracking system with five degrees of freedom using a 2D-array of Hall sensors and a permanent magnet," *Sensors and Actuators A: Physical*, vol. 92, no. 1–3, pp. 37–42, August 2001.

[179] K. Schmidt-Nielsen, *Scaling: Why is Animal Size So Important?* Cambridge University Press, 1984.

[180] D. Schneider, "Electrons unplugged: wireless power at a distance is still far away," *IEEE Spectrum*, pp. 34–39, 2010.

[181] S. Schuerle, S. Erni, M. Flink, B. E. Kratochvil, and B. J. Nelson, "Three-Dimensional Magnetic Manipulation of Micro- and Nanostructures for Applications in Life Sciences," *IEEE Transactions on Magnetics*, vol. 49, no. 1, pp. 321–330, January 2013.

[182] S. Senturia, *Microsystem Design*. Springer, 2000.

[183] W.-M. Shen, H. Chiu, M. Rubenstein, and B. Salemi, "Rolling and climbing by the multifunctional superbot reconfigurable robotic system," in *Proceedings of the Space Technology International Forum*, pp. 839–848, Albuquerque, New Mexico, 2008.

[184] T. Shibata, T. Sasaya, and N. Kawahara, "Development of in-pipe microrobot using microwave energy transmission," *Electronics and Communications in Japan (Part II: Electronics)*, vol. 84, no. 11, pp. 1–8, November 2001.

[185] N. Shinohara, "Power Without Wires," *IEEE Microwave Magazine*, pp. 64–73, December 2011.

[186] M. Sitti, "Microscale and nanoscale robotics systems: Characteristics, state of the art, and grand challenges," *IEEE Robotics and Automation Magazine*, pp. 53–60, March 2007.

[187] M. Sitti, "Voyage of the microrobots," *Nature*, vol. 458, pp. 1121–1122, April 2009.

[188] M. Sitti and H. Hashimoto, "Controlled pushing of nanoparticles: Modeling and experiments," *IEEE/ASME Transactions on Mechatronics*, vol. 5, no. 2, pp. 199–211, June 2000.

[189] M. Sitti and H. Hashimoto, "Teleoperated touch feedback from the surfaces at the nanoscale: modeling and experiments," *IEEE/ASME Transactions on Mechatronics*, vol. 8, no. 2, pp. 287–298, June 2003.

[190] K. Sivaraman, "Functional polypyrrole coatings for wirelessly controlled magnetic microrobots," in *Point-of-Care Healthcare Technologies*, pp. 22–25, 2013.

[191] H. Skriver and N. Rosengaard, "Surface energy and work function of elemental metals," *Physical Review B*, vol. 46, no. 11, pp. 7157–7168, 1992.

[192] A. Snezhko and I. S. Aranson, "Magnetic manipulation of self-assembled colloidal asters," *Nature Materials*, vol. 10, pp. 1–6, August 2011.

[193] A. A. Solovev, Y. Mei, E. Bermúdez Ureña, G. Huang, and O. G. Schmidt, "Catalytic microtubular jet engines self-propelled by accumulated gas bubbles," *Small (Weinheim an der Bergstrasse, Germany)*, vol. 5, no. 14, pp. 1688–92, July 2009.

[194] J. S. Song, S. Lee, S. H. Jung, G. C. Cha, and M. S. Mun, "Improved biocompatibility of parylene-C films prepared by chemical vapor deposition and the subsequent plasma treatment," *Journal of Applied Polymer Science*, vol. 112, no. 6, pp. 3677–3685, 2009.

[195] Y. S. Song and M. Sitti, "Surface-tension-driven biologically inspired water strider robots: Theory and experiments," *IEEE Transactions on Robotics*, vol. 23, no. 3, pp. 578–589, 2007.

[196] P. S. Sreetharan, J. P. Whitney, M. D. Strauss, and R. J. Wood, "Monolithic fabrication of millimeter-scale machines," *Journal of Micromechanics and Microengineering*, vol. 22, no. 5, p. 055027, May 2012.

[197] E. Steager, C.-B. Kim, J. Patel, S. Bith, C. Naik, L. Reber, and M. J. Kim, "Control of microfabricated structures powered by flagellated bacteria using phototaxis," *Applied Physics Letters*, vol. 90, no. 26, p. 263901, 2007.

[198] J. Stevens, "Optimized thermal design of small delta T thermoelectric generators," in *34th Intersociety Energy Conversion Engineering Conference*, 1999.

[199] D. Stewart, "Finite-dimensional contact mechanics," *Philosophical Transactions Mathematical, Physical and Engineering Sciences*, vol. 359, no. 1789, pp. 2467–2482, 2001.

[200] S. H. Suhr and Y. S. Song, "Biologically inspired miniature water strider robot," in *Robotics: Science and Systems I*, Boston: MIT, 2005.

[201] O. Sul, M. Falvo, R. Taylor, S. Washburn, and R. Superfine, "Thermally actuated untethered impact-driven locomotive microdevices," *Applied Physics Letters*, vol. 89, p. 203512, 2006.

[202] B. Sümer and M. Sitti, "Rolling and spinning friction characterization of fine particles using lateral force microscopy based contact pushing," *Journal of Adhesion Science and Technology*, vol. 22, no. 5, pp. 481–506, June 2008.

[203] G. P. Sutton and M. Burrows, "Biomechanics of jumping in the flea," *The Journal of Experimental Biology*, vol. 214, pp. 836–847, March 2011.

[204] S. Takeuchi and I. Shimoyama, "Selective drive of electrostatic actuators using remote inductive powering," *Sensors and Actuators A: Physical*, vol. 95, no. 2–3, pp. 269–273, January 2002.

[205] G. Taylor, "Analysis of the swimming of microscopic organisms," *Proceedings of the Royal Society A: Mathematical, Physical and Engineering Sciences*, vol. 209, no. 1099, pp. 447–461, November 1951.

[206] M. T. Tolley, M. Krishnan, D. Erickson, and H. Lipson, "Dynamically programmable fluidic assembly," *Applied Physics Letters*, vol. 93, no. 25, p. 254105, 2008.

[207] S. Tottori, N. Sugita, R. Kometani, S. Ishihara, and M. Mitsuishi, "Selective control method for multiple magnetic helical microrobots," *Journal of Micro-Nano Mechatronics*, vol. 6, no. 3–4, pp. 89–95, August 2011.

[208] S. Tottori, L. Zhang, F. Qiu, K. K. Krawczyk, A. Franco-Obregón, and B. J. Nelson, "Magnetic helical micromachines: Fabrication, controlled swimming, and cargo transport," *Advanced materials*, vol. 24, no. 6, pp. 811–816, February 2012.

[209] K. Tsuchida, H. M. García-García, W. J. van der Giessen, E. P. McFadden, M. van der Ent, G. Sianos, H. Meulenbrug, A. T. L. Ong, and P. W. Serruys, "Guidewire navigation in coronary artery stenoses using a novel magnetic navigation system: First clinical experience," *Catheterization and Cardiovascular Interventions*, vol. 67, no. 3, pp. 356–63, March 2006.

[210] H. W. Tung and D. R. Frutiger, "Polymer-based Wireless Resonant Magnetic microrobots," in *International conference on Robotics and Automation*, pp. 715–720, 2012.

[211] W. R. Tyson and W. A. Miller, "Surface free energies of solid metals: Estimation from liquid surface tension measurements," *Surface Science*, vol. 62, pp. 267–276, 1977.

[212] P. A. Valberg and J. P. Butler, "Magnetic particle motions within living cells. Physical theory and techniques," *Biophysical Journal*, vol. 52, no. 4, pp. 537–550, October 1987.

[213] P. Vartholomeos, M. R. Akhavan-sharif, and P. E. Dupont, "Motion planning for multiple millimeter-scale magnetic capsules in a fluid environment," in *IEEE International Conference on Robotics and Automation*, pp. 1927–1932, 2012.

[214] J. Visser, "On Hamaker constants: A comparison between Hamaker constants and Lifshitz-van der Waals constants," *Advances in Colloid and Interface Science*, vol. 3, no. 4, pp. 331–363, 1972.

[215] F. Walther, P. Davydovskaya, S. Zürcher, M. Kaiser, H. Herberg, A. M. Gigler, and R. W. Stark, "Stability of the hydrophilic behavior of oxygen plasma activated SU-8," *Journal of Micromechanics and Microengineering*, vol. 17, no. 3, pp. 524–531, March 2007.

[216] L. Wang and F. G. Yuan, "Vibration energy harvesting by magnetostrictive material," *Smart Materials and Structures*, vol. 17, no. 4, p. 045009, August 2008.

[217] M. Wautelet, "Scaling laws in the macro-, micro-and nanoworlds," *European Journal of Physics*, vol. 22, pp. 601–611, 2001.

[218] S. Webb, ed., *The Physics of Medical Imaging*. CRC Press, 2 ed., 2010.

[219] D. B. Weibel, P. Garstecki, D. Ryan, W. R. DiLuzio, M. Mayer, J. E. Seto, and G. M. Whitesides, "Microoxen: Microorganisms to move microscale loads," *Proceedings of the National Academy of Sciences of the United States of America*, vol. 102, no. 34, pp. 11963–7, August 2005.

[220] P. N. Wells, "Current status and future technical advances of ultrasonic imaging," *Engineering in Medicine and Biology*, vol. 19, no. 5, pp. 14–20, 2000.

[221] C. Wiggins and R. Goldstein, "Flexive and propulsive dynamics of elastica at low reynolds number," *Physical Review Letters*, vol. 80, no. 17, pp. 3879–3882, April 1998.

[222] C. B. Williams, C. Shearwood, M. A. Harradine, P. Mellor, T. S. Birch, and R. B. Yates, "Development of an electromagnetic micro-generator," *IEEE Proceedings — Circuits, Devices and Systems*, vol. 148, no. 6, p. 337, 2001.

[223] J. A. Williams, "Friction and wear of rotating pivots in MEMS and other small scale devices," *Wear*, vol. 251, no. 1–12, pp. 965–972, October 2001.

[224] M. Wu, J. W. Roberts, and M. Buckley, "Three-dimensional fluorescent particle tracking at micron-scale using a single camera," *Experiments in Fluids*, vol. 38, no. 4, pp. 461–465, February 2005.

[225] Y. Xia and G. M. Whitesides, "Soft Lithography," *Angewandte Chemie*, vol. 37, no. 5, pp. 550–575, 1998.

[226] A. Yamazaki, M. Sendoh, K. Ishiyama, K. Ichi Arai, R. Kato, M. Nakano, and H. Fukunaga, "Wireless micro swimming machine with magnetic thin film," *Journal of Magnetism and Magnetic Materials*, vol. 272, pp. E1741–E1742, 2004.

[227] M. Yasui, M. Ikeuchi, and K. Ikuta, "Magnetic micro actuator with neutral buoyancy and 3D fabrication of cell size magnetized structure," in *IEEE International Conference on Robotics and Automation*, pp. 745–750, St. Paul, 2012.

[228] Z. Ye, E. Diller, and M. Sitti, "Micro-manipulation using rotational fluid flows induced by remote magnetic micro-manipulators," *Journal of Applied Physics*, vol. 112, no. 6, p. 064912, September 2012.

[229] E. M. Yeatman, "Advances in power sources for wireless sensor nodes," in *International Workshop on Body Sensor Networks*, pp. 20–21, 2004.

[230] K. B. Yesin, K. Vollmers, and B. J. Nelson, "Guidance of magnetic intraocular microrobots by active defocused tracking," in *International Conference on Intelligent Robots*, pp. 3309–3314, Ieee, 2004.

[231] K. B. Yesin, K. Vollmers, and B. J. Nelson, "Modeling and control of untethered biomicrorobots in a fluidic environment using electromagnetic fields," *International Journal of Robotics Research*, vol. 25, no. 5–6, pp. 527–536, 2006.

[232] M. Yim, W.-M. Shen, B. Salemi, D. Rus, M. Moll, H. Lipson, E. Klavins, and G. S. Chirikjian, "Modular Self-Reconfigurable Robot Systems," *IEEE Robotics and Automation Magazine*, vol. 14, no. 1, pp. 43–52, 2007.

[233] E. Yoshida, "Micro self-reconfigurable modular robot using shape memory alloy micro-sized robotic module," *Journal of Robotics and Mechatronics*, vol. 13, pp. 212–219, 2001.

[234] E. Yoshida, S. Kokaji, S. Murata, K. Tomita, and H. Kurokawa, "Micro self-reconfigurable robot using shape memory alloy," *Journal of Robotics and Mechatronics*, vol. 13, no. 2, pp. 212–219, 2001.

[235] M. Yuce and A. Demirel, "The effect of nanoparticles on the surface hydrophobicity of polystyrene," *European Physics Journal*, vol. 64, pp. 493–497, 2008.

[236] L. Zhang, J. J. Abbott, L. Dong, B. E. Kratochvil, D. Bell, and B. J. Nelson, "Artificial bacterial flagella: fabrication and magnetic control," *Applied Physics Letters*, vol. 94, p. 064107, 2009.

[237] L. Zhang, J. J. Abbott, L. Dong, K. E. Peyer, B. E. Kratochvil, H. Zhang, C. Bergeles, and B. J. Nelson, "Characterizing the swimming properties of artificial bacterial flagella," *Nano Letters*, vol. 9, no. 10, pp. 3663–7, October 2009.

[238] L. Zhang, T. Petit, K. E. Peyer, and B. J. Nelson, "Targeted cargo delivery using a rotating nickel nanowire," *Nanomedicine*, vol. 8, no. 7, pp. 1074–1080, March 2012.

[239] L. Zhang, K. E. Peyer, and B. J. Nelson, "Artificial bacterial flagella for micromanipulation," *Lab-on-a-Chip*, vol. 10, no. 17, pp. 2203–2215, September 2010.